SOCIETY FOR MATERIALS CHEMISTRY

Society for Materials Chemistry

Society for Materials Chemistry was mooted in 2007 with following aims and objectives:

(a) to help the advancement, dissemination and application of the knowledge in the field of materials chemistry,

(b) to promote active interaction among all material scientists, bodies, institutions and industries interested in achieving the advancement, dissemination and application of the knowledge of materials chemistry,

(c) to disseminate information in the field of materials chemistry by publication of bulletins, reports, newsletters, journals.

(d) to provide a common platform to young researchers and active scientists by arranging seminars, lectures, workshops, conferences on current research topics in the area of materials chemistry,

(e) to provide financial and other assistance to needy deserving researchers for participation to present their work in symposia, conference, etc.

(f) to provide an incentive by way of cash awards to researchers for best thesis, best paper published in journal/national/international conferences for the advancement of materials chemistry,

(g) to undertake and execute all other acts as mentioned in the constitution of SMC.

Executive Committee

President
Dr. S. K. Sarkar
Bhabha Atomic Research Centre
Trombay, Mumbai, 400 085
sarkarsk@barc.gov.in

Vice-Presidents
Dr. V. K. Jain
Bhabha Atomic Research Centre
Trombay, Mumbai, 400 085
jainvk@barc.gov.in

Prof. Sandeep Verma
Indian Institute of Technology
Kanpur
sverma@iitk.ac.in

Secretary
Dr. P. A. Hassan
Bhabha Atomic Research Centre
Trombay, Mumbai, 400 085
hassan@barc.gov.in

Treasurer
Dr. Sandeep Nigam
Bhabha Atomic Research Centre
Trombay, Mumbai, 400 085
snigam@barc.gov.in

Members
Dr. K. Ananthasivan
Indira Gandhi Centre for Atomic Research
Kalpakkam, 603102

Dr. (Smt.) A. Banerjee
Bhabha Atomic Research Centre
Trombay, Mumbai-400085

Dr. K. Bhattacharya
Bhabha Atomic Research Centre
Trombay, Mumbai-400085

Dr. D. Das
Bhabha Atomic Research Centre
Trombay, Mumbai-400085

Dr. G. K. Dey
Bhabha Atomic Research Centre
Trombay, Mumbai-400085

Dr. P. Sujata Devi
CSIR Central Glass & Ceramic Research
Institute, Kolkata-700032

Dr. C. P. Kaushik
Bhabha Atomic Research Centre
Trombay, Mumbai-400085

Dr. T. Mukherjee
Bhabha Atomic Research Centre
Trombay, Mumbai-400085

Dr. M. C. Rath
Bhabha Atomic Research Centre
Trombay, Mumbai-400085

Dr. (Smt.) S. S. Rayalu
CSIR National Environmental
Engineering Research Institute, Nagapur

Prof. S. D. Samant
Institute of Chemical Technology
Mumbai

Dr. A. K. Tyagi
Bhabha Atomic Research Centre
Trombay, Mumbai-400085

Dr. R. K. Vatsa
Bhabha Atomic Research Centre
Trombay, Mumbai-400085

Co-opted Members
Prof. A. Ajayaghosh
CSIR – National Institute for
Interdisciplinary Science and Technology
Thiruvananthapuram

Prof. A. K. Ganguli
Director, Institute for Nanoscience and
Technology

Prof. S. Ram
Indian Institute of Technology - Kharagpur

Dr. A. K. Tripathi
Bhabha Atomic Research Centre
Trombay, Mumbai-400085

Contact address
Society for Materials Chemistry
C/o Chemistry Division
Bhabha Atomic Research Centre, Trombay, Mumbai, 400 085, India
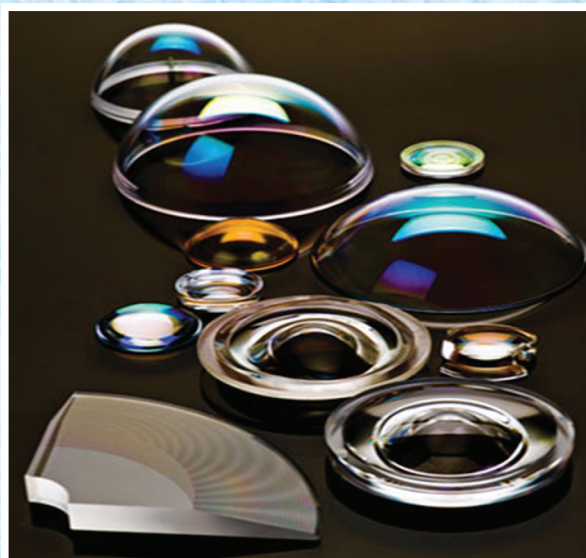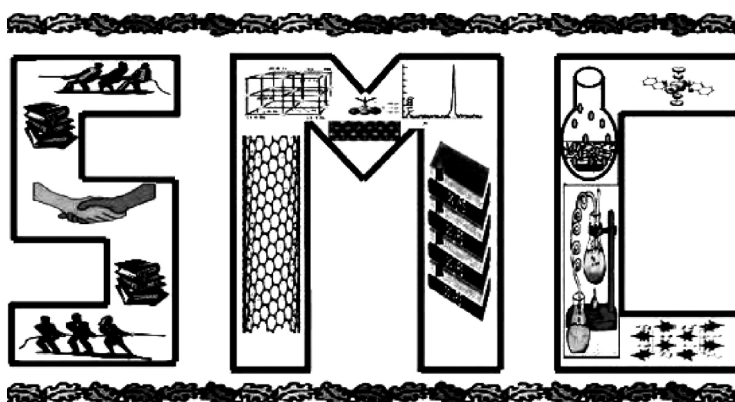Tel: +91-22-25592001, E-mail: socmatchem@gmail.com

SMC Bulletin

A Publication of the Society for Materials Chemistry

Volume 6   No. 2   August 2015

SOCIETY FOR MATERIALS CHEMISTRY

About the Cover page graphic

Front cover shows some diamond turned aspherical polymer optics along with Transmission spectra of 17 layer F-P filter with a graded spacer thickness varying from 0 to 33nm.

Please note that the authors of the paper are alone responsible for the technical contents of papers and references cited therein

Guest Editorial

Dr. S. K. Sarakar   **Dr. N. K. Sahoo**

Optics and photonics technologies are central to modern life, spanning from communication,energy sector, medical science, entertainmentdomain to computation. This year we are celebrating the International Year of Light (IYL 2015) and the light-based technologies which can promote sustainable development and provide solutions to global challenges in energy, education, agriculture, health care and security. For example, in the last decade, advances in optical fiber communications have permitted a nearly 100-fold increase in the amount of information that can be transmitted, enabling a society-transforming Internet to thrive. As noted in the introduction to Charles Kao's 2009 Nobel Prize lecture on his work in optical fiber communications, "the work has fundamentally transformed the way we live our daily lives."

These technologies enable the manufacture and inspection of all the integrated circuits in every electronic device in use. They give us displays on our smartphones and computing devices, optical fiber that carries the information in the Internet, advanced precision fabrication, and medical diagnostics tools. Optics and photonics technology offers the potential for even greater societal impact over the next few decades. Solar power generation and new efficient lighting, for example, could transform the energy landscape, and new optical capabilities will be essential to supporting the continued exponential growth of the Internet. Optics and photonics technology development and applications have substantially increased across the globe over the past several years. This is an encouraging trend for the world's economy and its people.

The Sun has been identified as one of the primary sources of alternative energy as the world is making transitions from a fossil-fuel-driven energy infrastructure in the next 20 years. Several of the exotic elements required by emerging solar technologies rely on joint production methods, which pose another potential risk to scale-up. These materials especiallygallium, tellurium, and selenium are currently produced as by-products of refinement or extraction of more common materials. The use of light-emitting diodes (LEDs) for lighting is another example of how optics is affecting energy conservation in several industrial nations. Several countries around the world have initiatives to phase out the use of incandescent lightbulbs by 2020. LEDs have been identified as the leading replacement technology for this mass market. One promising approach to obtain white light is to use galliumnitride (GaN)-based blue LEDs in conjunction with fluorescent phosphors containing rare earth elements like europium and terbium.

Synthetic biology is a new field of biological research and technology development that combines science and engineering with the goal of designing and constructing novel and useful biological systems not found in nature. Synthetic biology has provided the means of both genetically engineering specific optical properties into living organisms and manufacturing optically active materials, both of which are now routinely used in life science research.One of the major advances of the last two decades in the life sciences (the subject of a Nobel Prize in 2008) was the development of genetic engineering techniques that allow the programming of individual cells to produce protein molecules that fluoresce in response to specific stimuli. The approach is used for optical detection of the turning on and turning off of specific genes in cells in response to drugs or environmental conditions. Similarly, neurons engineered to produce fluorescent dyes based on proteins that report the active and inactive states of neurons in living animals are being used to map out the neuronal wiring of living brains and to track the flow of information through neural circuits in live

animals.New, highly efficient inorganic dyes have been developed that can be chemically linked to nucleic acids and provide an optical readout of nucleic acid sequences in high-throughput DNA sequencing instruments.

Materials are playing an increasingly important role in the technological evolution of photonic and optical applications. Whether the applications are related to imaging of cellular functions, the development of new types of sensors and solar cells, or the integration of materials for optoelectronics, the study of techniques to alter how light interacts with materials has become an important element in the advancement of various applications. Moreover, defence applications require an assured and secure manufacturing source of key materials. Engineered materials, including photonic crystals, have come of age. We have seen key optoelectronic materials play an important role in negotiations between countries. Material development has always been a slow and expensive process, but with the advent of engineered materials and the rise of awareness of the importance of certain materials, materials have taken on a strong enough strategic importance to warrant the publication of the present issue.

We sincerely thank all contributing authors for their keen interest, ready response and commitments to bring out this issue in time. We also thank our colleagues who have put their valuable efforts towards timely finalization of this issue. Past developments and recent advances in the area of optical materials arethe central focus of this special issue. We are certain that these articles will provide a deep insight in to this exciting and challenging topic and will serve as a useful resource material for young researchers.

N.K.Sahoo   **S.K.Sarkar**

Guest Editor

From the desks of the President and Secretary

Dr. Sisir K Sarkar
President

Dr. P. A. Hassan
Secretary

Dear Fellow members and Readers,

Greetings from the Executive Council of SMC.

It gives us great pleasure in organizing the third DAE-BRNS National Workshop on Materials Chemistry on Optical Materials, NWMC-2015 (OPT-MAT), during November 20-21, 2015 to celebrate the International Year of Light (IYL 2015). The importance of raising global awareness about how light-based technologies can promote sustainable development and provide solutions to global challenges in energy, education, agriculture, health care and security. The focus of the Workshop is on the synthesis and characterization of different types of optical materials and how their properties can be utilized for various applications.

On this occasion we are bringing out the thematic issue of the SMC Bulletin on "Optical Materials", in line with our tradition of publishing articles in frontier areas of materials chemistry. The role of light in our lives is both pervasive and primordial. Ultraviolet light probably had a role in the very origins of life, and light-driven photosynthesis underlies all but the most primitive of living things today. For humans, sight is the most crucial of the senses for perceiving the world around us. Indeed, the highly evolved vertebrate eye is one of the most exquisite light detectors ever created. Yet light is influencing the way we live today what we could never have imagined just a few decades ago.

Materials are playing an increasingly important role in the technological evolution of photonic and optical applications. One specific challenge that optics faces in most industries where it is being used is that optics remains an enabling technology, supporting another area such as cancer treatment or welding. The principal value of a product is not always attributed to the optical technologies associated with the product's applications. For example, developing new biological materials, such as fluorescent proteins, that have new optical characteristics is associated more with new advances in biotechnology than with optical imaging.

Finally we want to acknowledge the individual and collective contributions of the authors and editors of this issue especially Dr. N.K.Sahoo, Head, Atomic and Molecular Physics Division and Vice President, Optical Society of India for sparing his valuable time. They represent an admirable group of busy but unselfish professionals volunteering their limited time tending to the scientific "commons" on which we all depend. We are certain that these articles will provide a deep insight in to this exciting and challenging topic and will serve as a useful resource material for young researchers.

Finally, we wish to express our gratitude to all members of SMC for their continued support and cooperation in the growth of the society.

Dr. Sisir K Sarkar
President

Dr. P. A. Hassan
Secretary

CONTENTS

Characterization of Optical Thin Films by Spectrophotometry and Atomic Force Microscopy

S. Jena, R.B. Tokas, S. Thakur and N.K. Sahoo

Atomic & Molecular Physics Division, Bhabha Atomic Research Centre, Mumbai 400085, India
E-mail: shujena@barc.gov.in

Abstract:

The present article provides an overview of optical and morphological characterization of optical thin films by using spectrophotometry and atomic force microscopy (AFM) respectively. The basic principle of spectrophotometer for thin film transmission measurement is discussed briefly. The optical properties such refractive index, extinction co-efficient and band gap along with film thickness is determined from the transmission spectrum using two popular method (i) Envelope method and (ii) Inverse synthesis method. The detail theoretical formulation of the two methods has been discussed and applied to a thin film sample for example purpose. The working principle and different imaging modes of AFM is explained briefly to gain basic understanding about this technique. The surface quality of any optical thin film is qualified by probing its surface topography using AFM. The procedure for deriving important surface parameters such as root mean square (RMS) roughness and grain size or particle size from the AFM image is discussed with an example. The power spectral density (PSD) of AFM data provides a more thorough description of the morphology than only rms roughness. The detail procedure of extracting different surface characteristic parameters from the average PSD function derived from the topography has been described and implemented for normally and glancing angle deposited HfO_2 thin films as an example.

1. Introduction

Spectral characteristics and surface morphology are the two most important characteristics, which mainly defines the quality of any thin film optical coatings. The spectral characteristics (transmission, reflection and absorption) generally measured by UV-VIS-NIR spectrophotometry, while surface morphology is probed through atomic force microscopy (AFM). The spectral characteristics of optical thin films depends on the wavelength dependence of the optical constants, i.e. the refractive index $n(\lambda)$ and the extinction co-efficient $k(\lambda)$ of thin films, and their physical thickness, d. The determination of the optical constants is of great importance in the design of any optical interference filters. Few examples of optical interference filters are band pass filters, beam splitters, neutral density filters, antireflection coatings, high reflectivity mirrors etc. Successful fabrication of such filters is often directly related to the accurate value of $n(\lambda)$, $k(\lambda)$ and d. There are numerous methods for the determination of optical constants of thin films. But we will focus on two routinely used methods such as Envelope/Swanepoel method[1,2] and Inverse synthesis method[3], in which optical constants and film thickness are derived from single transmission measurement only. Surface roughness and grain structure has strong influence on many physical properties such as optical, tribological, adhesion etc. Therefore accurate evaluation of such surface characteristics is necessary. For optical coating applications, surface roughness of thin films is responsible for optical losses, because of scattering mainly for UV and deep-UV optical devices. This optical loss reduces the efficiency of the optical devices. Therefore it is necessary to have minimum roughness for fabricating high quality optical devices. The optical scattering phenomena strongly depend on both the morphology as well as the grain structure of the films. The AFM, since its inception, has been used by various researchers in different fields to image and to obtain qualitative and quantitative information about surface morphology, grain structure, elasticity, viscoelasticity, frictional force, photoconductivity, chemical composition mapping etc. In this article, we will only discuss the working principle and potential application of AFM to characterize the surface roughness and grain structure of thin film optical coatings. Further, the parameters like micro-surface roughness, lateral distributions of heights and surface microstructure of thin films are determined using power spectral density (PSD) function[4]. The detail formulation of PSD to extract these parameters by fitting with suitable combination of theoretical models is discussed. The transparent refractory oxide coating materials generally used for development of variety of optical interference filters is HfO_2, ZrO_2, SiO_2, TiO_2, Ta_2O_5, Nb_2O_5, Sc_2O_3, Gd_2O_3 etc[5]. They are used, because of their large transparent spectral range from ultraviolet to infrared region, better thermal, chemical and mechanical stability and high laser damage threshold[5]. Finally these two characterization techniques

are implemented on few thin film optical coatings to show their potential applications to characterize their optical and morphological properties.

2. Spectrophotometry:

Spectrophotometry is a technique to measure the transmission, reflection and absorption characteristics of a material as a function of wavelength of light. Spectrophotometry deals with near UV, visible and near IR light. The application of spectrophotometers is enormous in different field of science and technology. It includes semiconductors and laser technology, optics and photonics, printing and forensic examination, as well as in laboratories for the study of materials, chemicals and biological samples. There are two types of spectrophotometer (i) single beam spectrophotometer[6] and (ii) double beam spectrophotometer[7], which can be used for measuring the transmission in low absorbing materials.

Single beam spectrophotometer: The schematic diagram of a single-beam spectrophotometer is shown in Fig. 1. Light from the source lamp is collimated and then passed through a monochromator, which diffracts the light. The narrow bandwidths of this diffracted spectrum are then passed through a mechanical slit on the output side of the monochromator. Then the intensity of the light transmitted through the sample is measured by detectors and converted to absorbance or transmittance. Generally Halogen lamp is used for VIS-NIR light source while deuterium lamp is used for UV-light source. The most commonly used detectors in the UV-VIS and NIR region are the photomultiplier tubes (PMT) and PbS detector respectively. For better performance of a single beam spectrophotometer, the light source, detector, and electronics must be reasonably stable over time. The advantages to a single beam configuration are that there are often fewer moving parts. This makes the instrument simpler and less likely to have parts wear out or get out of alignment. This type of spectrophotometer is usually less expensive.

Double beam spectrophotometer: It overcomes certain limitations of the single beam spectrophotometers and is therefore preferred over them. A double beam spectrophotometer has two light beams, one of which passes through the sample while other passes through a reference cell as shown in Fig. 1. This allows more reproducible measurements as any fluctuation in the light source or instrument electronics appears in both reference and the sample and therefore can easily be removed from the sample spectrum by subtracting the reference spectrum. Modern instruments can perform this subtraction automatically. Simultaneous recording at multiple wavelengths allows recording of the entire spectrum at once. Double beam spectrophotometer is generally used to investigate the spectral characteristics of thin films or bulk materials. For transmission measurements in thin film samples, the spectrophotometer quantitatively compares the fraction of light that passes through a reference (air in our case) and the thin film, then electronically compares the intensities of the two signals and computes the percentage of transmission of the sample compared to the reference.

2.1 Optical Properties:

The optical properties can be extracted from transmission as well as from reflection spectrum depending on the materials. The methods of extracting optical constants from only transmission spectrum can be classified into two categories. The first one is an Envelope method and the second one is Inverse synthesis method. The envelope method, one of the algebraic methods, has been developed and refined by several workers after the work of Manifacier[1] *et al*. Inverse synthesis method is based on the optical structural modeling followed by the fitting of the experimental data with the theoretical one. In this following section, we briefly describe the general procedure of the two methods with their advantage and disadvantage. These two methods are applied to determine the refractive index, extinction co-efficient and thickness of ZrO_2-MgO thin film deposited using reactive electron beam evaporation for example purpose. The transmission of the film is measured in the range of 190-1200 nm with a wavelength resolution of
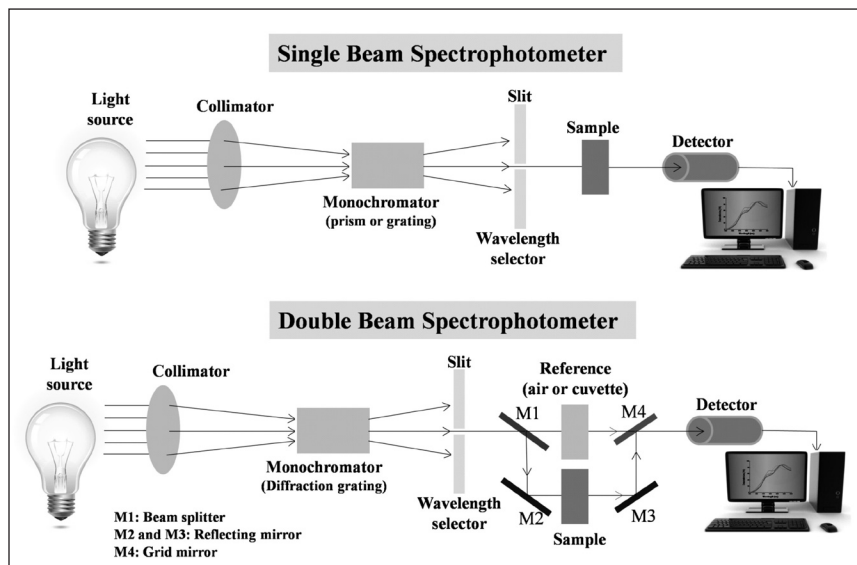

Figure 1: Schematic of Single and double beam spectrophotometer

1 nm using SHIMADZU made UV-VIS-NIR (dual beam) spectrophotometer.

2.1.1 Envelope Method:

Fig. 2 shows schematically the optical transmission measurement on a film/substrate system, in which the substrate is transparent and the film is semitransparent or transparent. The n, k and d are refractive index, extinction co-efficient and thickness of the film, while n_s, $k_s=0$ and d_s are that of the substrate. The refractive index of air is assumed to be $n_0=1$. If the film thickness is uniform, then the interference effects give rise to a spectrum as shown in Fig. 3 (ZrO$_2$-MgO thin film). These interference fringes can be used to calculate the optical constants as well as thickness of the film using Envelope method.
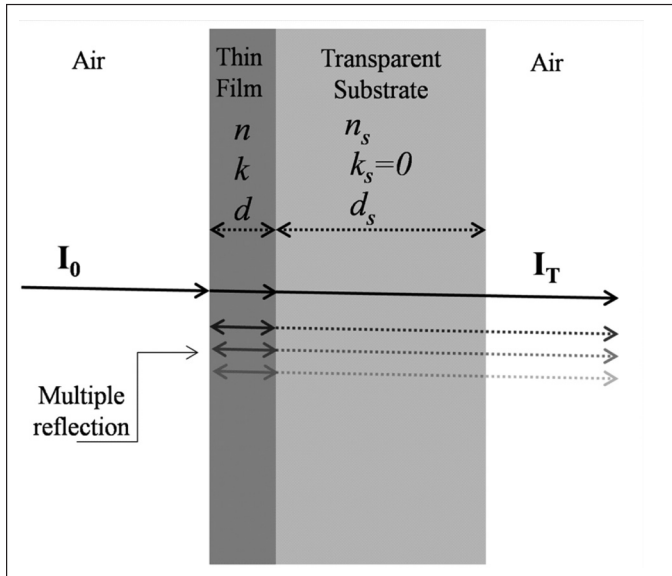

Figure 2: Schematic of light transmission through a thin film/substrate system (T=I$_T$/I$_0$).
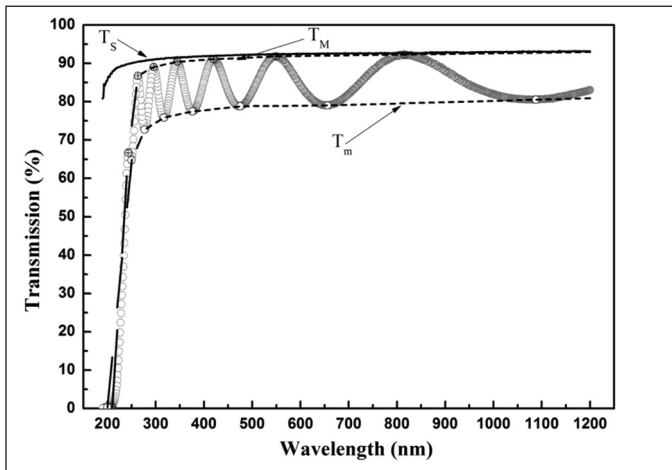

Figure 3: Transmission spectrum of ZrO$_2$-MgO thin film. Curves Ts, TM, and Tm, are as per the text.

The procedure of the Envelope method can be briefly described as follows. The details should be referred to the previous reports. The extremes of the measured transmission spectrum occur according to the condition

$$2nd = m\lambda \tag{1}$$

where m is an integer for maxima and half integer for minima and λ is the corresponding wavelength. T_M and T_m define the envelopes passing tangentially through the maxima and minima as shown in Fig. 3. The refractive index of the transparent substrate can be calculated from the transmission spectrum T_s via the relation

$$n_s = \frac{1}{T_s} + \sqrt{\frac{1}{T_s^2} - 1} \tag{2}$$

Above the strong absorption region, the expression for refractive index at wavelength of different extreme points is given by

$$n = \sqrt{N + \sqrt{N - n_s^2}} \tag{3}$$

where $\quad N = 2n_s \dfrac{T_M - T_m}{T_M T_m} + \dfrac{n_s^2 + 1}{2} \tag{4}$

Using equation (1), we can estimate the film thickness by the relation

$$d = \frac{\lambda_1 \lambda_2}{2[\lambda_1 n(\lambda_1) - \lambda_2 n(\lambda_2)]} \tag{5}$$

where λ1 and λ1 are the wavelength of two adjacent maxima (or minima). The more accurate thickness of the thin film can be obtained by following the procedure described elsewhere. The accurate thickness of the ZrO$_2$-MgO film is 413±4 nm. Finally, from the exact value of m and the final thickness of the film, the accurate refractive index n can again be calculated for each maximum and minimum using Eq. (1) as shown in Fig. 3. The refractive index as a function of wavelength n (λ) can be then obtained by fitting the estimated values as shown in Fig. 5 (a) using Cauchy dispersion equation[8].

The extinction co-efficient (k) is given by

$$k = \frac{\alpha}{4\pi} \lambda = -\frac{\lambda}{4\pi d} \ln\left[\frac{(n+1)(n+n_s)(\sqrt{T_M} - \sqrt{T_m})}{(n-1)(n-n_s)(\sqrt{T_M} + \sqrt{T_m})} \right] \tag{6}$$

The calculated extinction co-efficient at different extreme of the transmission spectrum along with its fitting using Cauchy dispersion model to get k (λ) is shown in Fig. 5 (b).

This method works well for thick film having interference fringes extremes. It fails at strong absorption edge. This method also does not suitable if there are local absorption bands in between interference fringes extremes. It also fails if the film has high absorption such that interference fringes are not visible unlike at absorption edge. The accuracy of the method decreases with decreasing film thickness. Because with decreasing thickness, the spacing between interferences extremes increases, this makes interpolation between extremes more difficult[9]. Instead of all this pitfalls, the Envelope method is widely used as routine analysis technique for determination of optical constants of transparent or semiconducting optical materials.

2.1.2 Inverse synthesis Method:

The optical constants (n & k) of the films have been obtained by fitting the measured transmission spectrum with a theoretically generated spectrum. The reliability of inverse synthesis mainly depends on the validity of optical model and the fitting statistics. The procedure of this method is as follows.

(i) Measure the transmission of thin film deposited on a weakly absorbing substrate.

(ii) The optical parameters and thickness of thin film as well as substrate should be assumed properly. The transmission of the film/substrate structure as shown in Fig. 1can then be readily calculated from the complex refractive index of the film (n+ik) and thickness (d) using the expression given elsewhere[10].

(iii) The wavelength dependency of n (λ) and k (λ) are generally expressed by different dispersion models such as (1) Cauchy-Urbach model[11] (2) single oscillator model[12] (3) Adachi model[13] (4) Forouhi and Bloomer model[14] (5) Tauc-Lorentz model[15] (6) Cody-Lorentz model[16] etc.

(iv) Using the above procedure, the fitting has been carried out by minimizing the squared difference (χ^2) between the experimentally measured and calculated values of transmission given by:

$$\chi^2 = \frac{1}{(2N-P)} \sum_{i=1}^{N} \left[\left(T_i^{Exp} - T_i^{Cal} \right)^2 \right] \qquad (7)$$

Where T_i^{Exp} and T_i^{Cal} are the experimental and theoretical transmittances respectively. N is the number of data points, P is the number of model parameters and the minimization has been done using the Levenberg-Marquardt algorithm. After the fine adjustment of model parameters, a good fitting can be achieved.
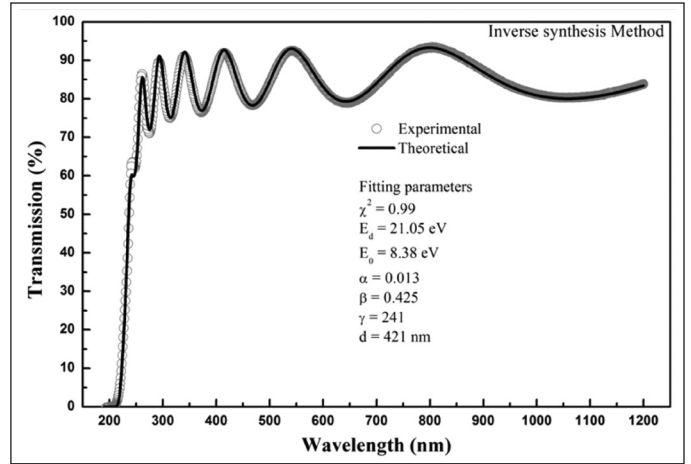

Figure 4: Experimental and fitted transmission spectrum of the ZrO$_2$–MgO thin film.

For an example point of view, the experimental transmission spectrum along with its fitting for ZrO$_2$-MgO thin film using single oscillator and Urbach dispersion model for refractive index and extinction co-efficient respectively is shown in Fig. 4. Single oscillator model assumes that the material is composed of individual dipole oscillators that are set to forced vibration by the incident light. Wemple and DiDomenico Jr. proposed that the lowest energy oscillator had the largest contribution to n and a single term Sellmeier relation describes the dispersion of refractive index equation given by:

$$n(\lambda) = \sqrt{1 - \frac{E_0 E_d}{E_0^2 - (hc/\lambda)^2}} \qquad (8)$$

Where h is Planck's constant, c is the velocity of the light, E_0 is the oscillator energy, E_d is the dispersion energy and can be closely associated with the structural order parameter. The imaginary part of the refractive index, i.e., the extinction coefficient (k) of the composite is assumed to follow the Urbach model as given below.

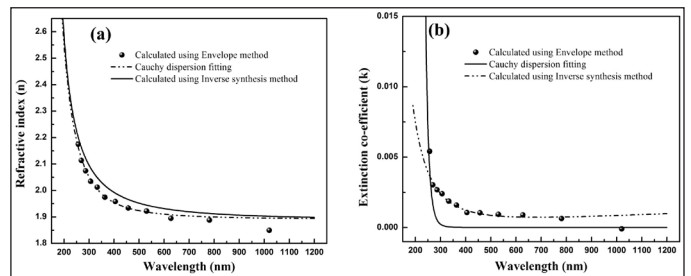$$k(\lambda) = \alpha \exp(1240\beta(1/\lambda - 1/\gamma)) \qquad (9)$$

Figure 5: (a) Refractive index and (b) extinction co-efficient spectra of the ZrO$_2$–MgO thin film.

Fig. 5(a) shows the refractive index of ZrO_2-MgO thin film determined using both Envelope method and Inverse synthesis method. Fig. 5(b) shows the extinction co-efficient spectra determined by both the methods. The refractive index and thickness value obtained by these two methods are almost close, while the extinction co-efficient differs a lot. The Inverse synthesis method is very powerful and can yield very accurate values of optical constants (n & k) for thin films or even multilayer thin films with some know parameter like film thickness or material parameters as guess value. The only limitation of this method is that one has to make assumptions about the type of dispersion relation before start the fitting procedure[9]. The advantage of inverse synthesis method is that it can be applicable to any type of thin film, while Envelope method is suitable for transparent or semitransparent thick films.

2.1.3 Optical band gap:

The optical band gap (E_g) of the films is determined from the obtained values of absorption co-efficient (α). Around strong absorption region, the optical absorption is computed from the measured transmission (T) and reflection (R) spectra using the following formula[17].

$$\alpha = \frac{1}{d} \ln \left(\frac{1-R}{T/T_{sub}} \right) \tag{10}$$

Where d is the film thickness and T_{sub} is the transmission of the bare substrate. The absorption co-efficient of thin films (behave like amorphous semiconductor) in the high absorption region ($\alpha \geq 10^4 \, cm^{-1}$) is given according to Tauc's relation[18].
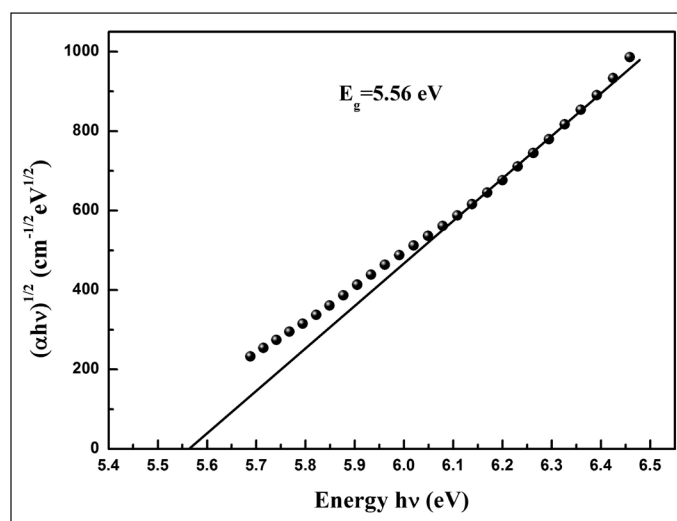
$$a h\nu = K \, (h\nu - E_g)^m \tag{11}$$

Figure 6: Representative Tauc plot for optical band gap determination of HfO_2 thin film

where K is constant depends on the transition probability, E_g is the optical band gap and m determines the type of transition (m=1/2 for direct allowed transition and m=2 for indirect allowed transition).

The best fit of the experimental result is found using Eq. (11) with m=2 i.e. optical band gap is determined by plotting $(\alpha h\nu)^{1/2}$ as a function of the photon energy hν and extrapolating the linear curve progression to zero. Fig. 6 shows the Tauc plot for HfO_2 thin film prepared by electron beam evaporation to determine its optical band gap (E_g=5.56 eV) for example purpose.

3. Atomic force microscopy (AFM):

AFM[19] is most widely used technique to investigate surface morphology of any kind of materials. It uses near-field forces between atoms of the probe tip apex ad the surface to generate signals of surface topography. This near field interactions (van der Waals force for topography) eliminates the resolution limit associated with optical microscopy, because its resolution is limited by far-field interactions between light and specimens. AFM is a high resolution imaging technique, which is less-destructive than either transmission electron microscope or scanning electron microscope. AFM is capable of measuring the vertical dimension (Z-direction) of the sample i.e. the height or depth of the surface features, while optical and electron microscope does not have this scope.

Working Principle[20]: The operation of AFM for is governed by three basic components (i) Cantilever tip (ii) piezoelectric scanner and (iii) feedback loop control system. A schematic diagram of a typical AFM system is shown in Fig. 7. A sharp tip is mounted at the end of a cantilever. The cantilever beam is attached at one end to a piezoelectric scanner. The force detection is based on a beam deflection method. A diode laser is bounced off from the back side of the cantilever (coated with metallic thin film for better reflection) onto a position-sensitive quadrant photodiode detector. This detector measures the bending of cantilever during the tip scanning over the sample surface. As the tip is scanned across the sample in the x-y direction, the force of the interaction between the sample and the tip is measured by the cantilever. A feedback loop control system is used to maintain a desired force between the tip and the sample. When the measured force is larger or smaller than this set point, the piezoelectric scanner in the z-direction moves the probe away from or towards the surface, bringing the force back to the set point. The displacement of piezo scanner directly corresponds to the height of the sample. A topographic image of the surface can be generated by scanning the tip over the sample surface and recording the displacement of the piezo-scanner as a function of position.
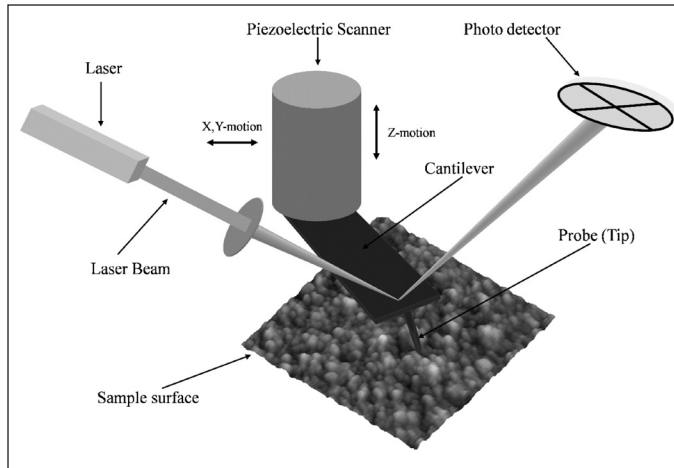
Figure 7: Schematic diagram of atomic force microscopy with beam deflection method.

Figure 8: Schematic of force-distance curve for interaction between tip and sample surface.

The cantilever is typically silicon or silicon nitride with a tip radius of curvature on the order of nanometers.

For surface topography, the dominant interactions at short tip-sample distances in the AFM are van der Waals interactions. The typical force-distance curve[21] for van der Walls interactions is shown in Fig. 8. Depending on the distance between tip-sample, there are 3 types of imaging modes[22] in AFM. They are (i) Contact mode (ii) Intermittent contact mode and (iii) Non-contact mode.

Contact mode: The tip physically touches the surface and the force (10^{-6} N < F < 10^{-9}) is repulsive as shown in Fig. 8. The force between the tip and sample remains constant by maintaining a constant cantilever deflection using the feedback loops and an image of the surface is obtained. It is a fast scanning mode and good for rough samples. It is not much suitable for soft samples as the tip may damage the sample.

Intermittent contact mode (*Tapping*): In this mode, the tip lightly "taps" on the sample surface at its resonant frequency during scanning. The tip contacts the surface at bottom of its oscillation. The force between the tip and sample remains constant by maintaining constant oscillation amplitude and an image of the surface is obtained. It gives high resolution imaging for soft samples. It is not suitable for imaging in liquids and the scan speed is slower.

Non-contact mode: The tip oscillates above the sample at a distance of 10-100 nm during scanning. The surface topography can be measured by monitoring changes in the amplitude of oscillation due to attractive van der Waals forces (10^{-9} N < F < 10^{-12}) as shown in Fig. 8 using a feedback loop. This mode extends the tip life time due to its very low force. It generally gives low resolution imaging.
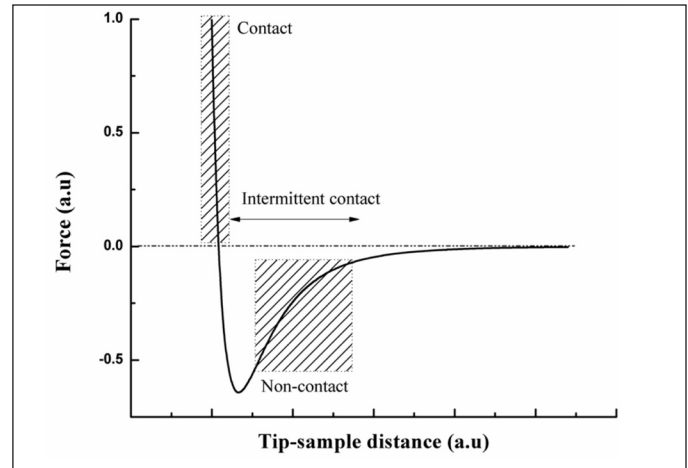
3.1 Surface morphology:

The surface morphology of optical thin films is measured using AFM. AFM images have a lateral (x, y) resolution and a vertical (z) resolution. The radius of curvature of the end of the tip will determine the highest lateral resolution obtainable with a specific tip. The vertical resolution is necessary for determining surface roughness. Root mean square (rms) surface roughness describes the finish or smoothness of optical surfaces. It represents the standard deviation of surface profile heights[23]. The lateral resolution is necessary for determination of grain or particle size[24]. However, another factor that needs to be considered during image analysis is the number of data points, or pixels, present in an image in the x and y scan-direction. For example, in acquiring a 5 µm × 5 µm area images with 512 pixels, the pixel size is ≈ 10 nm (5 µm/512 pixels). In this case, it is not possible to resolve features smaller than 10 nm at a 5 µm scan size. Thus, it is important to consider the grain size when choosing the scan size. After AFM imaging, the image can be processed for determination of surface roughness as well as grain size. The surface roughness is derived from the vertical height, while the grain size is derived from the lateral size of the grains or particles in the image. A cross-sectional line can be drawn across any part of the image to see lateral size of grains, and the vertical profile along that line is also displayed. By making several cross-sectional line profiles through different grains, it is possible to calculate the grain or particle size. This procedure is applied to determine the surface roughness and grain size of HfO_2 thin film deposited using reactive electron beam evaporation. NT-MDT, P-47H AFM system has been used for measuring the topography of the HfO_2 thin film morphological measurements of obliquely deposited HfO_2 thin films. A super sharp diamond like carbon (DLC) coated Si probe
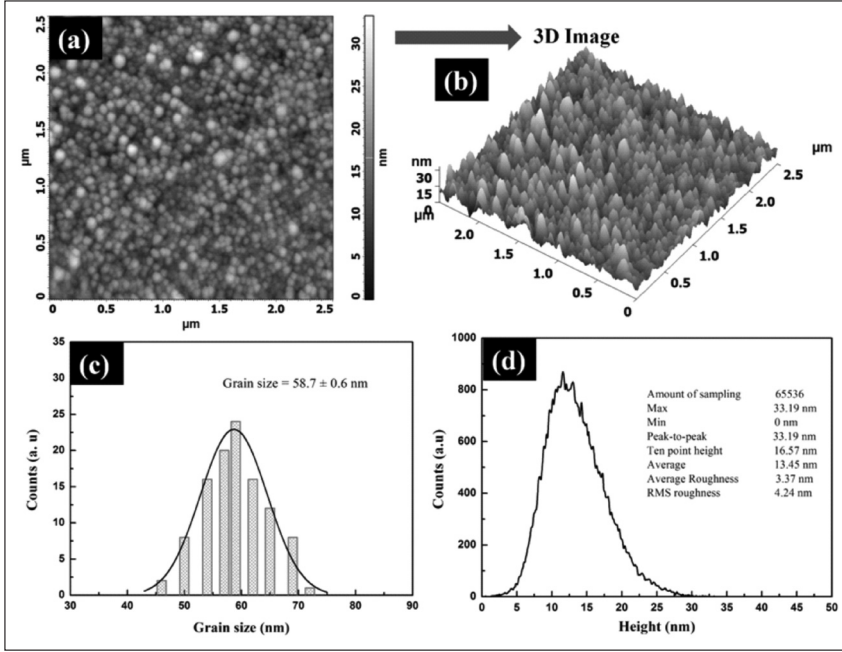
Figure 9: Representative (a) 2D, (b) 3D AFM morphology for determination of (c) grain size and (d) surface roughness of HfO$_2$ thin film.

having tip curvature 1-3 nm, resonance frequency 198 kHz and force constant 8.8 N/m has been used. DLC coated AFM probe being very hard and anti-abrasive, was chosen to get the consistency in measurements.

Measurements with different scan sizes such as 2.5x2.5 μm^2, 5x5μm^2 and 10x10 μm^2 with spatial resolution of 512x512 points have been taken for the film. The scan size 2.5x2.5 μm^2 with 512x512 points can give better spatial resolution of ≈ 5 nm, which would be useful for accurate determination of grain size or particle size. 9(a) & (b) show the 2D and 3D AFM topography of electron beam evaporated HfO$_2$ thin film. The grains are spherical in size with uniform size distribution. The estimated average grain size is found to be 58.7 ± 0.6 nm as shown in Fig. 9(c). The RMS surface roughness determined from the height counts is 4.24 nm as shown in Fig. 9(d).

3.2 Power Spectral Density:

The most important surface morphology parameter is the rms roughness. However this parameter does not account for the spatial distribution of peaks or valleys present in the surface. A more complete description is provided by power spectral density (PSD) of the surface topography. It describes both the aspects of surface topography such as the spread of heights from a mean plane and the lateral distance over which the height variation or mutual correlation occurs. For thin film optical coatings the PSD function is especially important and represents a very popular way to describe the surface quality. There are large

numbers of publications which describe the PSD based surface statistics thoroughly. We have adopted the formulation described in references[4,25] for the computation of PSDF,

$$S_2(f_x f_y) = \frac{1}{L^2}\left[\sum_{m=1}^{N}\sum_{n=1}^{N} Z_m \right.$$
$$\left. e^{-2\pi i\Delta L(f_x m + f_y n)}(\Delta L)^2\Big|\right]^2 \tag{12}$$

Here S$_2$ is the 2-dimensional PSDF, L^2 is the scan surface area, N is the number of data points in both X and Y direction of scanned area, Z$_{mn}$ is the surface profile height at position (m, n), f$_x$, and f$_y$ are the spatial frequencies in X and Y directions respectively and ΔL (L/N) is the sampling interval. Computation of PSDF is further followed by transition to polar coordinates in frequency space and angular averaging (φ)

$$S_2(f) = \frac{1}{\pi}\int_0^{2\pi} S_2(f,\varphi)d\varphi \tag{13}$$

As the PSDF depends only on one parameter, it will be plotted in all our figures as a 'slice' of the 2-D PSD function with unit '(length)^4'. Several mathematical models alone and in combinations has been proposed and used by researchers to interpret experimental PSD. The most used extended model for PSD of thin films is the sum of Henkel transforms of the Gaussian and exponential autocorrelation functions. But such model fails when wide spatial frequency range is considered. To describe roughness over large spectral frequencies, PSD model should comprises contribution from substrate, pure thin film and aggregates or superstructures. PSD of substrates generally follows inverse power law[4,25] with spatial frequency (assuming fractal like surfaces). PSD function of pure thin film is conventionally characterized by abc or k-correlation model[4,25], while PSD of aggregates or superstructures is characterized by Gaussian function with its maximum shifting to a nonzero spatial frequency[4,25]. The combination of these PSD models is given by:

$$PSD_{total} = \frac{K}{f^{\gamma+1}} + \frac{a}{(1+b^2 f^2)^{(c+1)/2}} + \sum_m \pi \sigma_{ag,m}\tau_{ag,m}$$

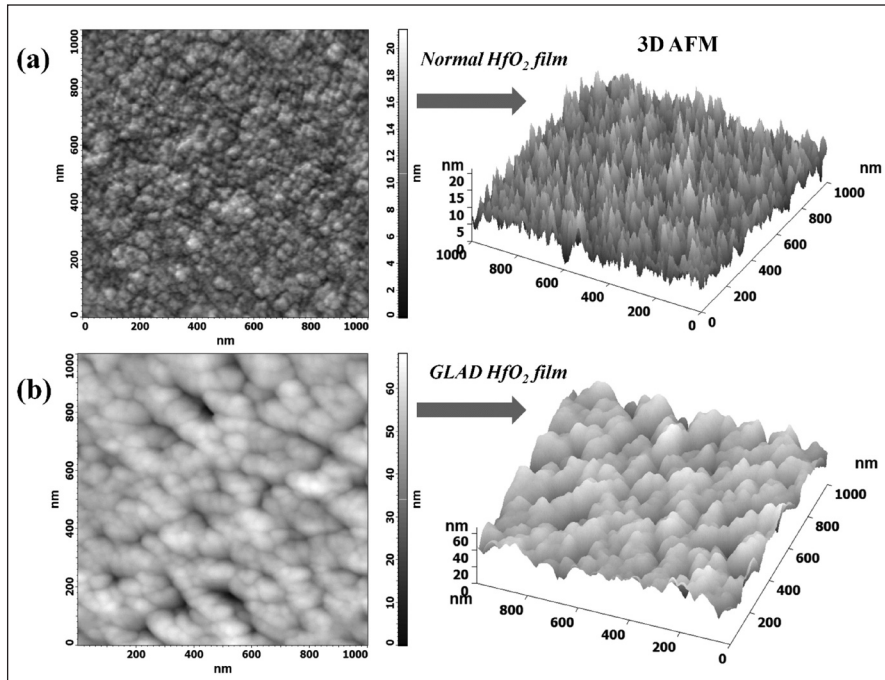$$\exp[-\pi^2\tau_{ag,m}^2(f-f_{ag,m})^2] \tag{14}$$

Figure 10: 2D and 3D AFM morphology of (a) normally deposited and (b) glancing angle deposited (GLAD) HfO₂ thin film.

resolution of 512x512 points have been taken for the film. Power spectral density function (PSDF) has been computed for each scan size and extended PSDF has been obtained by combining PSDF of different scans together by a suitable methodology as described elsewhere[25]. A representative 2D and 3D AFM image having scan size 1x1 μm^2 for both normal and glancing angle deposited HfO₂ film is shown in Fig. 10.

The experimental PSD functions are fitted with combined PSD model as described by Eq. (14) for the thin films as shown in Fig. 11. It shows that PSD function of GLAD thin film depicts higher roughness for full range of spectral frequencies as compared to normal deposited film. The intrinsic roughness which is the only contribution from pure thin film i.e. σ_{abc} (0.79 nm) is higher for GLAD film as compared to that (0.17 nm) of normal deposited film. This can be explained in the light of atomic shadowing and re-emission & diffusion of ad-atoms. For glancing angle depositions, atomic shadowing effect is very high and it leads to very high roughening effect to the surface of film. Consequently, film surface roughening due to atomic shadowing dominates the smoothing effects due to re-emission of ad-atoms diffusion processes and results in the higher surface roughness as compared to the normal deposited film. It is known that correlation length (τ_{abc}) represents the size of the grains on the surface The value τ_{abc} estimated from the PSD fitting is 26.7 nm and 74.6 nm for normal and GLAD HfO₂ thin film respectively, which can be clearly verified by the AFM image in Fig. 10. The highest grain size of the GLAD film is the consequence of dominant atomic shadowing at glancing angles. In fact, diameter of slanted columns is very high at glancing angle which ultimately leads to bigger grain size as reported in our earlier work[26]. This shows the capability of PSD to extract different surface parameters of thin films having different microstructures, which is helpful to quantify the quality of optical surface.

The 1st term is power law, 2nd term is abc-model and 3rd tem is shifted Gaussian model. Here K is spectral strength of fractal and γ is fractal spectral indices. The parameters *a*, *b* and *c* are related to intrinsic rms roughness (σ_{abc}) and correlation length (τ_{abc}). The σ_{ag} corresponds to the height and τ_{ag} corresponds to the size of the aggregates or super structures. For an example purpose, normal and glancing angle deposited HfO₂ thin films have been studied using PSD function.

Three different measurements having scan sizes i.e. 1x1 μm^2, 2.5x2.5 μm^2, 5x5μm^2 and 10x10 μm^2 with spatial

Figure 11: Experimental and fitted extended PSDF of normal and GLAD deposited HfO2 thin films.

4. Conclusion:

Characterization of optical properties using spectrophotometry and surface morphology using AFM are discussed in this article. The most commonly used methods such as Envelope method and Inverse synthesis method for determination of optical properties and film thickness are described with an example. The fundamental

principle and different imaging modes of AFM are briefly presented. The surface morphological properties such as RMS roughness and grain size are probed by analysing AFM image. The power spectral density of AFM image are discussed and analysed for micro roughness parameters of thin films.

References:

1. J. C. Manifacier, J. Gasiot, J. P. Fillard, *J. Phy. E*, **1976**, *9*, 1002.
2. R. Swanepoel, *J. Phy. E*, **1983**, *16*, 1214.
3. J. A. Dobrowolski, F. C. Ho, A. Waldorf, *Appl. Opt.*, **1983**, *22*, 3191.
4. J. Ferré-Borrull, A. Duparré, E. Quesnel, *Appl. Opt.*, **2001**, *40*, 2190.
5. M. Friz, F. Waibel, in *Optical Interference Coatings*, edited by N. Kaiser, H. Pulker, Springer: Berlin Heidelberg, 2003, Vol. 88, pp. 105.
6. K. C. Kao, T. W. Davies, *J. Phy. E*, **1968**, *1*, 1063.
7. M. W. Jones, K. C. Kao, *J. Phy. E*, **1969**, *2*, 331.
8. D. Y. Smith, I. Mitio, K. William, *J. Phys.: Condens. Matter*, **2001**, *13*, 3883.
9. P. Dirk, S. Philippe Frederic, *J. Phys. D: Appl. Phys.*, **2003**, *36*, 1850.
10. S. Jena, R. B. Tokas, N. Kamble, S. Thakur, D. Bhattacharyya, N. K. Sahoo, *Thin Solid Films*, **2013**, *537*, 163.
11. D. V. Likhachev, *Thin Solid Films*, **2014**, *562*, 90.
12. S. H. Wemple, M. DiDomenico, *Phy. Rev. B*, **1971**, *3*, 1338.
13. S. Adachi, *Phy. Rev. B*, **1987**, *35*, 7454.
14. A. R. Forouhi, I. Bloomer, *Phy. Rev. B*, **1986**, *34*, 7018.
15. G. E. Jellison, F. A. Modine, *Appl. Phys. Lett.*, **1996**, *69*, 371.
16. J. Price, P. Y. Hung, T. Rhoad, B. Foran, A. C. Diebold, *Appl. Phys. Lett.*, **2004**, *85*, 1701.
17. S. Jena, R. B. Tokas, N. M. Kamble, S. Thakur, N. K. Sahoo, *Appl. Opt.*, **2014**, *53*, 850.
18. R. Naik, S. Jena, R. Ganesan, N. K. Sahoo, *Phys. Status Solidi B*, **2014**, *251*, 661.
19. G. Binnig, C. F. Quate, C. Gerber, *Phys. Rev. Lett.*, **1986**, *56*, 930.
20. E. Meyer, *Prog. Surf. Sci.*, **1992**, *41*, 3.
21. B. Cappella, G. Dietler, *Surf. Sci. Rep.*, **1999**, *34*, 1.
22. S. N. Magonov, M.-H. Whangbo, *Surface analysis with STM and AFM: experimental and theoretical aspects of image analysis*, VCH Publishers: New York, 2008.
23. N. K. Sahoo, S. Thakur, M. Senthilkumar, N. C. Das, *Appl. Surf. Sci.*, **2003**, *206*, 271.
24. J. Grobelny, F. DelRio, N. Pradeep, D.-I. Kim, V. Hackley, R. Cook, in *Characterization of Nanoparticles Intended for Drug Delivery*, edited by Scott E. McNeil, Humana Press, 2011, Vol. 697, pp. 71.
25. M. Senthilkumar, N. K. Sahoo, S. Thakur, R. B. Tokas, *Appl. Surf. Sci.*, **2005**, *252*, 1608.
26. R. B. Tokas, S. Jena, P. Sarkar, S. R. Polaki, S. Thakur, S. Basu, N. K. Sahoo, *Mater. Res. Express*, **2015**, *2*, 035010.

Shri. Shuvendu Jena joined Atomic & Molecular Physics division (A&MPD), BARC in the year 2010 after graduating from 53rd batch of BARC training school. He is working on Optical coatings and devices for laser and spectroscopic applications for various DAE projects.

Shri. R. B. Tokas joined Atomic & Molecular Physics Division (A&MPD), BARC in the year 2003 after graduating from 46th batch of BARC training school. He has been involved in activities like design and development of interference multi-layer devices for various laser applications, investigation of various properties of thin films of HfO2, SiO2, TiO2, Al2O3MgO, ZrO2 etc., used for the fabrication of multilayer devices. Glancing angle deposition of oxide thin films, Super-hydrophilic anti-reflection broadband coatings for solar applications

Dr. Sudhakar Thakur is working in Atomic & Molecular Physics Division (A&MPD), BARC. He has been involved in activities like, development of beam splitters for selective dye laser pumping, anti reflection coatings for CVL and other dye laser experiments, narrow band Fabry Perrot type transmitting filters etc.

Dr. N.K Sahoo is an Outstanding Scientists and Head, Atomic & Molecular Physics Division of Bhabha Atomic Research Centre. Dr. Sahoo, after graduating from Ravenshaw College completed his post-graduation from Utkal University with the specialization in Solid-state Physics. Subsequently he joined the 25th batch physics discipline OCES course of Training School of BARC. Subsequently, he joined "Multi-Disciplinary Research Section" of BARC and started his career in the field of thin film physics and technology primarily required then for high power pulse laser spectroscopy activities. He completed his PhD in Physics titled "Thin Film Optical Coatings for High Power Laser Applications", from University of Mumbai. Subsequently he was selected by National Academy of Sciences (NAS, USA) as a National Research Council (NRC) research associate to carry out post-doctoral research at NASA/Marshall Space Flight Center, Huntsville, USA in the field of "new generation multilayer thin film laser & space coatings and devices

Optical Fiber Bragg Grating Sensors for Chemical and Biochemical Sensing

Rupali Suresh and K. Divakar Rao

Photonics and Nanotechnology Section, Atomic and Molecular Physics Division,
Bhabha Atomic Research Centre Facility, Visakhapatnam-530 012
Email: rupalis@barc.gov.in; divakar@barc.gov.in;

Abstract

Fiber Bragg grating (FBG) sensors have been extensively utilized to measure physical parameters such as pressure, strain and sensor. The sensor technology offers the advantages of immunity to electromagnetic interference, small size, low volume, multiplexing capability and wavelength encoded measurement. In the last few years, FBG sensors have made entry into the chemical sensing area and also under harsh environments. This paper presents a review of the role of FBG as optical device for chemical and biochemical sensing.

Key Words: FBG sensor, hydrogen, relative humidity, refractive index, C-reactive protein, sugar

1. Introduction

Optical fibers have been extensively used in communication industry in last few decades. Concurrently, about 30 years back, the optical fiber based sensors were introduced as alternative to contemporary sensing techniques[1]. Initially, optical fiber sensors utilized the variation of intensity or phase due to applied stimuli, however, as the intensity and phase are prone to source fluctuations, vibration, bending and coupling losses, fiber Bragg grating (FBG) sensors have been introduced[2]. The FBG technique employs variation of wavelength with applied stimulus. As the wavelength is absolute parameter, the sensors are immune to any source fluctuations, vibration, bending or coupling losses in the network.

FBG have been extensively utilized for measurement of physical parameters such as pressure, shear force and temperature etc[3-6]. However, the FBG sensors have demonstrated promising potential in the chemical and bio sensing applications. This paper presents the theory and optical characteristics of the FBGs and their growth in the sensing applications.

2. Theory and fabrication of FBG sensors

2.1 Theory of FBG

FBG is a wavelength selective filter, inscribed in the core of a single mode optical fiber. The FBG comprises of the periodic variation of refractive index in the core. When light from a broadband source is launched in the optical fiber, partial reflection occurs at each interface. At a particular wavelength, which is known as the Bragg wavelength, the partially reflected waves interfere constructively, giving rise to a reflection peak. The Bragg wavelength depends on the effective refractive index and the periodicity of the refractive index variation. Their relationship is given by[2],

$$\lambda_b = 2n_{eff}\Lambda \tag{1}$$

where λ_b is Bragg wavelength that is reflected back, n_{eff} is the effective refractive index of the fiber core and Λ is the period of the grating. Schematic of the working principle of FBG is shown in Fig. 1[7].
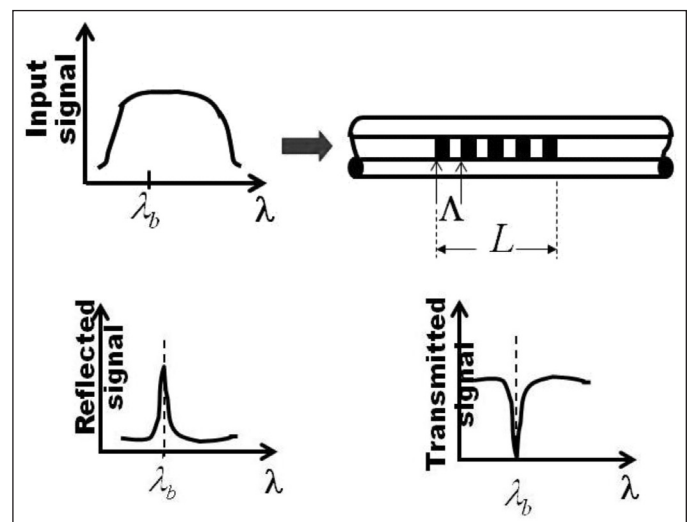
Fig. 1 *Working principle of FBG: transmission and reflection spectra*

2.2 FBG Fabrication

The periodic variation of refractive index in the core of the single mode optical fiber can be achieved by imprinting an interference pattern of UV source on to the photosensitive fiber core[8]. The interference pattern can be obtained either by a holographic set-up, where a UV- laser beam is split in to two beams and the two beams are made to interfere on the fiber core[9]. Alternately a phase mask

can also be used in the path of UV beam incident on the fiber core. The phase mask technique is widely used, as it is suitable for bulk production of the FBGs. A phase mask is a transmission grating, with nulled zeroth order. The diffraction occurs mainly in ±1 order. The beams in the ±1 order interfere and give rise to interference pattern, which can be photo imprinted in the photosensitive fiber core. Fig 2 shows the schematic of the FBG fabrication process using phase mask technique[7].

Fig. 2 *Phase mask photo- imprinting of fiber Bragg grating[7]*

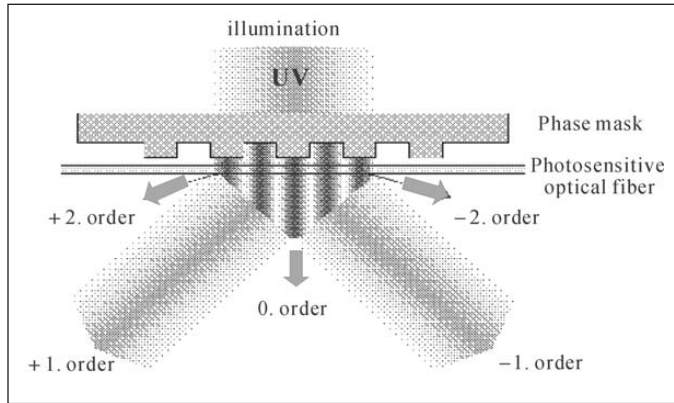The photosensitivity can be rendered to the fiber core either by doping it with suitable dopant such as germanium or boron or loading it with molecular hydrogen at high pressure[11, 12].

According to the formation mechanism, gratings can be classified as type I, type II, type II A (now known as type In), regenerated and fs-IR laser induced gratings[13]. Type I gratings are formed by a single UV photon absorption around 244 nm that excites oxygen deficiency defect centers in germanosilicate fibers. This results in small index change. When densification of glass matrix occurs with defects formation, larger index changes are obtained. Type II gratings involve multiphoton ionization process. Type IIA gratings are formed due to stress relief in the fiber. Regenerated gratings are observed in hydrogen loaded fibers, which involves formation of Si-OH or Ge-OH defects. However, exact mechanism of the process is still not fully understood. Femtosecond- IR laser induced gratings involve non-linear mutliphoton absorption or ionization process.

Based on the profile of the refractive index modulation in the core, gratings are named as uniform, chirped, sampled chirped etc[14]. In general, uniform FBG, where the grating periodicity remains uniform throughout the FBG length is used for sensing.

3. FBG as sensor

As shown in eq. (1), Bragg wavelength depends on the grating periodicity and effective refractive index. If any external stimulus is applied, which changes either grating periodicity or the effective refractive index, the reflected Bragg wavelength will shift. This shift in the Bragg wavelength is a direct measure of the applied stimulus. Thus, by measuring the wavelength shift, the applied stimulus can be measured directly. The wavelength shift with axial strain and temperature is given by[7],

$$\frac{\Delta\lambda}{\lambda_b} = \varepsilon[1 - 0.5n_{eff}\{P_{12} - \nu(P_{11} + P_{12})\}] + \xi\Delta T \quad (2)$$

where ε is the axial strain in the optical fiber core, ΔT the change in temperature, P_{ij} show the strain-optic constant, ν is Poisson's ratio and ξ is the thermo-optic coefficient of the fiber. Thus, the wavelength shift is a simultaneous measure of axial strain and temperature. However, the two parameters cannot be distinguished from wavelength shift of a single FBG. This multi parameter dependence causes cross-coupling also. Hence, temperature compensation is required. A simple approach is to locate two sensors, having different strain ($K_{\varepsilon1}$, $K_{\varepsilon2}$) and temperature sensitivities (K_{T1}, K_{T2}). One sensor is exposed to both the strain and temperature fields and the other one is exposed to the temperature variation only. Then a matrix equation can be obtained as[2],

$$\begin{pmatrix} \Delta\lambda1 \\ \Delta\lambda2 \end{pmatrix} = \begin{pmatrix} K\epsilon1 & KT1 \\ K\epsilon2 & KT2 \end{pmatrix} \begin{pmatrix} \epsilon \\ T \end{pmatrix} \quad (3)$$

Solving this, strain and temperature can be obtained simultaneously but independently.

At constant temperature (or after thermal compensation), the wavelength shift with applied pressure (P) can be obtained as[15],

$$\Delta\lambda_P = \lambda_B \left[-\frac{(1-2\nu)}{E} + \frac{n^2}{2E}(1-2\nu)(2\rho_{12} + \rho_{11}) \right]\Delta P \quad (4)$$

where E is the Young's modulus of the material of the fiber. Since, the wavelength is an absolute parameter, which does not depend on the intensity; any fluctuation in the source intensity or any coupling losses in the sensor network will not cause any error in the recorded wavelength. Also, as each FBG works in a narrow wavelength range, several FBGs can be fabricated in a single fiber. This multiplexing capability is of utmost importance as it results in very compact sensor network.

3.1 FBG for measuring physical parameters

For direct sensing, the normal force was directly applied on bare FBG. The measured wavelength shift was converted into axial strain based on the calibration result that 1 με strain corresponds to 1.2 pm wavelength shift. The deduced axial strain and the standard deviation are plotted against the applied force as shown in Fig. 3[7].
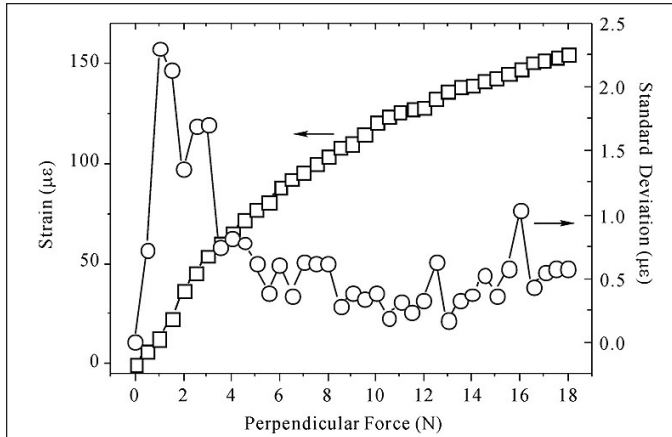

Fig. 3 *Axial strain versus perpendicular force applied on a bare FBG[7]*

The graph shows a non-linear response of axial strain with respect to the applied normal/ perpendicular force. The non-linearity between the axial strain and the perpendicular force may be due to changes in polarization as a result of stress-induced birefringence. To overcome this problem, grating fiber embedded into carbon/ epoxy composite material (to form a reinforced laminate) is employed for sensing. This technique is known as indirect sensing. A force applied on the laminate is transferred from the composite matrix to a longitudinal strain onto the fiber. Fig. 4 shows the response of embedded FBG sensor under applied normal force[7].
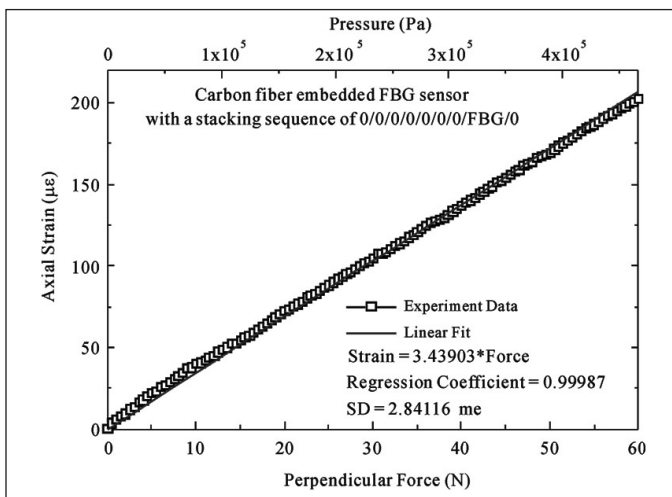

Fig. 4 *Axial strain performance when the FBG is embedded within layers of composite material[7]*

For shear force measurement, the FBG is embedded at a small angle between the upper and lower layers of carbon composite material (CCM) with a deformable layer of silicon rubber between them, as shown in Fig. 5[4]. With this embedding technique, a relative motion between the upper and lower layers occurs when shear force is applied to the upper layer of CCM. The upper layer will move in the direction of the applied shear force with respect to the lower layer.
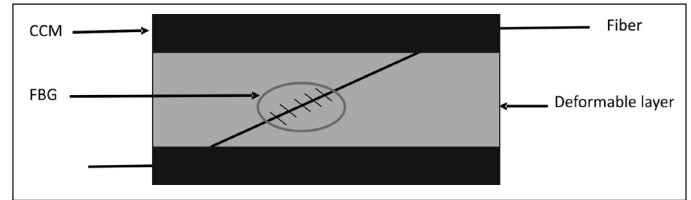

Figure 5 Introduction of deformable layer between the CCM layers increases the force sensing range of the sensor4.

This relative motion between the upper and lower layers will stretch the fiber embedded in between. Hence, the applied shear force results in a change of fiber length and thus changing the reflected Bragg wavelength. Therefore, this embedding technique ensures the transformation of shear strain to the axial strain of the fiber.

A simple temperature sensor can be fabricated by packaging the FBG within a small brass tube, of diameter 2mm, so as to enhance the thermal sensitivity and the temperature sensing range of the FBG as well as providing protection from external stress. Under temperature, the brass tube expands and stretches the fiber, resulting in the increase of grating periodicity, thereby, red shift of the Bragg wavelength. The bare FBG exhibited a sensitivity of 13 pm/°C at 1550 nm[16], however, the packaged sensor showed an increased temperature sensitivity of 15.08 pm/°C. These sensors have been used in structural health monitoring[17].

Based on these simple designs, various pressure, strain, temperature sensors have been fabricated and applied in practical applications such as structural health monitoring of civil and aerospace structures[17-20].

3.2 FBG in chemical sensing/ biochemical sensing

After successful applications of FBGs sensor for physical parameters, now FBG sensors are being explored for chemical and biochemical sensing for biophotonics applications[21]. In general, for chemical sensing, fiber cladding is removed and the evanescent wave interaction with surrounding media in monitored for sensing. A schematic sensor arrangement is shown in Fig. 6.
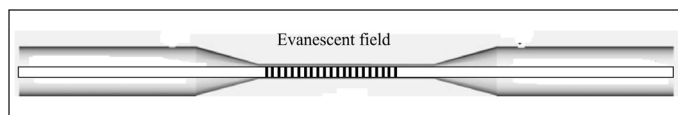
Fig. 6 Schematic of the etched FBG sensors (the cladding is removed and the measurand chemical is applied at the core surface)

A palladium (Pd)-coated elastooptic sensor was fabricated for hydrogen sensing[22]. In this sensor, a uniform FBG was coated with Pd. When the Pd –film absorbs hydrogen, it expands, thereby, stretching the fiber. The elongation of the fiber results a red shift in the wavelength. The amount of the wavelength shift is proportional to the hydrogen concentration. A linear shift was observed for hydrogen concentration of 0.3- 1.8%, with combined temperature and hydrogen concentration sensitivity of $0.00\%/H_2/°C$.

A highly sensitive refractive index sensor was reported by Liang et al[23]. The sensor consists of single etch-eroded FBG, the refractive index of ambient material can be measured by wavelength shift due to the change of effective refractive index. In the same work, another sensor was reported, which consists of two FBGs, forming fiber Fabry-Perot Interferometer. In the design, when the effective index changes, the resonance wavelength of the mth mode shifts accordingly. This design demonstrated a higher sensitivity to refractive index. Index change of up to $1.4×10^{-5}$ could be measured.

A temperature insensitive chemical sensor was reported by Sang et al[21]. The sensor consists of half-etch-eroded FBG. Due to half etching, the FBG peak splits into two peaks, corresponding to etched and non etched regions of FBG. The two peaks how similar shifts with temperature, however, due to concentration of the surrounding material, the peaks show different wavelength shift. Thus, the spectral separation acts as a function of the concentration of the surrounding chemical. Measurement of aqueous propylene glycol and sugar solutions were demonstrated successfully. Concentration changes of 0.067% and 0.027% could be achieved.

Recently Yang et al.[24] employed the FBG for measurement of aliphatic alcohol concentration and temperature. Their experimental results indicate that the proposed FBG sensor has a maximum sensitivity of 428.07 nm/refractive index units (RIU) at the RI value of 1.3265, a temperature sensitivity of 9.9 pm/°C, and a bandwidth sensitivity of 0.92 pm/°C is finding at methanol concentration of 10%. Kumar et al.[25] reported the use of clad etched FBGs to measure the dye concentration in dye-ethanol solution with a sensitivity of wavelength shift of 70pm/mM.

Recently, a sensitive detection of C-reactive protein is demonstrated using FBG[26]. In the sensor, and etched FBG is coated with grapheme- oxide complex, which is anti-C-reactive protein antibody. With the concentration of the C-reactive protein, the wavelength shifts. . A linear range of detection from 0.01mg/L to 100mg/L has been achieved.

Micro-structured FBG sensors have also been studied for sensing applications[27]. The micro-structured FBGs, consists of FBG as well as some microchannels in the fiber core. The optical characteristics can be drastically modified by the structure, pattern and refractive index within microchannels. Bertucci et al.[28] have demonstrated the successful detection of genomic DNA by these sensors.

3.3 FBGs in Harsh environments

Due to passive nature, FBG sensors have been explored for monitoring in harsh environment[13]. The sensors are ideally suitable for energy production applications as they are operable in harsh environment. High temperature measurement is required in gas turbine monitoring. Various types of gratings were employed for temperature monitoring[13, 29]. The UV laser induced gratings were erased at about 250°C, whereas weak and strong excimer laser induced gratings were erased in the range of 450 to 700°C. Type II gratings survived up to 800°C. Fs-IR laser induced gratings showed no measurable drift above 800°C. The sensor can be employed for measurement up to 100°C, after treatment in an annealing process[30]. However, above 1200°C, silica glass fibers are not suitable. In this temperature range, single crystal sapphire fiber may be used[31].

FBG sensor have been found suitable for monitoring in high radiation environment[13]. UV laser written FBGs in germanosilicated fiber have been found to be tolerant in low flux environment over a prolonged period[13, 32]. However, for high flux environment monitoring, germanosilicate fibers are found not suitable, as these are susceptible to radiation induced attenuation, which eventually makes the fiber opaque. In this environment, fluorine- doped radiation hardened fibers are found suitable. Fs-IR laser may be used to inscribe FBG in F-doped fibers[13, 32-34].

4. Conclusions

After successful demonstration of FBG sensors for measurement of physical parameters, FBG sensors are now utilized for chemical sensing. The evanescent field interaction with the surrounding media is utilized for sensing applications. Especially, micro structured FBG sensors have been explored for possible biophotonics application due to their large evanescent field and

compactness. FBG based system for measuring hydrogen, C-reactive protein, genomic DNA, concentration of various chemical substances such as alcohol, aqueous propylene glycol and sugar solutions etc. have been demonstrated successfully. FBG sensors have been proven to be suitable for harsh environment, such as radiation field and high temperature zone. This paper has presented chronological journey of FBGs from measurement of physical parameters to chemical and biochemical sensing as well as harsh environment monitoring. With their exceptional advantages such as robustness and immunity to EMI, FBG sensor technology has been proven in widespread industrial usage. However, the full potential of this technology has yet to be utilized. Especially, the microstructured FBGs have potential for multi parameter measurement and are explored as next generation sensing technology.

References

1. Byoungho Lee, "Review of the present status of optical fiber sensors" Optical Fiber Technology 9 (2003) 57–79.

2. A. D. Kersey, M. A. David, H. J. Patrick, M. LeBlanc, K. P. Koo, C. G. Askins, M. A. Putnam, E.J. Friebele, "Fiber Grating Sensors", J. *Light wave Techno.,* vol. 15, pp. 1442-1463, 1997.

3. Tjin, S. C., Hao, J., Lam, Y. Z., Ho, Y. C. and Ng, B. K. (2001), 'A pressure sensor using fiber Bragg grating', *Fiber and Integrated Optics*, vol. 20, no. 1, pp. 59–69.

4. Tjin, S.C., Suresh, R. and Ngo, N.G. (2004), 'Fiber Bragg Grating Based Shear-Force Sensor: Modeling and Testing', *Journal of Lightwave Technology*, vol. 22, no. 7, pp. 1728-1733.

5. Luyckx, G. , Voet, E. , Lammens, N. , Degrieck, J. , " Strain measurements of composite laminates with embedded fibre bragg gratings: Criticism and opportunities for research ", Sensors, Volume 11, Issue 1, January 2011, Pages 384-408

6. Li, Y. , Hua, Z., Yan, F. , Gang, P. , "Metal coating of fiber Bragg grating and the temperature sensing character after metallization" , Optical Fiber Technology, Volume 15, Issue 4, August 2009, Pages 391-397

7. Hao, J.Z. (2001), "Design and Fabrication of a Fiber Optic Pressure Sensor", Ph.D. Thesis, Nanyang Technological University, Singapore.

8. K.O.Hill, F. Fuji, D. C. Johnson, B. S. Kawasaki, "Photosensitivity in optical fiber waveguides: Application to reflection filter fabrication" *Appl. Phys. Lett.,* vol. 32, pp. 647-649, 1978.

9. G. Meltz, W. W. Morey, W. H. Glenn, "Formation of Bragg grating in optical fibers by a transverse holographic method", *Opt. Lett.,* vol. 14, pp. 823-825, 1989.

10. Hill, K.O., Malo, B., Bilodeau, F., Johnson, D.C., Albert, J., "Bragg gratings fabricated in monomode photosensitive optical fiber by UV exposure through a phase mask", Applied Physics Letters, Volume 62, Issue 10, 1993, Pages 1035-1037.

11. Larionov, Yu.V., Rybaltovsky, A.A., Semenov, S.L., Vartapetov, S.K., Kurzanov, M.A., Obidin, A.Z. "Photosensitivity of optical fibres doped with different Impurities" Quantum Electronics, Volume 34, Issue 2, February 2004, Pages 175-179

12. Atkins, R.M., Lemaire, P.J., Erdogan, T., and Mizrahi, V., "Mechanics of enhanced UV photosensitivity via hydrogen loading in germanosilicate glasses", Electronics Letters, vol. 29, no. 14, pp. 1234-1235, 8 July, 1993.

13. S. J. Mihailov, "Fiber Bragg Grating Sensors for Harsh Environments", Sensors 12, 1898-1918 (2012)

14. Kashyap, R., "Fibre Bragg Grating", Academic Press, 1999.

15. Rao, Y. J., "In-fibre Bragg grating sensors", Measurement Science Technology, vol. 8, pp. 355-375, 1997.

16. W.W. More, G. Meltz and W.H. Glenn, "Fiber optic Bragg grating sensors," *SPIE Proc.,* ed. 1169, pp. 89-106, 1989.

17. P. Moyo, J.M.W. Brownjohn, R. Suresh, S. C. Tjin, "Development of fiber Bragg grating sensors for monitoring civil infrastructure", Engineering Structures, vol. 27, pp. 1828-1834, October 2005.

18. Majumder, M., Gangopadhyay, T.K., Chakraborty, A.K., Dasgupta, K., Bhattacharya, D.K. "Fibre Bragg gratings in structural health monitoring-Present status and applications", Sensors and Actuators, A: Physical, Volume 147, Issue 1, 15 September 2008, Pages 150-164.

19. Ecke, W., Latka, I., Willsch, R., Reutlinger, A., Graue, R. "Fibre optic sensor network for spacecraft health monitoring", Measurement Science and Technology, Volume 12, Issue 7, July 2001, Pages 974-980.

20. Da Costa Antunes, P.F. , Lima, H.F.T., Alberto, N.J., Rodrigues, H., Pinto, P.M.F., De Lemos Pinto, J., Nogueira, R.N., Varum, H., Costa, A.G., De Brito André, P.S. , "Optical fiber accelerometer system for structural dynamic monitoring", IEEE Sensors Journal, Volume 9, Issue 11, November 2009, Article number 2026548, Pages 1347-1354.

21. Xinzhu Sang, Chongxiu Yu , T. Mayteevarunyoo, Kuiru Wang, Qi Zhang, Pak L. Chu, "Temperature-insensitive chemical sensor based on a fiber Bragg grating", Sensors and Actuators B 120 (2007) 754–757.

22. Boonsong Sutapun, Massood Tabib-Azar, Alex Kazemi, "Pd-coated elastooptic fiber optic Bragg grating sensors for multiplexed hydrogen sensing", Sensors and Actuators B 60 (1999) 27–34

23. Wei Liang, Yanyi Huang, Yong Xu, Reginald K. Lee, and Amnon Yariv, "Highly sensitive fiber Bragg grating refractive index sensors", APPLIED PHYSICS LETTERS 86, 151122 (2005).

24. H.Z. Yang, Q.X. Guang, R. Md. Islam, K.-S. Lim, H. Ahmad, "Simultaneous measurement of aliphatic alcohol concentration and temperature based on etched taper FBG", Sens. Actuators B: Chem. 202, 959–963 (2014)

25. J. Kumar, R. Mahakud, O. Prakash and S. K. Dixit, "HF-based clad etching of fibre Bragg grating and its utilization in concentration sensing of laser dye in dye–ethanol solution", Pramana 82, 265 (2014)

26. Sridevi S., K.S.Vasu , S.Asokan, A.K.Sood, "Sensitive detection of C-reactive protein using optical fiber Bragg gratings", Biosensors and Bioelectronics 65(2015)251–256.

27. Jun-Long Kou, Ming Ding, Jing Feng , Yan-Qing Lu, Fei Xu and Gilberto Brambilla, "Microfiber-Based Bragg Gratings for Sensing Applications: A Review", Sensors 2012, 12, 8861-8876.

28. Alessandro Bertucci, Alex Manicardi, Alessandro Candiani, Sara Giannetti, Annamaria Cucinotta, Giuseppe Spoto, Maria Konstantaki, Stavros Pissadakis, Stefano Selleri, RobertoCorradini, "Detection of unamplified genomic DNA by a PNA-based micro structured optical fiber (MOF)Bragg-grating optofluidic system", Biosensors and Bioelectronics 63(2015)248–254.

29. Willsch, M.; Bosselmann, T.; Flohr, P.; Kull, R.; Ecke, W.; Latka, I.; Fischer, D.; Thiel, T. Design of fiber optical high temperature senosrs for gas turbine monitoring. *Proc. SPIE* 2009, *7503*, 75037R1–75037R4.

30. Putnam, M.A.; Bailey, T.J.; Miller, M.B.; Sullivan, J.M.; Fernald, M.R.; Davis, M.A.; Wright, C.J. Method and apparatus for forming a tube-encased Bragg grating. US Patent 6,298,184, 2001.

31. Wang, A.; Gollapudi, S.; May, R.G.; Murphy, K.A.; Claus, R.O. Sapphire optical fiber-based interferometer for high temperature environmental applications. *Smart Mater. Struct.* 1995, *4*, 147–151.

32. Wijnands, T.; De Jonge, L.K.; Kuhnhenn, J.; Hoeffgen, S.K.; Weinand, U. Optical absorption in commercial single mode optical fibers in a high energy physics radiation field. *IEEE Trans. Nucl. Sci.* 2008, *55*, 2216–2222.

33. Aikawa, K.; Izoe, K.; Shamoto, N.; Kudoh, M.; Tsumanuma, T. Radiation-resistant single-mode optical fibers. Fujikura Tech. Rev. 2008, 37, 9–13.

34. Grobnic, D.; Henschel, H.; Hoeffgen, S.K.; Kuhnhenn, J.; Mihailov, S.J.; Weinand, U. Radiation sensitivity of Bragg gratings written with femtosecond IR lasers. Proc. SPIE 2009, 7316, 73160C.

Dr. Rupali Suresh received Master's Degree in Physics from IIT Delhi and PhD from Nanyang Technological University, Singapore. She is now working as Scientific Officer at Photonics and Nanotechnology Section, Atomic and Molecular Physics Division, BARC-Vizag.

Dr. K. Divakar Rao received his PhD in Physics from IIT Kanpur. He was associated with the Laser Biomedical Applications & Instrumentation Division at Raja Ramanna Centre for Advanced Technology till 2012 and currently he is with the Photonics and Nanotechnology Section at BARC-Vizag. His research interests include photonic materials, laser applications, nonlinear optics and biophotonics.

Thin film based optical coatings; materials and process issues

Chandrachur Mukherjee*, Rajiv Kamparath and Lala Abhinandan

Optical Design & Fabrication Laboratory, Raja Ramanna Centre for Advanced Technology, Indore – 452013, India.
*Email: cmukh@rrcat.gov.in; Tel: +91 731 244 2416; Fax: +91 731 244 2400.

Abstract

The very basis of optical coatings is stack of nanometric thin film layers of dielectrics, metals, ceramics, composites with defined microstructure that utilize the principle of interference governing amplitude, phase and polarization of the electromagnetic radiation. Technological and scientific applications linked to interference coatings especially lasers and associated technologies, heterogeneous coatings, metamaterials are enormous and are continuing to grow. Both material and geometric parameters are equally important in the description of optical coatings. Properties and behavior coating materials are discussed. Various process issues related to the development of specialized and challenging optical coatings developed at RRCAT and their characteristics are also discussed in this article.

1. Introduction

Applications for optical thin film interference coatings are numerous and continue to grow. For example, Mirrors in lasers, dense wavelength division multiplexer (DWDM) filters to enable fiber optic communications, optics for bar code scanners, fax machines and medical instruments, space shuttle windows and satellite solar covers, laser printers, CD-Rom drives, computer-driven projectors etc., all use optical thin film coatings. Optics and optical components with specialized optical coatings are important for laser based R&D and spectroscopic studies and also help in considerably enhancing the efficiency and hence usefulness of various laser based instruments, industrial and high power laser systems. These components are very expensive, not readily available and are mostly being imported. Development of large area optical coatings with high performance uniformity and high damage threshold as required for the development of high power lasers is a challenging task [1].

The nineteenth century saw a great deal of progress was being made in the field of interferometry. The most significant development, was the Fabry–Perot interferometer. In 1873, the great work of James Clerk Maxwell provide the basic theory for the analysis of thin film optical problems. Developments became much more rapid in the 1930s, the beginnings of the modern era of thin-film optical coating [2].

The most important factor in this sudden expansion of thin-film optical coatings was the manufacturing process. Although sputtering was discovered around the middle of the nineteenth century, and vacuum evaporation around the beginning of the twentieth, they were not considered as useful manufacturing processes. The main difficulty was the lack of suitable pumps. Since the development of diffusion pump oils, tremendous strides have been made,

particularly in the last few decades. Filters with greater than 200 layers, especially for optical communication, specialized branch of science and technology are not uncommon [3].

It is well known that a stack of thin layers of optical materials can preciously control the flow of light energy through the surface of a transparent solid on which layers are deposited. The behavior of the coating depends on the optical properties of the material together with interference effects, which vary with wavelength, angle of incidence and polarization. Only specular component of light is considered. As the incident light enters the system of optical thin film coatings, it suffers multiple internal reflections at each interface. All the reflected/transmitted component waves having a distinct amplitude and phase as decided by the multilayer stack, interfere either constructively or destructively to produce the resultant reflected/transmitted wave as desired. Such calculation is well organized and understood. However, the inverse problem is rather complicated and success depends equally on powerful theoretical tools, experience and skill. Design has to be finalized based on the practical problems faced in depositing such coatings and the limitations of the deposition and monitoring systems. The problem is compounded by the fact that properties of materials in thin film form vary on their own and also in the vicinity of another material [4, 5].

2. Optical Thin Film Materials: Dielectric materials

A typical transmission characteristic of an optical thin film material is presented in Fig. 1. Every material, because of its structure, has a characteristic transmission spectrum that can be split into three parts: (i) the high-frequency electronic absorption region, (ii) a transparent region, and (iii) a region dominated by the low-frequency lattice

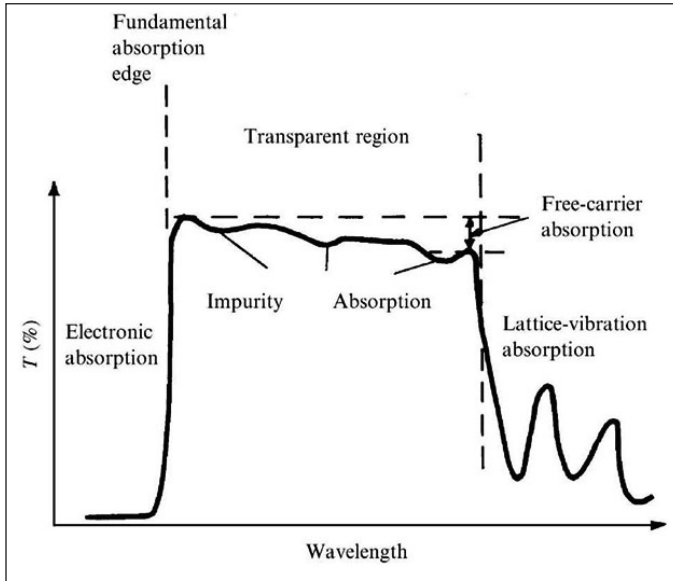vibration. The transparent region is particularly influenced by impurity and free-carrier absorption. [6]

Fig. 1. Wavelength dependent characteristic of a typical optical material used for interference coating [6].

Optical properties of substrates play a crucial role in deciding the ultimate optical performance of the coated surface Fig.2 shows the useful spectral band of various substrate materials.

In crystalline insulators fundamental absorption edge is determined by the band gap. 'A' indicates absorption by bound electrons. 'B' shows transparency range (Fig.3). Region 'C' indicates phonon absorption
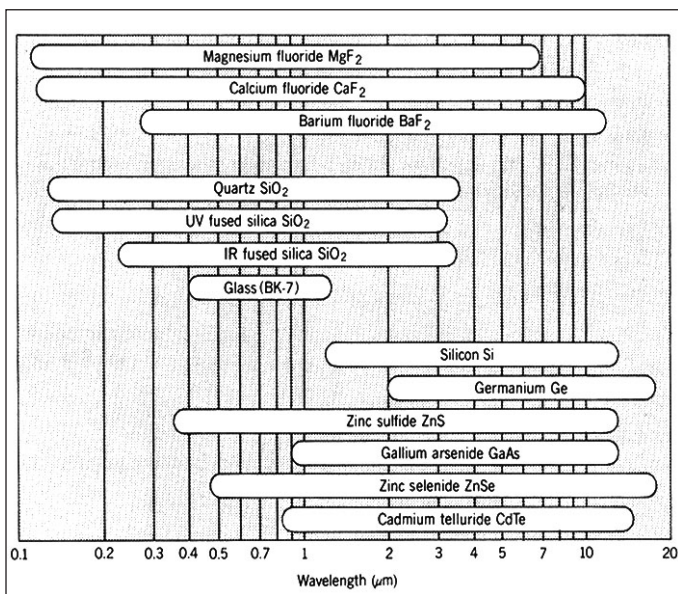

Fig. 2 The spectral band in which optical substrate materials are transparent [7].

or lattice absorption. 'D' denotes transparency range of CdSe. Optical properties of semiconductors are similar to those of insulators, expect that the electronic and photonic transitions occur at longer wavelengths. Its transparency range lies outside the visible spectrum, so it has a dark metallic appearance. Table 1. lists transparency range and refractive index of various crystals.
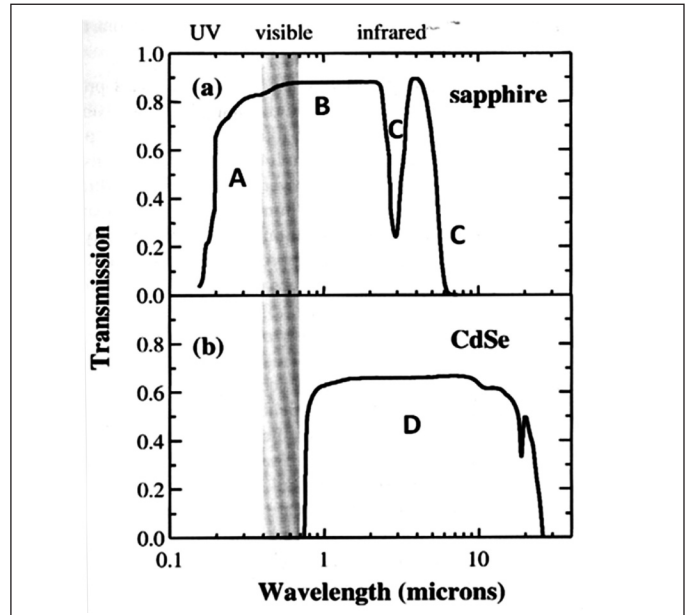

Fig.3: Transparency region in crystalline insulators[8].

Table 1: Transparency range and refractive index of various crystals[8].

Crystal	Transparency range (μm)	n
Al_2O_3 (sapphire)	0.2 – 6	1.771 (o), 1.763 (e)
BaF_2	0.2 – 12	1.476
Diamond	0.25 –> 80	2.424
KBr	0.3 – 30	1.564
KCl	0.21 – 25	1.493
KI	0.3 – 40	1.673
MgF_2	0.12 – 8	1.379 (o), 1.390 (e)
NaCl	0.21 – 20	1.55
NaF	0.19 – 15	1.326
SiO_2 (quartz)	0.2 – 3	1.546 (o), 1.555 (e)
TiO_2 (rutile)	0.45 - 5	2.652 (o), 2.958 (e)

There are a very limited number of materials available for optical coating applications. Out of these, a handful of materials are available for UV laser such as excimer lasers. Since the choice of coating materials for DUV/VUV is limited, this leads to whole range of constraints in the design as well as development of multilayer interference filters and coatings [1]. Moreover, the lack of proper high

index materials in the shorter wavelengths leads to a lower refractive index contrast (i.e., difference in the refractive indices, n_H and n_L). This in turn most often requires more number of layers and generates small reflection-band design solutions. Several fluorides with band gap energies ~ 10eV are suitable for UV (<200nm) applications e.g. AlF_3, CaF_2, Na_3AlF_6, GdF_3, LaF_3, NdF_3, MgF_2, etc. For visible range, MgF_2, CeF_3, Na_3AlF_6 are used. ThF_4 has been the natural choice in the IR range

Optical Refractory Oxides:

Refractory oxides are the most favorable materials for multilayer laser coatings and a list of popularly used coating materials is presented in table below.

Table 2. Refractory oxides for optical coating applications

Metal Oxide	Refractive index at 550nm	Transparency range (nm)	Melting point (°C)
TiO_2	2.31	450 – 10,000 nm	1850
Nb_2O_5	2.25	400 – 10,000 nm	1460
Nd_2O_3	1.79 – 2.15	400 – 2000 nm	2300
HfO_2	1.93 – 1.97	250 – 10,000 nm	2800
ZrO_2	2.05	270 – 7000 nm	2700
Sc_2O_3	1.85 – 1.90	220 – 10,000 nm	2300
Ta_2O_5	2.05 – 2.10	400 – 10,000 nm	1800
SiO_2	1.40 – 1.45	185 – 5000 nm	1710

Oxides are an important class of coating materials, because they generally form hard, abrasion resistant, chemically and environmentally stable film with a good variety of refractive indices and spectral ranges of high transmission. Many Oxides react at high temperatures, so liners are used. Since quiet a few oxides also dissociate at high temperature, reactive evaporation in oxygen atmosphere is required in most cases [1].

3. Optical coating process

Modern thin film multilayer optical coatings are usually fabricated by physical vapour deposition techniques in a vacuum chamber. Prior to deposition necessary substrates are polished and thoroughly cleaned by ultrasonic cleaning which is followed by vapour degreasing [7]. The vacuum chamber is also cleaned from residues of previous deposition runs. The substrates on which the thin films are to be deposited are mounted on a flat or a hemispherical plate called calotte. Deposition chamber is evacuated to a low pressure of 10^{-6} to 10^{-7} mbar. A small amount of oxygen is bled into the chamber during evaporation of refractory oxide materials. The substrates

may be at room temperature or they may be heated say upto 300°C. To ensure uniformity of the deposited film thickness over the coated area, the calotte is usually rotated about a central vertical axis, and the relative geometry of the source and substrates is carefully chosen [1, 2, 4]. Various coating processes include i) Thermal evaporation, ii) E-beam evaporation, iii) Plasma Assisted Deposition, iv) Magnetron Sputtering, v) Ion Beam Sputtering, vi) Sol-Gel process and so on.

3.1 Deposition of thin films by electron-beam evaporation

Traditional e-beam evaporation is one of the most widely employed method for producing thin films because large number of materials can be evaporated at reasonable cost of implementation. Here, a coating material is heated through e-beam bombardment, eventually vaporizes and finally re-condenses on all surfaces that are in a line of sight with the source. This method of evaporation is a relatively low energy process, and, as a result, the dielectric films are porous, of relatively low density, and exhibit a columnar structure. The problem with these porous films is that they can subsequently absorb moisture, which changes the refractive index of the layer(s) and thereby alters coating performance parameters (such as centre wavelength).

3.2 Ion assisted deposition (IAD)

IAD is a variant of the e-beam evaporation process which adds a high energy ion beam that is directed at the part to be coated. These ions act almost like an atomic sized hammer, producing a higher film density, higher mechanical durability, greater environmental stability and lower scatter than can be achieved with purely by evaporation alone. The ion beam can also be used to pre-clean or etch the surface of the substrate, which can improve film adhesion. IAD gives tremendous flexibility in the process. In particular, it enables the intrinsic stress of a coating to be modified during deposition, in some cases changing the overall film stress from tensile to compressive. This can help to maintain substrate surface figure, especially when depositing thick infrared coatings. It also extends the wavelength range over which the process can be used. Such a coating system is shown in Fig.4.

4. Thickness monitoring during deposition

Precise control of film thickness (to within 1% of the desired value) and controlled film deposition rate are essential during the fabrication process. The most common method for controlling the film thickness during deposition is by the optical interference method, where a chopped beam of light is allowed to fall on a witness substrate on which deposition is taking place. As the film
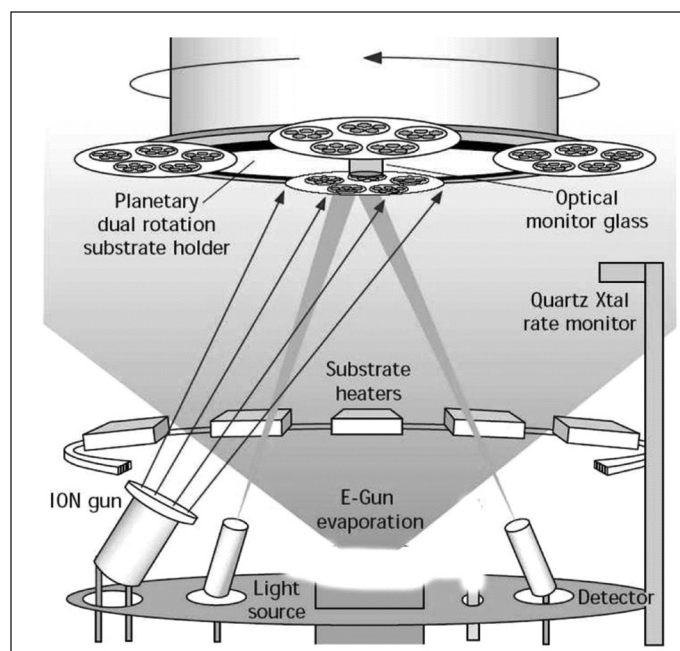
Fig. 4: A typical deposition system involving electron gun at the centre,ion source, in-situ optical and quartz thickness monitors[9].

grows on the substrate, the transmitted or reflected light intensity at a particular wavelength is monitored by the optical thickness monitor, fitted with a monochromator / filter and a detector. The measured transmittance or reflectance goes through a series of maxima and minima, and extrema being reached when the optical thickness is an integral number of quarter waves of the monitoring wavelengths. Additionally the physical thickness of the film being deposited is measured by a quartz crystal monitor, where an oscillating quartz crystal (frequency 5- 6 MHz) is exposed to the beam of material vapour, and as the film grows on it its oscillating frequency changes. This change in frequency is used to determine physical thickness of the deposited film. Therefore, one can monitor and measure both the physical thickness as well as the deposition rate of the film.

Optical quality of the growing multilayer can be continuously compared to the expected behavior and deviations from the target can be detected at an early stage of the process, where a correction may be feasible without sacrificing the coating batch. Feedback loop between process parameters and online monitoring ensures ultimate quality management in future optics production and helps in achieving high repeatability.

5. Laser resistance coatings

Development of optical components for lasers operating at very high power levels (terawatt level in pulsed systems and multi-kilowatt range in CW) at various wavelengths is a challenging task. This power handling capability of optical coatings is a major limiting factor. Today thin film laser damage research continues to focus on reducing absorption and coating defects. Telecommunication optics are being limited by laser damage issues as greater no. of photons are injected into small fibers. The need of semi conductor lithography industry for short wavelength coatings requires development of low absorbing materials in deep and extreme UV region. Mega projects like inertial confinement fusion, Free electron lasers, Air borne lasers have extremely high energy levels over large size optics. Short pulse lasers require coatings capable of withstanding pico-second and femto-second pulses. Coating design strategies such as standing wave electric field (SWEF) reduction technique and thick silica overcoat also improve laser resistance. SWEF reduction technique have immensely helped in using materials of different refractive index by reducing the SWEF peaks in the high index materials and also by shifting the peaks away from the interfaces. Reproducible and reliable measurements of LIDT (Laser Induced Damage Threshold) is essential for optimization of laser components. Damage in ultra short pulse region has been demonstrated to be mainly driven by direct electronic interaction of the material with intensive laser radiation involving tunneling, multi-photon and avalanche mechanisms. Films with pores, cracks, columnar microstructure, multiple crystalline phases, lack of stoichiometry lead to intrinsic defects. On the contrary extrinsic defect occur due to foreign defect seeds created during the coating process and due to surface contaminants present on the substrate. Therefore appropriate substrate and deposition system cleaning methods to be adopted to avoid such defects [1, 6].

6. High damage threshold broadband AR coating

Theoretically perfect anti-reflectance (AR) over a spectral and angle of incidence range can be achieved utilizing large number of non-quarter-wave layers. However, making such layer structure is extremely difficult. Therefore, design should be restricted to a limited no. of layers with thickness that can be deposited repeatedly with minimum run-to-run variation in thickness. We have optimized a four layer structure SUB/0.25H/0.4L/2.25H/1L/AIR, where H and L represents one quarter-wave TiO_2 and SiO_2 layers respectively. This layer structure yields a residual reflection loss nearly 0.2% per surface on a wavelength range over 240nm. In order to improve this, layer thickness were further optimized to SUB/0.25H/0.42L/2.3H/1.09L/AIR. This coating would provide reflection loss of 0.2% per surface over a larger wavelength range of 315nm. Electric field intensity profile along the depth of the multilayer is

calculated in both the cases and are shown in Figure 5. Electric field intensity profile provide insight about the laser damage phenomena [10].
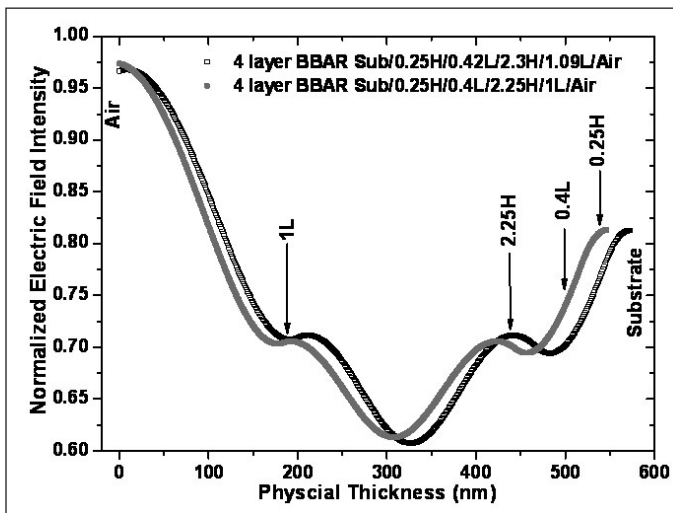

Fig.5. Calculated electric field intensity profile along depth of the multilayer for two different layer structures.

Damage threshold testing using high power Nd:YAG laser

High power Nd:YAG laser (average power 500 W, 10kW peak power, 2-40ms pulse duration, 1-100 Hz frequency and 10 - 300 J pulse energy) is used for damage testing the AR coated optics. The coating could sustain long duration pulses as well as very high pulse energy (300 J, 1.3Hz). The optics was tested starting from single shot exposure to 100 shots exposure using maximum energy pulse. Further, the laser beam was focused to produce a spot diameter of 400 μm on the coated optics. It could sustain peak power density of up to ~ 6 MW/cm² for long duration pulses (300J, 40msec). These measurements suggest that the coatings are free from absorption sites. LIDT tests were repeated at various sites on the coated optics [10].

7. Coatings for air-spaced & solid etalon

An etalon is an optical interferometer in which a beam of light undergoes multiple reflections between two parallel reflecting surfaces, and whose resulting optical transmission is periodic and narrowband in wavelength. Development of narrow line-width tunable dye laser requires etalons. For this an eight layer dielectric coating was designed, in which the last layer was non quarter-wave. Coatings were made on 50mm diameter, 10mm thick fused silica optical flats (~λ/50). Special precaution was taken during substrate loading, substrate heating, cooling and chamber venting so that surface figure can be maintained even after completing the entire coating

process. Finesse ≈ 24 @ 632.8 nm, for an air spaced Fabry-Perot was achieved. Similarly for solid etalon and finesse ≈ 26 @ 632.8 nm is measured. Reflectivity limited finesse of this multilayer coating is ~28.

8. Development of tunable fabry-perot (F-P) filter

Wavelength division multiplexer / demultiplexer (WDM/WDDM) is the key component in optical communication. Using thin film fabry-perot filter wavelength demultiplexing / tuning can be achieved by varying the spacer layer thickness [11]. The spacer layer thickness was varied from 125 to 160nm across a 25mm dia. substrate. 9 channels each of FWHM = 3nm can be placed each, 2mm apart from the previous channel on the substrate along the direction of shutter motion. Tuning of 21nm is achieved. Fig.6. shows the transmission spectra of a 17 layer F-P filter with high refractive index spacer layer (thickness = 4*λ/4 @ 465nm plus a tapered layer varying from 0 to 33nm) [12].
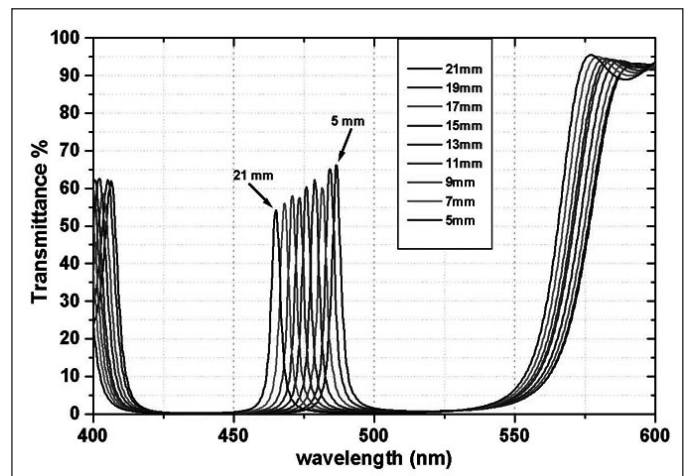

Fig.6: Transmission spectra of 17 layer F-P filter with a graded spacer thickness varying from 0 to 33nm.

9. Effect of moisture on thin film fabry-perot filter

Ultra-high-precision band pass filters employed in DWDM requires the quantification of film stability against fluctuations in environmental conditions. A newly deposited under-dense film will display a spectral shift to longer wavelengths while still under vacuum due to the adsorption of H_2O from the residual gases present in the evaporator [13, 14]. In this initial uptake of moisture, H_2O molecules are chemisorbed onto the inner walls of the film's voids. This initial moisture-induced spectral shift is considered irreversible due to the inherent difficulty of breaking the chemical bonds associated with chemisorption. A second spectral shift to longer wavelengths occurs upon exposure of the film to atmospheric conditions [15, 16]. The second moisture shift is due to the condensation of

H_2O vapor into the voids of the film and is understood as a change in the film's effective refractive index.

The peak transmission wavelength of a narrow band-pass fabry-perot filter is used in this study to find out the effect of moisture immediately after deposition and after long exposure in ambient atmosphere. Therefore, 13 layer F-P filters are deposited. Design and monitoring wavelength was 470nm.

Films were deposited in a fully automated ion assisted, e-beam evaporation system. TiO_2 and SiO_2 are independently evaporated from two e-beam guns. Substrate temperature during deposition was maintained at $150^o\pm1^oC$. Deposition rates were controlled with a stability of 5 ± 0.1 Å/s. Ion assisted deposition was carried out using high purity (99.9995%) O_2 (40sccm) and Ar gas (10 sccm). Discharge current & voltages used were 3A, 150V for SiO_2 deposition and 5A, 150V for TiO_2 deposition. These parameters yielded reasonably dense films. Deposition pressure was maintained at $2x10^{-4}$mbar using a throttle valve and capacitance manometer combination.

Fig.7 shows the transmission spectra of a 13 layer F-P filter measured, immediately after deposition was taken at 150^oC under vacuum and shows peak transmittance of 82.5% at 470nm. After approximately 2hrs the system got cooled down to 30^oC and the peak shifted to 472nm. Afterwards the chamber was vented with dry N_2, samples were kept at ambient for 12hrs and again transmission measurement was taken. Peak transmission of 87% is measured at 496nm. This shows a red shift of 26nm. Then sample is fitted back to the test glass position and kept under vacuum for 24hrs. Transmission peak blue shifted to 480nm. Therefore due to chemisorption of H_2O, 10nm i.e. nearly 2% peak shift is observed and for physisorption additional 16nm i.e. 3.3% red shift is observed [17].
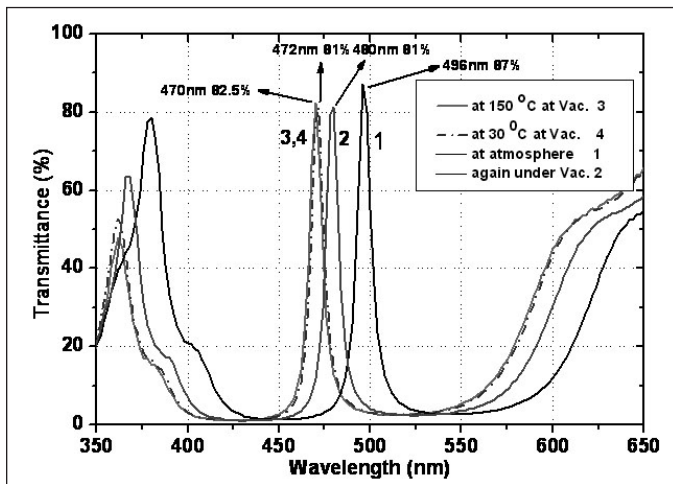

Fig.7. Transmission spectra of a F-P filter at different environmental conditions.

10. Effect of ion beam on morphology of optical thin films

For high power Nd:YAG and diode laser applications MgF_2 and Al_2O_3 thin films are extensively used as anti-reflection coatings respectively. Energetic deposition techniques like Ion assisted deposition is used to make dense film with low optical absorption. Effect of ion beam parameters, on optical performance and morphology are studied.

Figure 8 shows the transmission spectra of MgF_2 films grown at 5 Å/s and 100^oC with and without ion-assist (Ar ion) on BK-7 substrate. Systematic variation of both
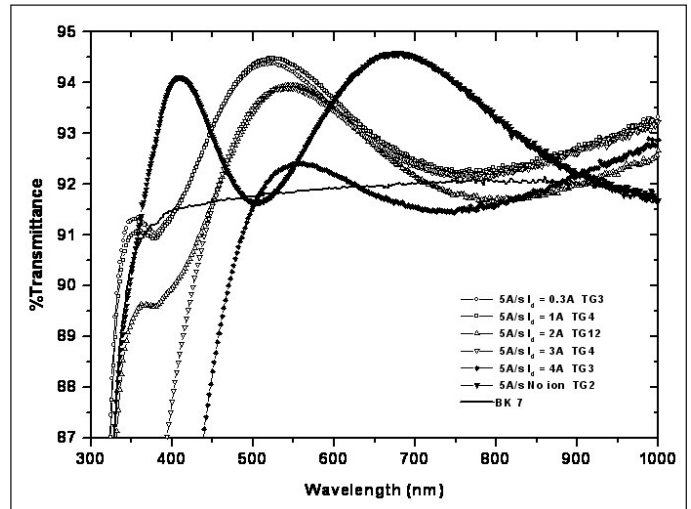

Fig. 8. Transmission spectra of MgF_2 films grown at 5Å/s & 100 ^{o}C.
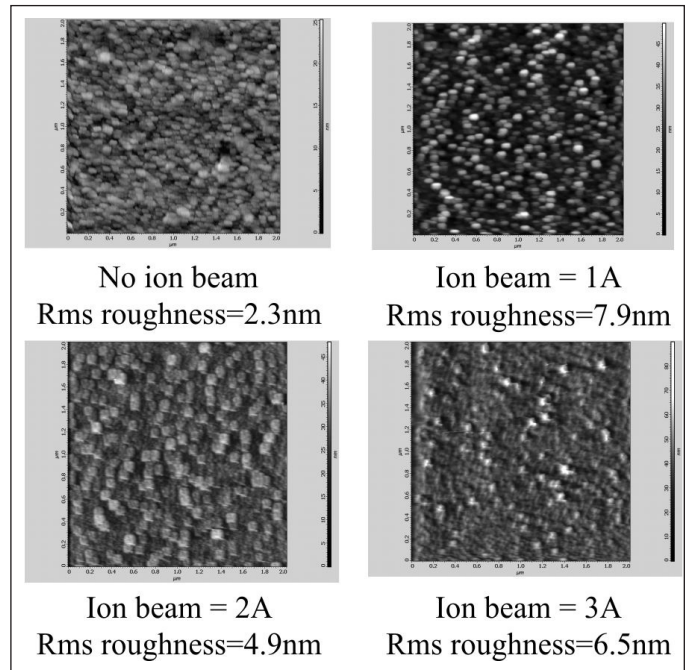

Fig. 9 Surface morphology of MgF2 films grown at 5 Å/s at various ion beam parameters.

ion beam current and ion energy are carried out. Use of 1A of anode current is found to be optimum to obtain homogeneous and good optical quality MgF_2 film grown at 5Å/s with rms roughness 7.9nm. Increase of I_d from 1A to 2A increases overall absorption in the film. Further increase of I_d drastically increases absorption in the film. This may be due to increasing fluorine loss from the film thereby increasing Mg concentration [18, 19]. I_d of 1A is found to be beneficial as far as ion-assisted deposition of MgF_2 is concerned [20].

In fig. 9 film grown without ion assist (top left) grow in a typical columnar microstructure consisting of tiny columns grown side by side with low inter-columnar voids with a roughness of 2.3nm. Roughness increases more than 3 times by using only 1A ion beam current with nearly similar columnar structure as that of film grown without ion beam. With further increasing I_d, roughness decreases and then again increases. LIDT improves from 14 J/cm^2 (no ion) to 19 J/cm^2 (ion beam current = 1A) [20].

Al_2O_3 films grow with much lower surface roughness than MgF_2 films. Surface morphology of the films grown without ion beam also show columnar microstructure. Use of high ion flux leads to denser film. The films were found to be of high optical quality in the measured wavelength range. Films are hard, durable and adherent to the substrate. Use of optimised ion flux (3A, 150V) leads to dense and smooth (rms roughness = 0.4nm) Al_2O_3 film. There is no one to one correspondence between morphology and ion beam parameters [21].

11. Analysis and crosscheck of optical properties based on spectrophotometric and ellipsometric measurements

Spectrophotometric and ellipsometric methods are popularly used for characterization of thin films. Spectrophotometric method determines the spectral dependencies of reflectance and transmittance of thin films. Ellipsometric method analyzes changes in the state of polarized light that has been reflected / transmitted from films.

Ellipsometry measurement provide optical constants (n, k) and thickness (d), through a model-based analysis[1]. The obtained n, k and d values can be used to generate transmittance & reflectance curves for the same thin film. To check, the correctness of n, k and d values as obtained by the above method (ellipsometry analysis), we have generated a computer code to theoretically calculate transmittance and reflectance spectra. This calculated spectra is compared with the transmittance curve of a thin film obtained experimentally using a commercial spectrophotometer. For this analysis a software (ELLIP-SPECTRO ANALYSIS) has been developed based on Matrix Method [22].

12. Recent developments in heterogeneous coatings

Any optical coating with a refractive index that depends on the spatial coordinates is considered as heterogeneous coating. Grating – waveguide structure / Guided-mode resonance (GMR) filter is one such structure. A three layer GMR filter consists of top grating layer, then waveguide layer and then sub-waveguide layer coated on the substrate. The remarkable property of a grating waveguide (GWG) is that it can show a reflectivity of 100 % for a given optical wavelength despite its thickness of typically less than a wavelength. coatings in gravitational wave detectors, because only a very small amount dielectric coating material is required with a corresponding considerable reduction in coating thermal noise. Raman notch filters can also be made using such structures [5].

Metamaterials: The development of electromagnetic, artificial-lattice structured materials (photonic crystals), termed metamaterials, has led to the realization of phenomena that cannot be obtained with natural materials. The metamaterial coating consists of a mesh and an electric split-ring resonator array separated by a dielectric spacer layer (~ 10μm). Structured metamaterials can achieve negative refraction using nano-fabricated materials in terahertz region [23].

4. Conclusions:

There are all round tremendous progress in the field of optical interference coatings, primarily due to available of powerful computers, electronics controls and instrumentation and novel process control formulations. The rapid growth in material science and technology has also added extra dimension as well as scopes to this pioneering branch of the optical technology. Demanding requirements due to ultra-fast, ultra-short pulse lasers, high peak power and high repeating lasers have also compelled this technology to adopt newer design, deposition and characterization techniques. Challenging requirements of fiber optics communication, Optical-MEMS (acronym for Micro Electro Mechanical Systems), Quantum-computing, nanophotonics and Terahertz science and technology have added several new dimensions as well challenges to its growth.

Acknowledgements:

References

1. Norbert Kaiser and H. K. Pulker, Optical Interference Coatings, Springer, (2003).

2. H.A. Macleod, Thin-Film Optical Filters, Third Edition, IOP, (2001).

3. H. K. Pulker, Coatings on glass, 2nd edition, Elsevier, (1999).

4. Ronald R. Willey, Practical Design and Production of Optical Thin Films, Second Edition.

5. Optical Coatings, Materials aspect in theory and practice, by Olaf Stenzel, Springer Vol.54 2014.

6. R.M. Wood, Laser damage in optical materials, Adam Hilger, 1986.

7. J.D. Rancourt, Optical thin films user handbook, SPIE 1996.

8. A. Mark Fox, Optical properties of solids, Oxford University Press, New York (2001).

9. A. Czajkowski, Optical coating technology and application: past and present to future, Photonic International, 2010.

10. C. Mukherjee, K. Rajiv, B.N. Upadhyaya, P. Misra, S.M. Oak and J.K. Mittal, National Laser Symp.-2010, RRCAT-Indore, (2010).

11. J.A. Wahl, J.S.Van Delden and S. Tiwari, IEEE Photonics Tech. Lett., 16 (2004).

12. C. Mukherjee, A. Joseph, K. Rajiv and U. Nundy IN Int. conference on PHOTONICS-2006, University of Hyderabad, Hyderabad, (2006).

13. 1. H.K. Pulker and E. Jung, Thin Solid Films, 9, 57 (1971).

14. P.J. Martin, H.A. Macleod, R.P. Netterfield, C.G. Pacey and W.G. Sainty, Appl. Opt. 22 (1) 178 (1983).

15. S. Ogura & H.A. Macleod, Thin Solid Films 34, 371 (1976).

16. D. E. Morton, V. Fridman, 41st Annual Tech. Conf. Proc., Society for Vacuum Coaters, 297 (1998).

17. C. Mukherjee, K. Rajiv and J.K. Mittal, National Laser Symp.-2007.

18. J. D. Targove, PhD Thesis, TheUniversity of Arizona, 1987.

19. L. Dumas, E. Quesnel, F. Pierre and F. Bertin, J. Vac. Sci. & Tech. A20 (2002) 102.

20. C. Mukherjee, K. Rajiv and R. Sundar, Int. Conf. on Opt. & Optoelectronics Proc. ICOL-2005 (2005).

21. C. Mukherjee, K. Rajiv & J.K. Mittal, Int. Conf. on fiber optics & photonics, PHOTONICS-2010, IGuwahati, (2010).

22. K. Rajiv and C. Mukherjee, IN National Laser Sysmposium-2006, RRCAT, Indore (2006).

23. Alexei A Maradudin, Cambridge University Press, (2011).

	Dr. C. Mukherjee received B.Sc & M.Sc in Physics from The University of Burdwan in 1989 and 1991 respectively. He obtained M.S (Physical Sciences) from Birla Institute of Technology & Science (BITS), Pilani in 1994. He carried out his doctoral research in Amorphous Silicon thin films under the supervision of Dr. R. Bhattacharyya at The National Physical Laboratory, New Delhi. He did his post doctoral work at the University of Kaiserslautern, Germany during 2000-2001. He joined Raja Ramanna Centre for Advanced Technology in 1996. His current research interests include Thin films, optical coatings, laser damage threshold, ultra low loss coatings over large area etc.
	Rajiv Kamparath did B.Sc (Physics) from Calicut University, Kerala in 1991. He joined Raja Ramanna Centre for Advanced Technology in 1992. He is actively involved in setting up of multilayer thin film deposition system and characterization setup for multilayer coatings. His main interest is in the area of design and characterization of thin film coatings, programming, laser damage threshold etc.
	Dr. Lala Abhinandan graduated in Chemical Engineering from IT BHU, Varanasi in 1977 and upon completion of training joined BARC, Mumbai. Since 1986, he has been working at RRCAT, Indore on various R&D projects including high power CO_2 laser, CVL, excimer laser etc. He was awarded PhD in 1999 by IIT, Bombay for his work on Laser Curing of Powder Coatings. In 2001, he also worked in Fraunhofer Institute for Applied Polymer Science at Potsdam, Germany. Dr. Lala is now heading the Mechanical and Optical Support Section at RCCAT. He is a Principal Investigator in a solar energy project run by CSIR. He is also a faculty and M.Tech guide at HBNI and IIT, Rajasthan.

Reduction of vanadium-manganese-oxide thin films and its effect on structural, electrical and optical properties

Girish M. Gouda

Laboratory for Electro-Optics Systems (LEOS), Indian Space Research Organization (ISRO),
First Cross, First Stage, Peenya Industrial Estate, Bengaluru 560058, India
E-mail: girish@leos.gov.in
Tel: +91-80-2268 5234

Abstract

Vanadium-manganese-oxide thin films which have 96.7 % and 3.3 % atomic concentrations of vanadium and manganese respectively have been subjected to a reduction process under hydrogen atmosphere at 673 K for a duration of 240 minutes. The virgin thin films are amorphous and become crystalline after the reduction process and there are crystalline phases due to VO_2, V_2O_5 and MnV_2O_6. The surface morphology study of reduced thin films by atomic force microscopy shows enhanced grain size compared to that of virgin films. The electrical and optical characteristics follow a behaviour similar to those of VO_2 material, but a semiconductor to metal type of transition occurs at 333.5 K. The rate of change of electrical resistance and optical transmittance with respect to temperature is found to be shallower compared to single crystal and polycrystalline VO_2. The optical absorption studies show that the absorptance of reduced thin films is higher over the entire spectral range and is attributed to increased low level defect centres within the forbidden optical band gap due to the reduction process.

Keywords: V-Mn-O thin films, reduction, semiconductor to metal transition, electrical property, optical property, transition temperature, optical band gap

1. Introduction

Vanadium oxide exists in several forms such as vanadium oxide (VO), vanadium trioxide (V_2O_3), vanadium dioxide (VO_2) and vanadium pentoxide (V_2O_5), due to multi-valence of vanadium[1, 2], out of which VO_2, V_2O_3 and V_2O_5 have been widely studied[3-8]. Within these materials, VO_2 has shown change in crystalline phase from monoclinic to tetragonal at a temperature of transition (T_c) close to 340 K[1-4]. The structural transformation is associated with changes in electrical and optical properties. The electrical properties of VO_2 are typical of semiconductors at room temperature (300 K) and after transition follow the trends of metallic materials with similar changes in optical properties, namely increased optical absorption in the infrared region[3, 4]. Because of these specific changes in electrical and optical properties, the structural transformation is widely referred as Semiconductor to Metal Transition (SMT).

Investigations have been focussed on introduction of dopants such as W^{6+}, Nb^{5+}, Al^{3+} and Cr^{3+} and their effect on phase transformation characteristics and associated electrical and optical properties[4-6]. It was observed that higher valence dopants, namely W^{6+} and Nb^{5+}, increase the T_c, whereas lower valence dopants Al^{3+} and Cr^{3+} produce the opposite effect. This is attributed to change in free electron density and electron-electron correlation which shields the lattice effect[7, 8]. Our critical survey of the literature has shown that there are no studies carried out so far on the effect of addition of Mn dopant on SMT of VO_2. It is however anticipated that doping with a low concentration of Mn, will affect the free electron density and electron-electron correlation and hence the SMT characteristics. In this paper, we present the experimental details of preparation of thin films of mixed oxides of manganese and vanadium, with a low concentration of manganese oxide, followed by annealing the thin films in a reduced atmosphere at a high temperature. Then, the paper is devoted to the results of the investigation on structural, electrical and optical properties, highlighting the intricate results of SMT of reduced thin films and their comparison with similar results reported in the literature.

2. Experimental

2.1 Preparation of reduced thin films

The coating material in the form of sintered flakes has been prepared by the solid state sintering technique which is, in general, applicable for mixed oxides of manganese and vanadium, ranging from 'manganese-rich' to 'vanadium-rich'. The preparation technique has been discussed in detail elsewhere[9]. The sintered flakes consist of manganese vanadate (MnV_2O_6) and vanadium pentoxide (V_2O_5), as revealed by X-ray diffraction analysis[9].

The sintered flakes are used as the coating material for deposition of thin films by electron beam evaporation technique under a high vacuum condition, with a base pressure better than 2×10^{-6} mbar[10]. The deposition is carried out at an elevated substrate temperature of 523 K and at a chamber pressure of 4×10^{-6} mbar and the deposited film thickness is 250 nm. Then the thin films have been annealed at 673 K in an air fired furnace for a duration of 180 minutes which here after referred as Annealed Thin Film (ATF) samples. The ATF samples have been further subjected to a high temperature annealing under reduced atmosphere at a temperature of 673 K for a duration of 240 minutes. The samples were placed in an horizontal tube furnace, Elite model TSH 15/50/180 and ultra high pure (99.999 %) argon (Ar) and hydrogen (H_2) gases are introduced into the furnace through separate mass flow controllers in the ratio of 50:50. The samples are allowed to reach ambient temperature under normal cooling condition. They are here after designated as Reduced Thin Film (RTF) samples. Both ATF and RTF samples have been used to characterize their chemical and physical properties.

2.2 Characterization of thin films

The crystalline structure of ATF and RTF samples have been characterized using a Phillips, Model PW1140/90 X-ray diffractometer (XRD) which uses copper K_α line (λ = 1.54056 Å) as the source. X-ray diffraction lines have been compared with the JCPDS-ICDD data to identify the different phases and their corresponding crystalline structures. The surface morphology of thin films has been studied using an atomic force microscope (AFM), Thermoscope Autoprobe M5, from which the grain size is determined. In this analysis, the samples are scanned, in contact mode, over an area of 50 µm × 50 µm. The elemental composition is determined using an energy dispersive x-ray analyser (EDAX) from Oxford Instruments attached to Leica S440i scanning electron microscope (SEM).

Thin film samples deposited on pyrex substrates have been used for the characterization of electrical properties for which metallization pads of suitable geometry, with electrical leads, are prepared using a two component silver epoxy material, EPOTEK H20E, such that the aspect ratio is equal to one. The electrical resistance of the thin film samples has been determined using a Keithley digital multimeter, Model 2000 with the samples kept in an air circulated oven at a temperature varied from 298 to 423 K, in steps of 5 K. The sample temperature is measured and controlled within an accuracy of ± 0.5 K using a copper-constantan thermocouple mounted close to the samples. The resistance measurements have been carried out over a minimum of five cycles of temperature variation, the average of which, at any particular temperature, is taken as standard resistance value. The specific resistivity is calculated form the measured resistance.

The transmittance (T) and reflectance (R) properties of ATF and RTF samples have been measured using a PerkinElmer Lambda950 spectrometer. From the measured R and T values at a given wavelength λ, the absorption index is deduced using the relation[11],

$$\left(\frac{1-R}{T}\right)=\exp\left(\frac{4\pi kd}{\lambda}\right) \tag{1}$$

where 'k' is the absorption index and 'd' the geometrical thickness of the thin film determined a priori using an AFM. The optical transmittance of RTF samples have been measured at different temperatures, ranging from 298 to 368 K using the same spectrometer but making use of a special temperature cell, in the optical path of the instrument. After inserting the temperature cell, the instrument is calibrated for 100 % baseline without the sample which is followed by transmittance characterization at room temperature as well as elevated temperatures, over the wavelength range from 400 to 2500 nm. During these scanning, the temperature of sample is monitored and controlled within ± 0.5 K.

3. Results and Discussion

3.1 Crystal Structure and surface morphology

The atomic concentrations of Mn and V of ATF samples, as revealed by EDAX, are respectively equal to 3.3 % and 96.7 % respectively. The ATF samples are amorphous[10] however, after annealing under reduced atmosphere at 673 K for four hours they become crystalline as shown by the XRD results presented in Figure 1. The observed d spacing values are compared with JCPDS-ICDD data[12-14] and the identified crystalline phases are presented in Table 1. It is obvious that there are peaks due to VO_2[12], V_2O_5[13] and MnV_2O_6[14]. Several investigators have studied the problem of reduction of vanadium oxides under different thermal conditions, such as annealing thin films of V_2O_5 in vacuum
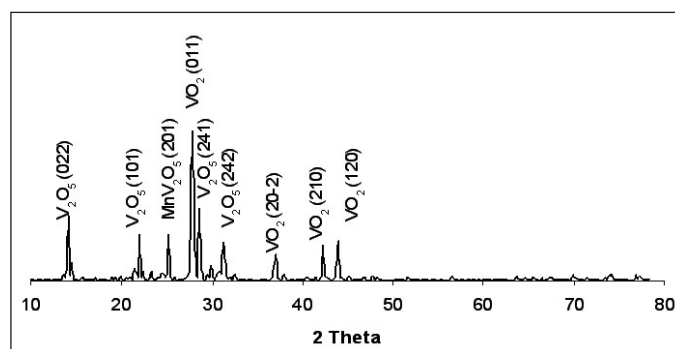

Figure 1: XRD pattern of reduced thin film sample.

Table 1: d-spacing and the phases present in reduced thin film

d (Å)	Phase	hkl	PDF No
6.2777	V_2O_5	022	45-1074
4.0891	V_2O_5	101	41-1426
3.5444	MnV_2O_6	201	40-0165
3.1957	VO_2	011	44-0252
3.0938	V_2O_5	241	45-1074
2.8406	V_2O_5	242	45-1074
2.4308	VO_2	20-2	44-0252
2.1335	VO_2	210	44-0252
2.0566	VO_2	120	44-0252

at temperatures ranging from 373 to 973 K [15] and reduction of sol-gel synthesized V_2O_5 in hydrogen stream[16]. It was reported that V_2O_5 material undergoes a transformation from amorphous to crystalline phase at temperatures higher than 673 K and, at temperatures greater than 723 K it gets reduced to lower oxide species[17, 18]. Similarly, tungsten (W) doped vanadium oxide amorphous thin films prepared by chemical synthesis become crystalline on heating to 773 K under H and Ar atmosphere for two hours[6]. It was also reported that W doped V_2O_5 crystalline material, on exposure to still higher temperature up to 923 K for five hours transformed to crystalline VO_2 having higher inter-planar spacing[5]. The ATF samples of the present investigation consist of MnV_2O_6 and V_2O_5 existing in an amorphous state as inferred from the authors' earlier investigation[10]. On exposure to reduced atmosphere at 673 K for a period of four hours a rearrangement of the oxygen polyhedra takes place, similar to that of vanadium oxide[17], leading to the growth of crystallites of MnV_2O_6 as well as other oxides of vanadium. Also during this process V_2O_5 gets reduced to VO_2 either wholly or partially and crystallites of both VO_2 and V_2O_5 grow further. All these processes ultimately produce reduced thin films (RTF) which consist of co-existing crystalline MnV_2O_6, VO_2 and V_2O_5. The results of the surface morphology of ATF and RTF samples by AFM are presented in Figure 2; the
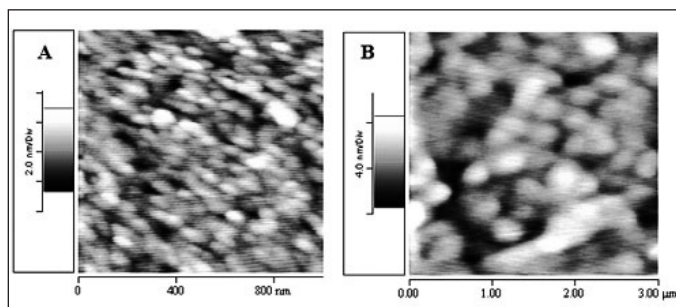

Figure 2: AFM topographic images of (A) ATF and (B) RTF samples.

grain sizes of RTF samples are considerably larger and there are changes in the grain shape. The average grain size is 325 nm for RTF and 76 nm for ATF. These results have substantiated the XRD results presented earlier. The AFM topographic image shows some elongated structures along with distorted circular granules which are attributed to V_2O_5, since V_2O_5 tends to exhibit needle like crystalline morphology when it is annealed at a higher temperature[9].

3.3 Electrical Properties

The results of the variation of electrical resistivity of RTF samples with temperature is shown in Figure 3 in which the data on heating and cooling cycles are presented together. A comparison of the present data with that of ATF samples, presented in the inset, shows the following differences in the electrical resistivity characteristics:
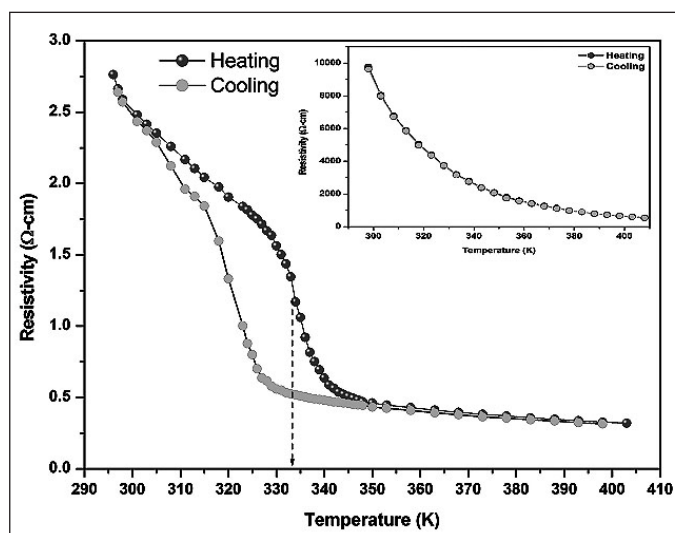

Figure 3: Resistivity as function of temperature for heating and cooling cycle of RTF; the inset gives that of ATF.

1. The room temperature resistivity of RTF samples is three orders of magnitude lower than that of ATF samples.

2. The electrical resistivity of RTF samples shows a transition from a higher to a lower value with an order of magnitude changes at a transition temperature around 333.5 K.

3. There is an hysteresis behaviour in RTF samples in which a lower value is observed during cooling.

4. There exist two activation energies, namely 0.115 eV (before T_c) and 0.076 eV (after T_c).

In order to understand the intricacy of electrical characteristics of RTF samples, the measured electrical parameters are compared in Table 2 with those of ATF

Table 2: Comparison of structural and electrical characteristics of RTF, ATF, MV12 and Vanadium Oxides

Material	Electrical Resistivity (Ω-cm)	Activation energy (eV)	Structure/ Phases present	Ref
RTF	2.5 (before transition)	0.115	Crystalline: VO_2, V_2O_5 and MnV_2O_6	Present work
	0.5 (after transition)	0.076		
ATF	8.01×10^3	0.274	Amorphous: probable phases MnV_2O_6 + V_2O_5	10
MV12	6.54×10^2	0.140	Crystalline: MnV_2O_6 + V_2O_5	9
V_2O_5	3.36×10^2	0.238	Amorphous	9
V_2O_5	10^3-10^4	0.21-0.26	Crystalline	19-21
VO_2	1.0 (before transition)	0.290	Monoclinic	21
	10^{-3} (after transition)	0.099	Tetragonal	

Table 3: Comparison of semiconductor to metal transition parameters

Material	ΔT (K)	T_c (K)	N_R	Remarks	Ref
RTF on pyrex substrate	16.0	333.5	10	Mixed crystalline phases of VO_2, V_2O_5 and MnV_2O_6	Present work
VO_2 on mono-crystalline sapphire	3.0	337.0	10^4	--	23
VO_2 on Sital (Si-Ti-Al-O) ceramic substrate	10	348.0	10	ΔT depends on the size of the crystallites	23
VO_2 doped with tungsten (W)	10	300.0	10^2	1 atomic % of W decreases T_c by 23 K	4
VO_2 doped with niobium (Nb)	10	315.0 (x=0.02)	10	$V_{1-x}Nb_xO_2$, $0.02 \leq X \leq 0.1$, T_C decreases with increase of x	24

samples, the parent MV12 material used for preparation of ATF and, V_2O_5 and VO_2 materials obtained from our own investigation[9, 10] as well as from other studies reported in the literature[19-22] respectively. The activation energy of conduction for RTF samples before T_c is close to that of the parent MV12 material, which consists of V_2O_5 and MnV_2O_6, but it is lower by 0.025 eV [9]. The electrical resistivity of RTF follows the typical characteristics of VO_2 material[1-3], even though it is a composite of MnV_2O_6, V_2O_5 and VO_2. This is due to the fact that VO_2 is one of the major phases in RTF samples, as shown by the XRD results. After the transition, the activation energy is equal to 0.076 eV for RTF samples, a value close to 0.099 eV observed in polycrystalline VO_2 thin films[22]. From the resistivity results of Figure 3, the following parameters are calculated: $\Delta T = T_a$-T_b, $T_c = (T_a + T_b)/2$, and $N_R = R_a/R_b$, where T_a is the temperature at which the resistance of the thin film starts to decrease rapidly, T_b is the temperature at which the rapid decrease of resistivity ceases, R_a is the resistance at temperature T_a and R_b is the resistance at temperature T_b. Both ΔT and N_R can be used to quantitatively assess the sharpness of transition. ΔT, T_c and N_R are compared with the corresponding results for

pure and doped VO_2 materials reported in the literature[4, 23, 24] in Table 3, from which following the observations can be made:

1. The transition is less sharp in RTF, compared to that of VO_2 material and the temperature of transition (T_c) is lower.

2. The resistance change at the transition is moderate like in any other doped VO_2.

The SMT in VO_2 material has been widely studied; however its origin is still a subject of discussion. Studies have shown that free electron-electron correlation is the driving force behind the SMT[7, 8]. It is experimentally proved that critical electron density (n_c) of the order of 10^{18}/cm^3 is required for SMT to take place[25], which can be supplemented either thermally or electrically at a particular temperature. If the electron density falls below the critical limit by any external influence, the material returns back to the semiconducting state[4]. The mechanism of critical electron density state responsible for SMT in VO_2 can also be extended to doped VO_2 material. By doping with higher valence (> 4+) impurities such as Nb^{5+}, W^{6+} (n-type doping)

the free electron density is increased thereby giving scope for reaching the required electron density n_c and hence SMT at a lower temperature than that of the virgin VO_2 material[4, 7]. Tungsten doping is the most effective and reduces T_c by about 23 K/ atomic % [4]. The lower valence impurities (p-type dopants) like Al^{3+} and Cr^{3+} produce an opposite effect of increasing the transition temperature[5]. The present results of SMT in RTF are discussed in the light of these observations. From the results presented in Figure 4 and Table 3, RTF has a lower transition temperature. The XRD analysis indicates that in RTF samples a separate phase of MnV_2O_6 is present and Mn does not exist as either a substitutional or an interstitial impurity in VO_2. As a result, the Mn presence does not alter the electron density as it happens in the case of either $Nb^{(5+)}$, $W^{(6+)}$ or $Al^{(3+)}$, $Cr^{(3+)}$. So the observed shift of T_c to a lower value is not due to the presence of Mn in the reduced thin films. However, RTF consist of V_2O_5 in addition to VO_2 and MnV_2O_6. The presence of pentavalent vanadium cations along with VO_2 is similar to the effect of doping with higher valence impurities and is responsible for lowering the transition temperature by a margin of 6.5 K. It may be noted that the order of the resistance change is also lower compared to pure VO_2 material because of the presence of V_2O_5 and MnV_2O_6.

3.4 Optical Properties

The room temperature optical transmittance and reflectance characteristics of RTF are presented in Figure 4 and compared with those of ATF. The films after reduction are more absorbing and reflecting over the entire spectrum as observed by many other investigators[26,27] in the case of VO_2 films.
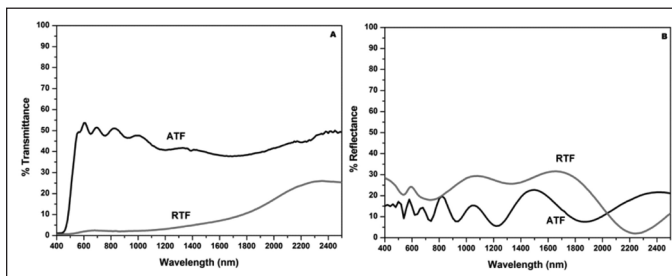
Figure 4: Optical transmittance (A) and reflectance (B) of the thin films before and after reduction.

3.4.1 Absorption Index

The absorption index variations with respect to wavelength from 400 to 2500 nm are presented in Figure 5 for RTF and ATF sample. The following differences have been observed for RTF:

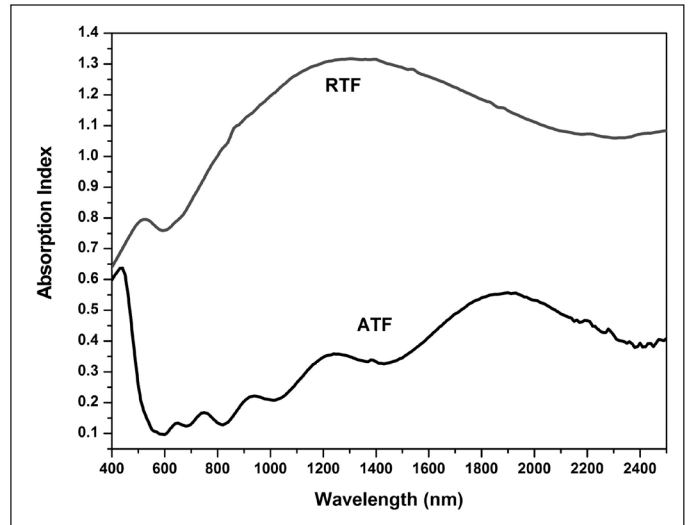1. The absorption index is substantially higher over the entire optical spectrum.

Figure 5: Absorption indices of ATF and RTF samples.

2. The absorption index increases with the increase of wavelength having peak values at 530 nm and 1270 nm unlike the ATF which has decreasing absorption with respect to wavelength initially, followed by increase of absorption after 560 nm with multiple peaks and valleys[10].

3.4.2 Effect of Temperature on Optical Transmittance

Vanadium dioxide material, which undergoes SMT, possesses interesting optical properties such as enhanced optical absorption and there is an hysteresis behaviour in optical transmittance with respect to forward and reverse cycle of temperature variation[4, 5, 26, 28]. These types of behaviour are also observed in doped VO_2 materials[4-6, 29]. It is natural to expect such characteristics in the present RTF also. Studies carried out over the temperature range from 298 to 368 K are shown in Figure 6A (optical transmittance as a function of wavelength from 400 to 2500 nm for different temperatures are plotted) and in Figure 6B (optical transmittance variation over the temperature range at selected wavelengths, namely 500, 1000, 1500, 2000 and 2500 nm). The transmittance decreases with increase of temperature. At 2500 nm the drop is 20 % a value smaller than that observed in pure VO_2 (about 60 % [4]). However, the present value is similar to that of W doped VO_2 [29].

The observed drop in transmittance (or increase of absorption) after transition is explained on the basis that change of crystalline phase from monoclinic to tetragonal results in overlap of the valence band due to V-3d^{II} with V-3dπ* conduction band [28, 30] and more free charge carriers are created as in the case of metals. However, the smaller transmittance change in RTF, compared to that of VO_2, is due to the fact that RTF
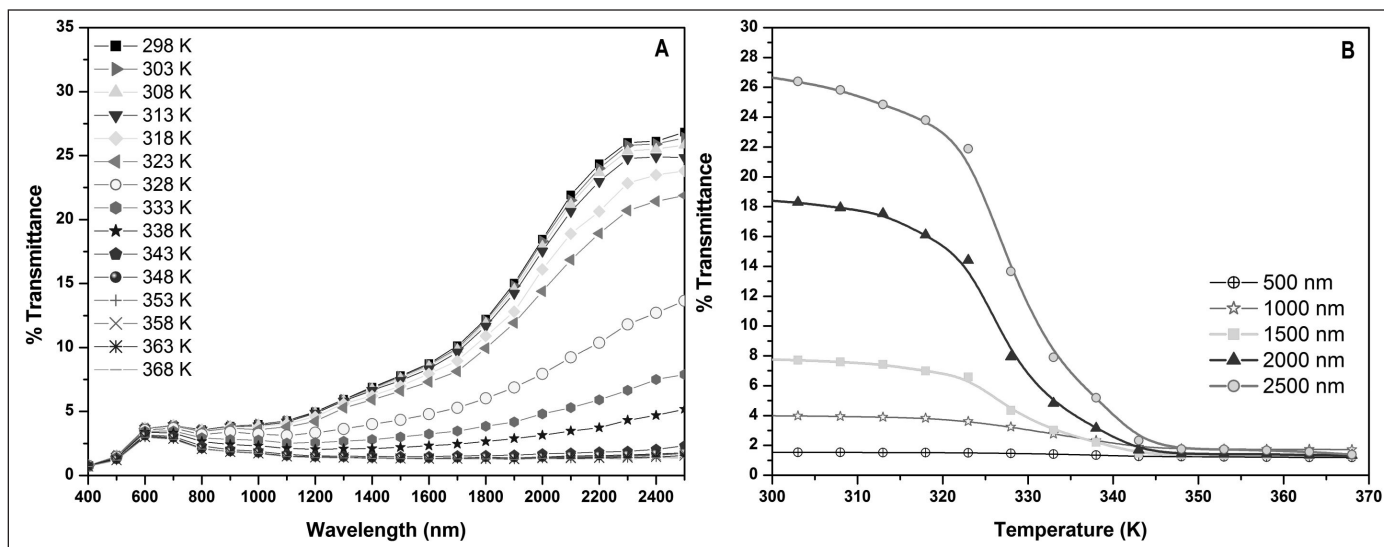
Figure 6: Optical transmittance of RTF sample (A) at different temperatures as a function of wavelength and (B) at selected wavelengths as a function of temperature.

contains not only VO_2 but also V_2O_5 and MnV_2O_6. It is reported in the literature that the presence of any other phase other than VO_2 [12] has an effect on transition characteristics such as a less sharp transition and smaller change in electrical and optical properties.

In Figure 7, the transmittance change with respect to forward and reverse cycles of temperature variation is presented showing an hysteresis behaviour. This is similar to the characteristics observed in the case of pure and doped VO_2. In a near ideal situation, namely single crystal VO_2, the transition is very steep with a negligible hysteresis width [4, 39]. But the transition is broader mainly due to the presence of other crystalline phases and defects present in RTF.
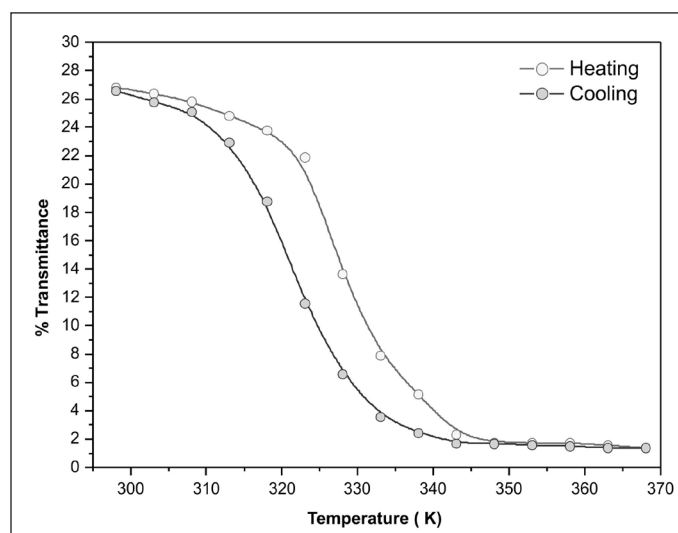

Figure 7: Optical transmittance hysteresis at 2500 nm.

4. Conclusions

The present investigation has established a simple method of preparation of crystalline V-Mn-O thin films by physical vapour deposition technique followed by annealing of thin films under a reduced atmosphere. The crystalline thin films consist of MnV_2O_6, V_2O_5 and VO_2, with VO_2 as the major phase. The electrical and optical properties of these thin films follow the typical behaviour of doped VO_2 material exhibiting however a lower transition temperature and broader range of transition. The reduced thin films have enhanced optical absorption in the near infrared region due to the creation of defect centers within the forbidden band gap region attributed to multi-valence state of vanadium.

Acknowledgements

References

1. J. Morin, Phys Rev. Lett. (1959), **3(1)**, 34-36
2. G. Anderson, Acta Chern. Scand. (1954), **8**, 1599-1606
3. S. Westman, Acta Chern. Scand. (1961), **15**, 217
4. S. Paradis, P. Laou, D. Alain, DRDC Valcartier, Technical Memorandum, DRDC Valcartier TM 2007-002, Canada (2007)
5. F. Beteille, J. Livage, Optical switching in VO_2 thin films, J. Sol-Gel Sci. Tech. (1998), **13**, 915-921
6. J. Ye, L. Zhou, F. Liu, J. Qi, W. Gong, Y. Lin, G. Ning, J. Alloys Comp. (2010), **504**, 503-507

7. P. P. Boriskov, A. L Pergament, A. A. Velinchko, G. B. Stefanovich, N. A. Kuldin, (2006) *http://arxiv.org/ftp/cond-mat/papers/0603/0603132.pdf*

8. A. Liebsch, H. Ishida, G. Bihlmayer, Phys. Rev. B (2005), **71**, 085109

9. G. M. Gouda, C. L. Nagendra, Sens. Actuators A (2009), **155**, 263-271

10. G. M. Gouda, C. L. Nagendra, Sens. Actuators A, (2013), **190**, 181-190

11. W. Q. Hong, J. Phys. D: Appl. Phys. (1989), **22**, 1384-1385

12. PDF No 44-0252, JCPDS-ICDD (1997)

13. PDF No 41-1426 and 45-1074, JCPDS-ICDD (1997)

14. PDF No 40-0165, JCPDS-ICDD (1997)

15. D. Q. Liu, W. W. Zheng, H. F. Cheng, H. T. Liu, Adv. Mater. Res. (2009), **79-82**, 747-750

16. G. Guzman, F. Beteille, R. Morineau, J. Livage, J. Mater. Chem. (1996), **6**, 505-506

17. C.V. Ramana, S. Utsunomiya, R. C. Ewing, U. Becker, Solid State Commun. (2006), **137**, 645-649

18. Y. Ningyi, L. Jinhua, L. Chenglu, Appl. Surf. Sci. (2002), **191**, 176-180

19. L. Murawski, J. Livage, J. P. Audiere, J. Non-Cryst. Solids (1990), **124**, 71-75

20. P. Umadevi, C. L. Nagendra, G. K M. Thutupalli, Sens. Actuators A (1993), **39**, 59-69

21. D. K. Chakrabatrhy, D. Guha, A. B. Biswas, J. Mater. Sci. (1976), **11**, 1347-1353

22. J. Duchene, M. Terraillon, M. Pailly, Thin Solid Films (1972), **12**, 231-234

23. J. Verkelis, Z. Bliznikas, K. Breivk, V. Dikinis, R. Sarmaitis, Sens. Actuators A, (1998), **68**, 338-343

24. C. N. R. Rao, M. Natarajan, G. V. Subbarao, R. E. Loehman, J. Phys. Chem. Solids (1971), **32**, 1147-1150

25. G. Stefanovich, A. Pergament, D. Stefanovich, J. Phys: Condens. Matter (2000), **12**, 8837-8845

26. S. Lu, L. Hou, U. Gan, J. Mater. Sci. (1993), **28**, 2169-2177

27. E. E. Chain, Appl. Opt. (1991), **30**, 2782-2787

28. V. Eyert, Ann. Phys. (Leipzig) (2002), **11**, 650-702

29. P. Jin, S. Nakao, S. Tanemura, Thin Solid Films (1998), **324**, 151-158

30. S. Shin, S. Suga, M. Taniguchi, M. Fujisawa, and H. Kanzaki, A. Fujimori and H. Daimon, Y. Ueda, K. Kosuge, and S. Kachi, Phys. Rev. B (1990), **41**, 4993–5009.

Girish M. Gouda did his M.Sc. in solid state physics from Karnatak University, Dharwad and subsequently joined Indian Space Research Organsiation Currently he is working as a senior scientist in Laboratory for Electro-Optics Systems (LEOS), ISRO, • Bangalore

Compositional Characterisation of Optical Coatings by Rutherford Backscattering Spectrometry

Sanjiv Kumar

National Centre for Compositional Characterisation of Materials,
Bhabha Atomic Research Centre, ECIL Post, Hyderabad-500062, India
sanjucccm@rediffmail.com, sanjukumar@barc.gov.in

Abstract

Rutherford backscattering spectrometry (RBS) is an important ion beam analysis technique for investigating surface and near surface regions of materials. The technique has found extensive applications, by virtue of its analytical capabilities that include non-destructive depth profiling, in the characterization of thin films. The article presents a brief description of the basic principles and salient features of RBS and summarises its applications in the analysis of optical coatings with particular emphasis on multilayered films.

1. Introduction

The advent of thin film technology has revolutionized the world of optical materials and their applications. Thin film optical coatings find extensive applications in energy, space, defence and other areas of high technological importance. These are also used in a diverse range of commercial consumer products that include cell phone, television, light emitting diode, binocular etc. The coatings function essentially by modifying the reflection and transmission characteristics of bulk materials onto which these are deposited and can serve, for instance, as anti-reflection, high reflection or anti-glare coatings, beam splitters, filters or transparent conductors. Such coatings are composed of metallic or dielectric (compound) materials or can be a combination of the two (metal-compound). In terms of configuration, these are single, bi or multilayered wherein the thickness of a layer can range from a few to several tens of nanometers. Amongst these, multilayered coatings are of immense significance as these synergistically combine the properties of different materials to realise functionality that is difficult to achieve by single or bilayered coatings. The coatings can be fabricated by different thin film deposition processes using modern equipments. However the synthesis of good quality films of desired functionality is non -trivial. The optical properties of the films and also their long term stability are strongly influenced by their structural and compositional features. In order to meet the envisioned properties, it is desirable that the films have adequate compositional properties. In other words the films should have their requisite stoichiometry, are devoid of contaminants and have envisaged thickness, minimal surface roughness, good chemical homogeneity and well defined interfaces. Therefore stringent control over deposition and post deposition processing parameters must be exercised to obtain films with such compositional features.

The influence of composition on the properties of films brings into focus the need of analytical characterization of the coatings. It is required not only for the optimization of deposition parameters to prepare films of designed properties but also, if warranted, for failure analysis. The analytical techniques, in view of very low overall thickness of films, must necessarily be surface sensitive. Furthermore, in order to analyze multilayered coatings the techniques should also be capable of providing composition as function of depth, preferably with high resolutions. The past few decades have witnessed the growth of several surface techniques with significantly different analytical capabilities. The prominent among these are X-ray photoelectron spectroscopy (XPS), Auger electron spectroscopy (AES), secondary ionization mass spectrometry (SIMS), glow discharge mass spectrometry (GDMS), Rutherford backscattering spectrometry (RBS) and nuclear reaction analysis (NRA). These techniques are based on different physical principles and have their own advantages and limitations. XPS, AES, RBS and NRA, as a matter of fact, are exclusively surface analysis techniques and have been used extensively for the characterization of thin films over the years. SIMS and GDMS, on the other hand, have dual applications: in addition to surface analysis these techniques are also used for bulk analysis and trace element determination with very good (ppm or lower) sensitivity. It is important to note that XPS and AES are inherently non-destructive, however, due to very low (<10 nm) probing depths, take recourse to sputtering for depth profile measurements. SIMS and GDMS, in contrast, are sputter based techniques and therefore are inherently destructive. Meanwhile RBS and NRA have the most distinguishing features since these do not involve any physical removal of matter for depth profile measurements. The two techniques, as described later, invoke the concept of stopping powers to discern the depth distribution of the

components. It lends the techniques a true non-destructive character and makes them unique and attractive methods for analytical characterization of thin films.

The present article presents an account of the applicability of the RBS in the analysis of thin optical coatings. Subsequent to a brief description of the principles underlying the technique and its salient features relevant examples are presented to critically analyse its efficacy in analysis of optical coatings with particular emphasis on multilayered films. The article also dwells on some of the recent developments regarding improvements in depth resolutions of the two techniques and culminates with a succinct comparison of the different surface techniques.

RBS and NRA are ion beam analysis (IBA) techniques. IBA techniques refer to techniques that utilize energetic beams of protons, α-particles or other ions such as Li^{+n}, C^{+n} etc. obtained from a particle accelerator as probes. The energy of ion beams can range from 300 keV to 10 MeV. The beams, on bombardment induce as shown in Fig. 1, different processes in the targets (herein films and the substrates) some of which carry unique and distinct analytical information on the targets. The classification or nomenclature of the IBA techniques is based on these processes. Before we proceed to a detailed description of RBS, it is pertinent to mention that particle induced X-ray emission (PIXE), particle induced γ-ray emission (PIGE) and elastic recoil detection (ERDA) are the other important IBA techniques. PIGE and PIXE are complementary techniques. PIGE is used for the sensitive (ppm) determination of light elements while PIXE, for trace analysis of mid and high Z elements. ERDA has applications in thin film characterization. It is also worth mentioning that IBA measurements, in general, are performed in high vacuum though there are instances wherein PIGE and PIXE have been performed in non-vacuum ambience as well.
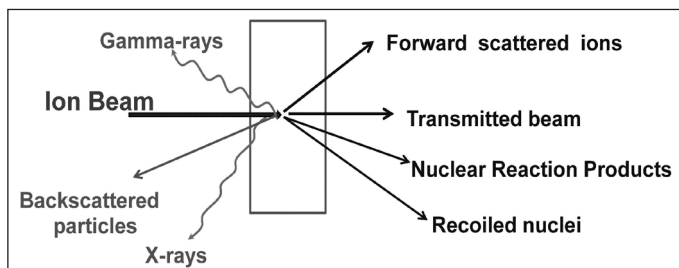

Fig.1 A schematic of interaction of an ion beam with matter (thin film).

2. Methodological considerations

2.1 A brief treatise on stopping power and stopping cross-section

The concept of stopping power is central to the basic understanding of ion beam techniques and their application to the analysis of materials. The term stopping power, in brief, refers to the rate of energy loss per unit distance of an energetic ion beam in a medium and is represented by dE/dX wherein E and X are energy and distance respectively. The unit of stopping power is eV/Å or keV/µm. The origin of stopping power lies in the interaction of the ion beam with the electrons and nuclei of atoms constituting the medium. The interaction with electrons is inelastic in nature and the corresponding stopping is known as electronic stopping. The interaction of the ion beam with nuclei, on the other hand, involves multitude of elastic collisions and the relevant stopping is referred to as nuclear stopping. The net stopping power is a sum of electronic stopping power and nuclear stopping power.

Some of the aspects of stopping power that are important from the point of view of IBA are summarised as: (1) The stopping power depends on the type and energy of the ion beam and also on the medium it traverses through. It, in general, increases with the atomic number of the projectile (ion beam) and also with that of the medium and its density. A typical energy dependence of the stopping power on the energy of ion beam is shown in Fig. 2 for illustration.
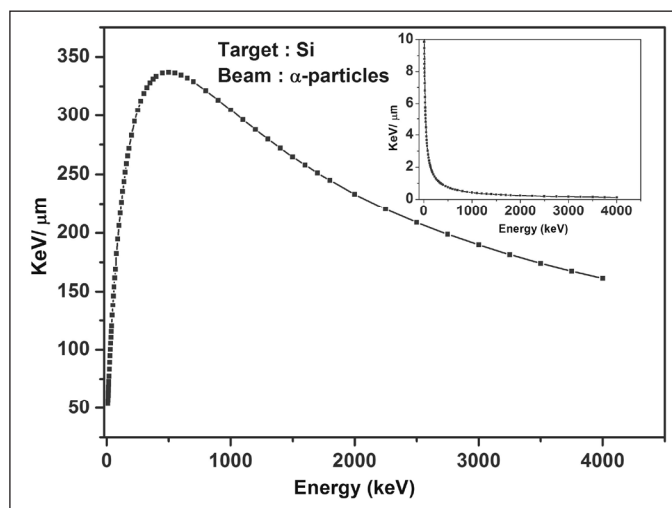
Fig.2 Electronic stopping power (keV/µm) of Si as a function of a-beam energy. The inset shows the nuclear stopping power ((keV/µm) component.

The figure also shows that the electronic stopping power predominates over the entire energy range. (2) The stopping powers can be experimentally determined. However, there are several theoretical models to calculate them. The model the formulated by Ziegler and Biersack (Z-B) and Ziegelr, Biersack and Littmark (Z-B-L) implemented in different versions of TRIM/SRIM codes is more often used. The theoretically derived values have typically <4 % uncertainty. (3) The stopping powers of

compounds can be calculated by the Bragg's rule of linear additivity and (4)The chemical bonding in the medium (compound) does not influence the stopping power.

Though the stopping power (dE/dx) has great theoretical value, stopping cross section (ε) is generally utilised in experimental studies and is defined as

$$\varepsilon \equiv \left(\frac{1}{N}\right)\frac{dE}{dX} \tag{1}$$

where N is the atom density of the target. The conventional unit of ε is eV/10^{15} atoms/cm^2. However it is also expressed in the units of keV/mg/cm^2 while N is represented accordingly. The advantage of using ε instead of dE/dX stems from the fact that the former is independent of the density of the material.

2.2 Principle and salient features of Rutherford backscattering spectrometry

As described pictorially in Fig.1 energetic ion beams interact with targets in multiple ways. In one of such interactions, first observed by Lord Ernest Rutherford, some of the incident ions are scattered in backward directions by positively charged nuclei of heavier nuclei. The scattering has great analytical value and is known, in the honour of the eminent discoverer, as Rutherford backscattering spectrometry (RBS)[1]. The technique involves energy analysis of the backscattered particles (ions). The scattering is Coulombic in nature and can be succinctly illustrated by Fig.3 (the symbols are quite common and are not explained for the sake of brevity)

A RBS measurement provides information on three basic features of thin films. Firstly, as a qualitative analysis it facilitates the identification of elements constituting the specimen, secondly it enables their quantification and thirdly it unravels their depth distribution. The identification of elements is, in fact, based on mass analysis which is governed by the kinematics of the scattering and is defined by kinematic factor K.
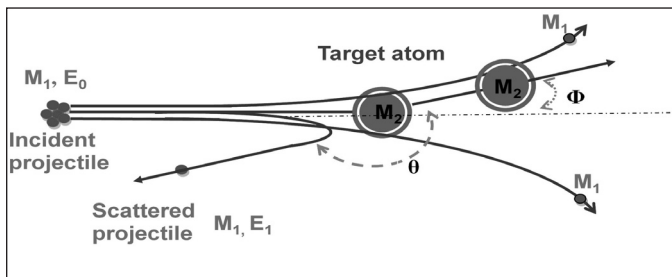

Fig.3 A schematic of Rutherford backscattering process.

$$K_{M_2} = \left\{ \frac{\left[1-\left(M_1/M_2\right)^2 \sin^2\theta\right]^{1/2} + \left(M_1/M_2\right)\cos\theta}{1+\left(M_1/M_2\right)} \right\}^2 \tag{2}$$

The mass resolution increases with increase in (a) beam energy (E_1), (b) scattering angle (θ), (c) mass of the projectile (M_1) and (d) energy resolution of the detector. It is higher for low target masses and lower for high target masses. For example, the mass resolution obtainable with 2.0 MeV α-particle at θ=180° is about 0.2 at M_2 = 10, about 5 at M_2= 100 and about 22 at M_2= 200 for a detector with 16 keV energy resolution.

So far as quantification is concerned, it is primarily influenced by backscattering cross section which, in brief, is defined by the relationship

$$\frac{d\sigma}{d\Omega} = \left(\frac{Z_1 Z_2 e^2}{4E}\right)^2 \frac{4}{\sin^4\theta} \frac{\left\{\left[1-\left(\left(M_1/M_2\right)\sin\theta\right)^2\right]^{1/2} + \cos\theta\right\}^2}{\left[1-\left(\left(M_1/M_2\right)\sin\theta\right)^2\right]^{1/2}} \tag{3}$$

A perusal of the equation shows that the scattering cross-section decreases with increase in scattering angle and increases with (a) decrease in incident beam and (b) increases in with both Z_1 and Z_2. An important point that needs to be mentioned that for certain low Z elements such as Li, B, C, O etc. though the kinematics of scatterings is governed by equation(2), the scattering cross sections are not Rutherford in nature (i.e. equation 3 is not obeyed) . This is due to the involvement of nuclear effects and therefore such scatterings are often referred to as nuclear scattering. It is particularly true for protons and alpha particles even in the energy region (0.5-4.0MeV) generally utilized for RBS measurements. In such cases the cross-sections at certain energies are higher than the corresponding Rutherford cross-sections and therefore these have proved to be very useful for the detection of low Z elements with improved sensitivity. But even more remarkable is the fact that excitation functions of some of such scatterings are endowed with resonances which have been exploited on numerous occasions for depth profile measurements. A list of some of such scatterings is presented in Table 1 for the benefit of the readers[2,3,4].

The depth profile measurements are obtained by invoking the concept of stopping power and thus are non-destructive in nature. Similar concept is used in the determination of thickness (x) of a film. It is obtained by the relationship

$$\Delta E = Sx \left(\frac{k}{Sin\alpha} + \frac{1}{Sin\beta} \right) = x[S] \tag{4}$$

Table 1: List of alpha - nuclear resonance scattering involving boron, carbon and oxygen

Element	Scattering	Resonance energy (MeV)	σ_R/σ
Boron	$^{11}B(\alpha,\alpha)^{11}B$	3.87	21.0
Carbon	$^{12}C(\alpha,\alpha)^{12}C$	4.26	128
Oxygen	$^{16}O(\alpha,\alpha)^{16}O$	3.05	22.66

σ_R/σ= Ratio of scattering cross-section at resonance to the Rutherford backscattering

wherein ΔE is the energy difference between the front and rear edges of a signal in the backscattered spectrum, [S] is the stopping cross-section factor, α is the incidence angle and β is the exit angle. It is worthwhile mentioning that the thickness x is in terms of areal density (at. /cm^2) and can be converted into linear dimensions by taking the density of the film into consideration. Alternatively, if the linear thickness of a film is known precisely, for example by ellipsometry or profilometer, the areal density provided by RBS can be used to determine the density of the film.

The experimental set up, the methodologies involved in quantification and depth profiling using backscattering spectrometry are described in detail in reference 1 and the references cited therein. There are several computer codes such as SIMNRA[5], RUMP etc. available for simulating the experimental backscattered spectra. Many of the spectra presented in the next section are superimposed with SIMNRA generated simulated profiles.

3. Characterization of optical coatings

The backscattered spectra of thin films of various kinds presented in a series of figures in this section provide a glimpse of the analytical capabilities of backscattering spectrometry. The spectra in Figs.4 and 5 correspond to elemental (Hf) and compound (SiO$_2$ and HfO$_2$) single layered films deposited on Si. The rationale behind selecting SiO$_2$ and HfO$_2$ is two-fold: firstly, these are important optical materials having refractive indices of about 1.46 and 2.0 respectively and secondly, these are composed of high and or low Z elements and are therefore analytically important from the point of view of RBS as well. The Hf films represented by spectra (a) and (b) in Fig.4 measure 247×10^{15} at./cm^2 and 987×10^{15} at./cm^2 respectively in (areal density) thickness. The thicknesses are determined by simulating the experimental spectra and are 56 nm and 987 nm respectively in terms of linear dimensions. So far as the hafnium oxide film is concerned, it consists of 520×10^{15} Hf at./cm^2 and 1016×10^{15} O at./cm^2

with its overall area density being 1.53×10^{18} at./cm^2. It is important to note the difference in the intensities of Hf and O signals in the 2.3 MeV α-RBS of the film (Fig.4(c)) which essentially is the manifestation of the Z^2 dependence of the Rutherford backscattering cross-section.
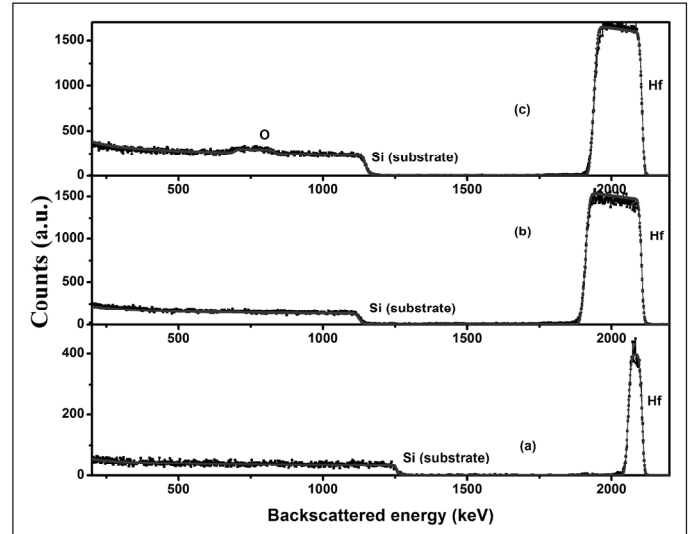

Fig. 4 2.0 MeV α-Rutherford backscattered spectra (a) and (b) of Hf metal films of different thicknesses and (c) of hafnium oxide film.

The 2.0 MeV α-RBS spectrum of the silicon oxide film in Fig.5 (a) has similar features except that the difference in intensities of Si and O is not very prominent. It is also apparent that the signal of Si of the film can be easily distinguished from that of substrate. The oxide films can also be analysed by 3.05 MeV $^{16}O(\alpha,\alpha)^{16}O$ resonant scattering and proton-backscattering spectrometry. As can

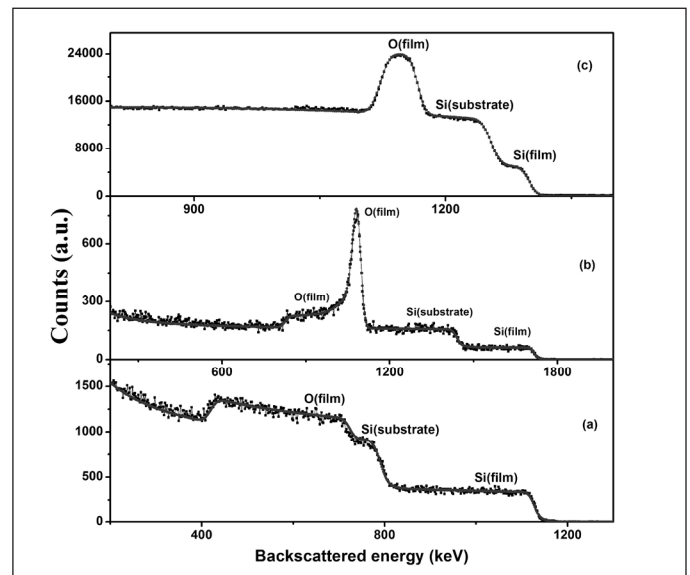*Fig. 5. (a) 2.0 MeV α- Rutherford backscattered spectrum (b) 3.05 MeV $^{16}O(\alpha,\alpha)^{16}O$ resonant scattering spectrum and (c) 1. 5 MeV proton backscattered spectrum of a silicon dioxide film on Si.*

be seen from the relevant spectra in Fig. 5(b) and (c), these two methods exhibit high sensitivity towards oxygen since herein the scattering cross-sections for O are higher than the corresponding Rutherford scattering cross-sections. In fact, 3.05 MeV $^{16}O(\alpha,\alpha)^{16}O$ resonant scattering is widely used for depth profiling O in films. The analytical results obtained on the film by the three methods are listed in Table 2. These are in good agreement which shows that backscattering spectrometry, in general, can be effectively used for a precise compositional analysis of oxide films.

Table 2: Areal densities of Si and O in a silicon dioxide film determined by backscattering spectrometry

Technique	Areal density of Si (10^{15} at/ cm²)	Areal density of O (10^{15} at/ cm²)	Total areal density (10^{15} at/ cm²)
2 MeV p - BS	1412	3048	4460
2 MeV α-RBS	1534	3077	4611
3.05 MeV α-BS	1516	3028	4544

So far as the sensitivity of BS techniques to O is concerned, it is ~ 10 at.% for 2.0 MeV α-RBS, ~ 0.5 at.% for 3.05 MeV $^{16}O(\alpha,\alpha)^{16}O$ resonant scattering and ~ 5 at.% for proton backscattering spectrometry in silicon. The sensitivities of the techniques decrease in cases where matrices with effective atomic number higher than that of Si (e.g. ZnS) are used as substrates. In addition to oxides, fluorides and sulphides are also important optical materials. α-backscattering spectrometry can not

only be used to analyse the fluoride or sulphide films but $^{16}O(\alpha,\alpha)^{16}O$ resonant scattering can also provide a quantitative estimation of any oxygen contaminant in such films. For instance, the technique revealed the presence of ~ 10 at.% oxygen in gallium sulphide films prepared by thermal evaporation[6]. Gallium sulphide has potential applications as window or buffer layer in thin film photovoltaics. The relevant spectrum overlapped with the simulated curve is shown in Fig. 6. It also abundantly displays the simultaneous multielement detection capability of backscattering spectrometry.

Equally notable is the observation that the signal of O of the film and that of glass (used as a substrate) are clearly distinguishable. It facilitates an unambiguous and interference free determination of oxygen in the film.

Carbon is yet another common contaminant in films. However due to low Z (6) α-RBS has poor sensitivity, even less than oxygen, to the element. As a result 4.26 MeV $^{12}C(\alpha,\alpha)^{12}C$ resonant scattering and $^{12}C(p,p)^{12}C$ scattering that have significantly higher sensitivities (~ 0.1at.% and <5 at.% respectively) for carbon, are methods of choice for its detection in films. This is very well illustrated by 2.0 MeV proton backscattered spectrum (Fig.7) of a thermally evaporated lanthanum fluoride film wherein the prevalence of carbon impurity in the specimen can be clearly observed[7]. The spectrum further shows that the impurity exists over the entire thickness of the film. Its occurrence was attributed to the sequential condensation of hydrocarbons prevailing in the deposition chamber along with of the sublimed vapours of LaF$_3$ produced as result of resistive heating of the fluoride compound.
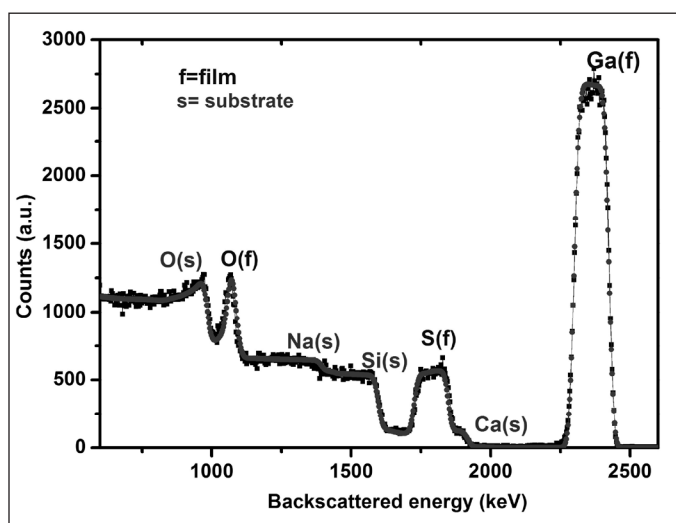

Fig. 6. 3.05 MeV $^{16}O(\alpha,\alpha)^{16}O$ resonant scattering spectrum of gallium sulphide film on soda lime glass.
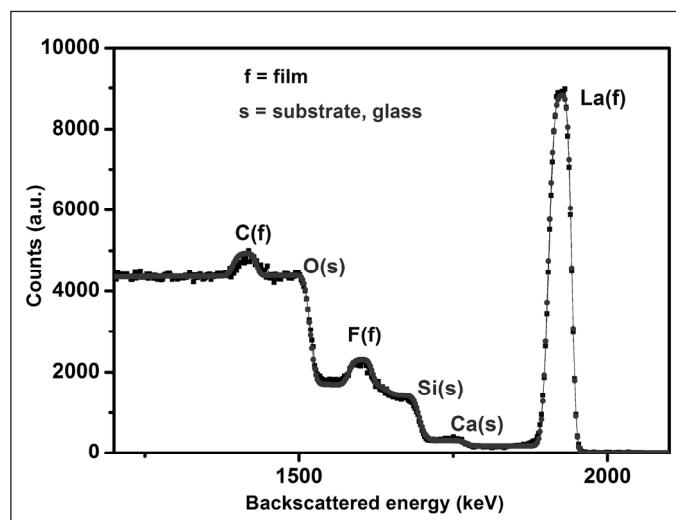

Fig. 7 2.0 MeV proton backscattered spectrum of a lanthanum fluoride film on glass.

Table 3: Atomic composition of 4-layered silica and hafnia films by 2.0 MeV alpha backscattering spectrometry

Layer No.	Layer structure	Layer composition	Thickness (x10^{15}at/cm^2)	Thickness (nm)
1	Si:O	0.36:0.64	499	62
2	Hf:O	0.31:0.69	534	59
3	Si:O	0.70:0.30	112	14
4	Hf:O	0.28:0.72	310	34
5	Substrate			

Backscattering spectrometry is eminently suitable for the analysis of multilayered films as well. It is exemplified in this section by a number of case studies that involve 4, 21 and 41 layered oxide films. To begin with, Fig.8 shows a 1.5 MeV α-RBS spectrum of a SiO$_2$/HfO$_2$/SiO$_2$/HfO$_2$/Si (four layered) film. The atomic ratio of the constituent elements in individual layers along with their thicknesses determined by simulating the spectrum is also provided in Table 3. A spectral 'anomaly' that draws immediate attention is that while the signals of Hf and Si of different layers are distinctly distinguishable but so are not the corresponding O signals. It is mainly due to the facts that (a) there is no non-oxide layer interspersed between the silica and hafnia layers and (b) the relative content of the element in the two compounds is same. This limitation of α-RBS can be overcome by depth profiling oxygen by means of 3.05 MeV ^{16}O(α,α)^{16}O resonant scattering. The spectra resulting from such an exercise are presented in Fig.9. The two peaks pertain to the signals of oxygen corresponding to silica (first) and hafnia (fourth) layers respectively. It is important to mention that depth profiling is a tedious process and is accomplished by recording
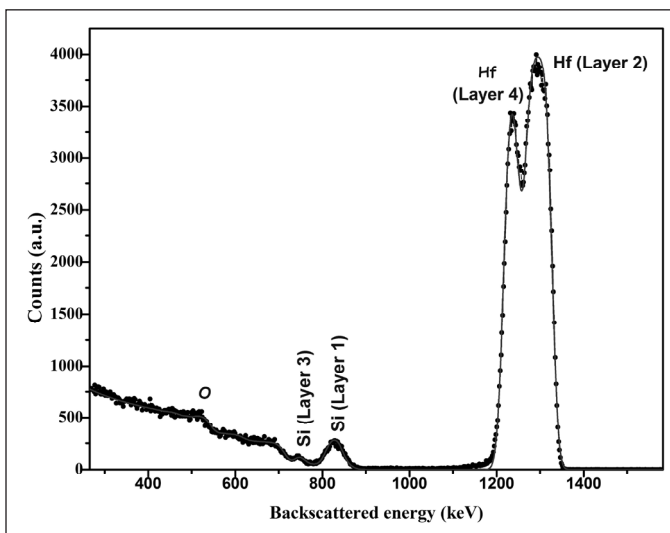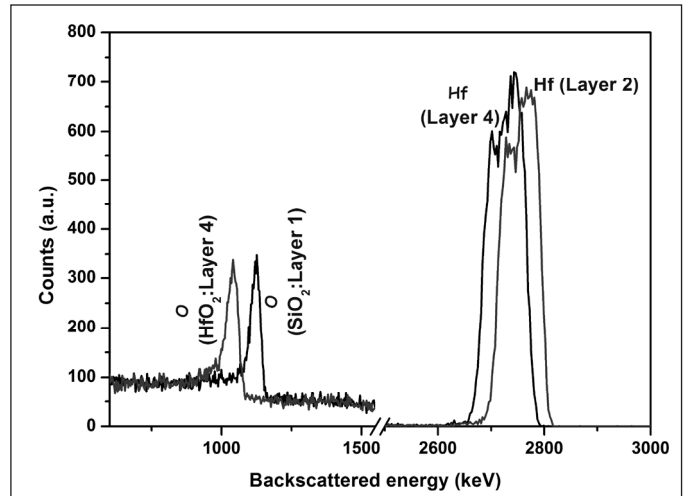

Fig. 9 3.05 MeV ^{16}O(α,α)^{16}O resonant scattering spectra of the (SiO$_2$/HfO$_2$)$_2$ film on glass.

spectra at multiple incident beam energies >3.035 MeV. The incident beam energy in this exercise is increased in suitable steps.

The ability of BS to analyse multilayered films non-destructively is more effectively demonstrated by the spectrum of a 21 layered film consisting of SiO$_2$ and TiO$_2$ layers (Fig.10)[8]. The coating is intended to serve as a Fabry-Perot Laser line transmission filter. A spectral analysis shows that the coating consists of alternate layers of SiO$_2$ and TiO$_2$ with the middle layer being that of TiO$_2$. The analysis also shows that the middle layer has thickness almost double that of other TiO$_2$ layers. Such an information is very valuable as the thickness of the middle layer defines the peak of the transmission wavelength. In fact the technique can be used for probing coatings comprising
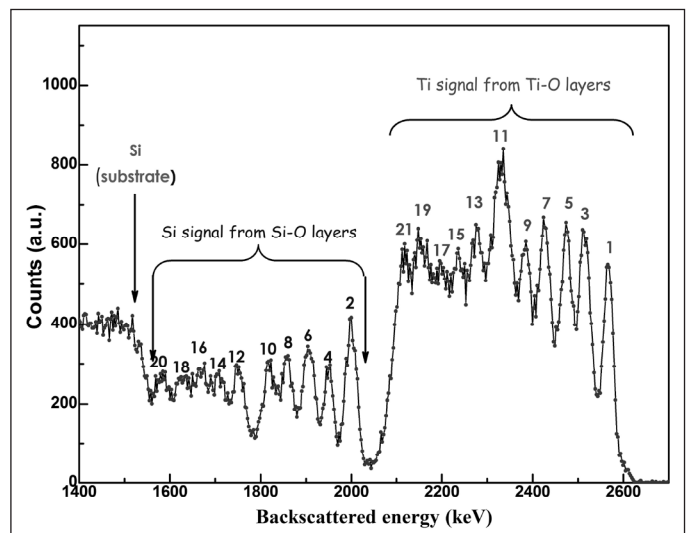

Fig.8 1.5 MeV α- Rutherford backscattered spectrum of a (SiO$_2$/HfO$_2$)$_2$ film on glass.

Fig.10 3.6 MeV α- backscattered spectrum of a 21 layered (TiO$_2$/SiO$_2$)$_{10}$/ TiO$_2$/ (SiO$_2$/TiO$_2$)$_{10}$ film on quartz.
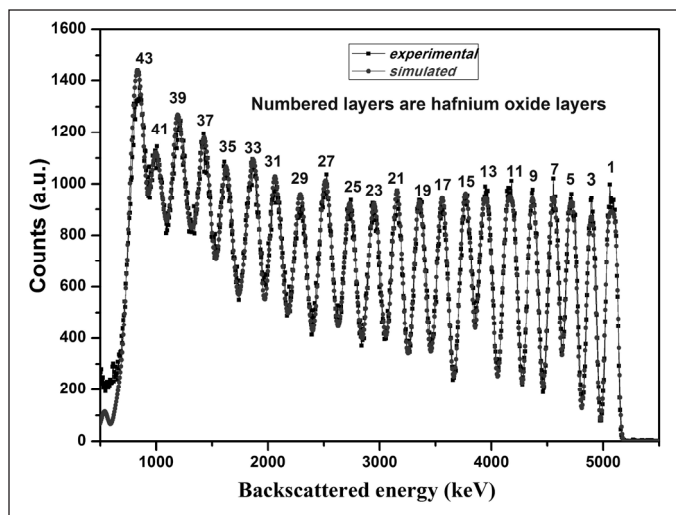
Fig. 11 6.0 MeV ^{12}C- Rutherford backscattering spectrum of a 43 layered $(HfO_2/SiO_2)_{21}/HfO_2/(SiO_2/HfO_2)_{21}$ film on quartz.

Fig.12.3.6 MeV a- backscattered spectrum of a multilayered antireflecting coating on ZnS.

even more number of layers. The spectrum of a 43-layered made up of HfO_2 and SiO_2 films in Fig. 11 is a case in point. Incidentally the film has been examined by 6.0 MeV Li $^{+2}$ beam and therefore signals of only Hf corresponding to 22 hafnia layers are seen while the troughs are indicative of Si signals from the 21 silica layers. Interestingly, there is a spectacular agreement between the experimental and simulated spectra which, in other words, establishes the veracity of the measurements.

Before concluding the discourse on multilayered films it is pertinent to discuss, at least in brief, anti-reflecting coatings which form a very important class of optical materials and employ multilayered films for specific applications. Such coatings provide excellent broadband, visible to far infrared wavelengths, antireflection behaviour against single layered coatings that operate in only a narrow wavelength region. Oxides and or fluorides are generally used for the fabrication of anti-reflecting coatings with LaF_3 discussed earlier being a typical example. The backscattered spectrum in Fig. 12 is that of a multilayered coating consisting of thin layers of HfF_4, TiO_2 and MgF_2 on ZnS. In such systems complexities can arise, particularly in the detection of F and Mg, due to relatively higher effective mass of the substrate. However the two elements can be detected and depth profiled as well, by nuclear reaction analysis. Presently a comprehensive study that involved RBS and NRA measurements for F [using $^{19}F(p,\alpha\gamma)^{16}O$ resonance reaction] was used to discern the layer configuration (in terms of relative position and thickness of individual layers) of the multilayered antireflecting coating represented by Fig.12. Interestingly the HfF_4 layer is the innermost layer.
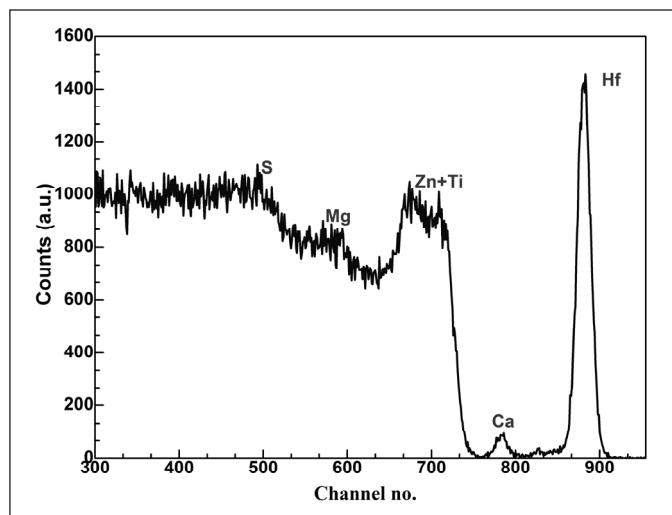
Sensitivity, probing depth and depth resolution are the three most important analytical features of a surface technique. Since RBS is carried out usually by α-particles, these features of α-RBS are described more prominently. The sensitivity of the technique to heavy elements is 10^{-1} to 10^{-2} at. % while to light elements it ranges from 5-15 at. %. The sensitivity to the light elements namely B, C and O is improved at least by an order of magnitude for resonant scatterings of the respective elements listed in Table 1. The probing depth of α-RBS is typically 2 to 3 microns though it depends on the nature of the matrix and energy of the incident beam. So far as the depth resolution is concerned, it is about 30 nm for low Z matrices and about 15 nm for mid and high Z matrices in their surface regions. It decreases dramatically with increasing depths due to straggling effects.

Backscattering spectrometry experiments are also conducted using protons and heavy ions. Proton backscattering spectrometry is often employed to analyse Li, B, C, N and O bearing films. Some of the examples presented earlier are testimonies of such capabilities. By virtue of its low stopping power, the probing depth of the technique can be as high as 15 μm. But for the same reason it has poor (100-500 nm) depth resolution and is therefore not suitable for the analysis of multilayered films.

Heavy ion RBS, on the other hand, is essentially useful in the analysis of films with mid or high Z constituents with adjacent mass numbers. It has better detection sensitivity, particularly in the top surface regions. It has been employed to detect as low as 5×10^{11} Au at./cm^2 on silicon[1]. However for reasons explained later, its depth resolution is not very high (as is the general perception) which in

fact, is nearly similar to that of α-RBS. Furthermore heavy ion RBS must be carried out with 6-10 MeV beam energy to probe to a depth of few microns.

The depth resolution of backscattering spectrometry, in general, is influenced by the detector (energy) resolution and stopping cross-section factor. Higher depth resolutions are achieved with detectors of higher (numerically lower) energy resolution and higher stopping powers. The energy resolution of Si surface barrier detectors employed for BS measurements is often about 15 keV for α-particles and protons which defines the depth resolution in different matrices. The detector resolution of heavy ions is 60-100 keV and therefore there is no substantial improvement in depth resolution in spite of significantly higher stopping powers.

The depth resolution can be increased by increasing the incident (α) and or exit (β) angles (increasing path length). It has been shown by way of analyzing (Si 30nm / Si0.78Ge0.22 5nm)$_5$ coatings that the depth resolution increases from about 40 nm at normal incidence to sub-10 nm grazing incidence angle[9]. However surface roughness can severely interfere in such measurements. Utilisation of low energy beams can also serve the purpose though other analytical aspects such mass resolution etc. also need to be taken into consideration. However, the best way to improve depth resolutions is to employ detectors of 1-2 keV energy resolutions. This is achieved by employing magnetic or electrostatic energy analysers instead of Si surface barrier detectors for energy analysis. It facilitates measurements with nano-metric depth resolution while the technique itself is classified as high resolution-RBS (HR-RBS). Unfortunately this technique has not found extensive applications in the analysis of optical coatings. However it holds much promise once the kind of limitations encountered in the analysis of Nb/C and W/C multilayered X-ray mirrors are addressed[10].

Besides composition and thickness, interfacial characteristics and roughness, a morphological feature, too can influence the properties of optical coatings. [Roughness of films is usually measured by atomic force microscopy (AFM)]. RBS can be used to discern the occurrence of interfacial mixing as well as the prevalence of surface roughness in films. However minor interfacial mixing and moderate roughness produce similar effects in RBS spectra: the rear edges are marked by lower slopes[11,12]. Therefore an unambiguous assertion of the precise reason giving rise to such an effect may sometimes be difficult. It can be rather more clearly understood by way of Figs. 13 and 14 which represent the spectra of two very important optoelectronic materials namely In_2O_3 and Ga_2O_3 respectively. A careful

analysis shows that the rear edge of the spectrum in Fig.13 is due to the roughness of In_2O_3 film while that in Fig.14 reflects the diffusion of Ga in soda lime glass during thermal annealing[13]. The determination of roughness of films by RBS has been a subject of several investigations and has been found to be in good agreement with that obtained by AFM measurements.

The capability to discern surface roughness is one of the most important and unique merits of RBS. Techniques like XPS and SIMS are not endowed with such capability. However RBS, unlike XPS, is not sensitive to chemical environment. Though hydrogen cannot be determined by RBS, it can be depth profiled by NRA and elastic recoil detection analysis. Hydrogen can also be analysed by SIMS which, among the surface techniques has the least detection limits for a vast majority of elements.
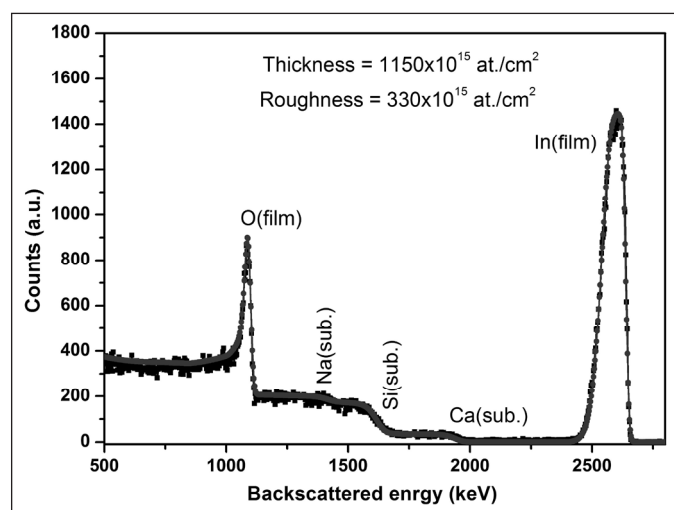

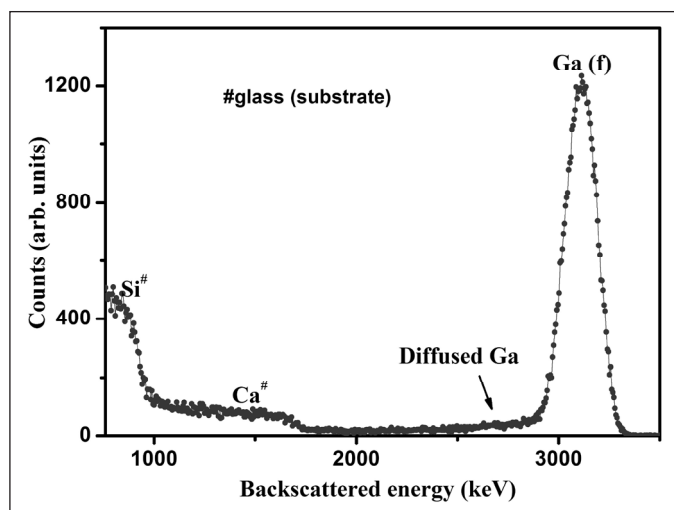*Fig. 13 3.05 MeV $^{16}O(a,a)^{16}O$ resonant scattering spectrum of an indium oxide film on glass.*

Fig. 14. 6.4 MeV ^{12}C- Rutherford backscattering spectrum of gallium oxide film on soda lime glass.

However this technique is ideally not very well suited for optical coatings since most of them have an insulating such as quartz etc. as substrates. Though such substrates can also cause difficulties in analysis by RBS, these can be circumvented or alleviated by adopting certain measures. SIMS has, in general, nano-metric depth resolution but the sputter rate has to be calibrated to obtain thickness in linear dimensions which often is prone to errors. Moreover sputtering, employed for the physical removal of matter can cause modification/ interfacial mixing that can disturb the inherent composition of the materials. RBS is non-destructive and the probability of the occurrence of such phenomena is very low which makes RBS an eminently suitable technique for the analysis of thin films and coatings.

Summary

The article describes the principles and salient features of RBS and presents a comprehensive illustration of its capabilities in the characterization of optical coatings. Several case studies have been presented to highlight its efficacy. The use of other IBA techniques such as NRA, ERDA can further widen the scope of analysis.

Acknowledgements

References

1. W. K. Chu, J.W. Mayer and M.A. Nicolet, Backscattering Spectrometry, Academic Press Inc, London, 1978.
2. J.R. Liu -, Z.S. Zheng, W.K. Chu, *Nucl. Instr. Meth. B* 108 (1996) 1-6.
3. J. A. Leavitt, Jr. L. C. McIntyre, P. Stoss, J.G. Oder, M. D. Ashbaugh, B. Dezfouly- Arjomandy, Z.-M. Yang and Z. Lin, *Nucl. Instr. Meth. B* 40/41 (1989) 776-779.
4. J. A. Leavitt, Jr. L. C. McIntyre, M. D. Ashbaugh, J. G. Oder, Z. Lin, B. Dezfouly
   Arjomandy, *Nucl. Instr. Meth. B* 44 (1990) 260-265.
5. M. Mayer, SIMNRA user's guide, Report IPP 9/113, Max Planck Institute for Plasmaphysik, Garching, Germany, 1997.
6. Pritty Rao, Sanjiv Kumar, N.K. Sahoo, *Materials Chemistry and Physics*, 149–150 (2015) 164-171.
7. Pritty Rao, Sanjiv Kumar, N.K. Sahoo, R.B. Tokas   *Nucl. Instr. and Meth. B*, 342 (2015)108-115.
8. N.K. Sahoo, Sanjiv Kumar, R.B. Tokas, S. Jena, S. Thakur and G.L. N. Reddy *Applied Optics*, 52 (2013) 2102-2115.
9. N.P.Barradas, A.P.Knights, C.Jeynes, O.A.Mironov, T.J.Grasby, E.H.C.Parker, *Phys.Rev.B* 59(7) (1999) 5097-5105.
10. J.R. Huddle, *Nucl. Instr. Meth. B* 40/41 (1989)773-775.
11. N. P. Barradas, E. Alves, S. Pereira, V. V. Shvartsman, A. L. Kholkin.E. Pereira, K. P. O'Donnell,C. Liu, C. J. Deatcher, I.M. Watson and M, Mayer, *Nucl. Instr. Meth. B* 217(2004) 479-497.
12. M. Mayer, R. Fischer, S. Lindig, U. von Toussaint, R. W. Stark, and V. Dose, *Nucl. Instr. Meth. B* 228 (2005) 349-359.
13. Pritty Rao and Sanjiv Kumar *Superlattice and Microstructures,* 70 (2014) 117-130.

Dr. Sanjiv Kumar graduated from 30 th batch (chemistry) of B.A.R.C. Training School. He completed his M.Sc. from Patna University and Ph.D. in Materials Science from I.I.Sc. Bangalore. Dr. Sanjiv Kumar specializes in surface analysis of materials by ion beam analysis (IBA) and X-ray photoelectron spectroscopy (XPS). Development of materials for semiconductor technology and renewable energy is his key research area. He is a recipient of DAE Science and Technical Excellence Award for 2008. He currently heads the Surface and Profile Measurement Section at National Centre of Compositional Characterization of Materials, BARC, Hyderabad.

An overview of recent advancements in organic light emitting diodes

S. P. Koiry* and D. K. Aswal

Technical Physics Division, Bhabha Atomic Research Centre, Mumbai, India
E-mail: spkoiry@barc.gov.in

Abstract

Organic light emitting diodes **(**OLEDs) - thin organic film sandwiched between two electrodes that emit light under an applied electric field - are emerging as the next generation light sources and displays. OLEDs were discovered in 1987 by Tang and van Slyke and since then they have covered a long journey to find their applications as displays for electronic devices (viz. mobile phones, stereo, and other portable devices). OLEDs offer number of advantages over existing technologies in terms of lightweight, mechanical flexibility, low power, high brightness and unmatched viewing angles. The efficiency of OLEDs over the period of time has improved significantly through improvisation of materials and device structures, which has facilitated the charge transport and their recombination resulting in ~100% internal quantum efficiency. In this article, we discuss working principle of OLEDs and present an overview of the recent materials used in OLEDs.

Introduction

At present we are witnessing new type of thin, large, flexible, bendable, app controlled aesthetic display and lighting devices, which were beyond imagination a few years ago. These changes are brought by organic light emitting diode (OLED) made of organic semiconductor film that emits light under electric field[1-3]. Such unbelievable applications of OLEDs are because of their capability to be fabricated on large areas using low cost solution based process like role-to-role printing on plastic substrates making devices lightweight, and mechanically flexible[2]. Moreover, organic materials can easily be modified chemically as per requirement that is not possible using the conventional inorganic materials. Therefore, there are wide ranges of choice for organic light emitting materials. The biggest advantage over existing display technology such as liquid crystal display (LCD) and LED is that the emitted light is diffusive that makes wide viewing angle. All these properties make OLED futuristic technology that is poised to change our lives as never before.

Although, OLED is a new technology, but research and development (R&D) has been started in the 1960s since the discovery of the electroluminescence in organic molecules — emission of light under electric field[5]. In 1987, the major breakthrough in R&D occurred when Tang and van Slyke demonstrated first OLED since then; OLEDs have been used as displays for electronic devices[2]. The OLED-based display has numerous advantages over the existing display technologies for example, in addition to lightweight, flexible and ease of fabrication, the OLED display has wider viewing angle (180°) than that of LCD (140°), and the conversion efficiency of OLED is eight times high as compare to the efficiency of LCD. Currently,

the OLED displays are competing with or replacing the existing displays such as the inorganic based LED, LCDs, cathode ray tube (CRTs), plasma displays etc. Recently, the OLED technology is also fast emerging as energy efficient next-generation lighting. The OLED-based solid-state lighting (SSL) has edge over the existing incandescent and fluorescent lightings in terms of high power efficiency, color quality, and lifetime at lower cost and less environmental impact[6]. Renowned lighting companies such as Philips, Osram, General Electric (GE), and Panasonic, as well as technology providers such as Universal Display, Cambridge Display Technology, Kodak, and Novaled mainly carry out the development of lighting technology[6]. Thus, the introduction of OLEDs light sources for general lighting applications will soon change the way of lighting of our street, office and households.

Working principle of OLED

An OLED basically consists of light emitting organic layer sandwiched between two metal electrodes with dissimilar work functions. The one electrode, cathode, supplies electrons and the other electrode, anode, supplies holes when electric field is applied between them. The electrons are injected from cathode to the lowest unoccupied molecular orbital (LUMO), and holes are injected to the highest occupied molecular orbital (HOMO) of the organic layer. Both the charges move towards each other under applied electric field and subsequently form excitons[7]. The recombination of these exactions release light that have a frequency equal to the energy gap ($E = h\nu$) between the LUMO and HOMO levels of the light emitting layer as shown in Fig. 1.The charge injection to organic layer follows Fowler-Nordheim tunneling (J_{FN}) or

Richardson-Schottky (J_{RS}) thermionic emission, described by the equations (1) and (2), respectively[7].

$$J_{FN} = \frac{A\, q^2 F^2}{\emptyset_B \alpha^2 k_B^2} e^{\left(-\frac{2\alpha\emptyset_B^{\frac{3}{2}}}{3qF}\right)} \tag{1}$$

$$J_{RS} = AT^2 e^{\left(-\frac{\emptyset_B - \beta_{RS}\sqrt{F}}{k_B T}\right)} \tag{2}$$

Where A is Richardson constant, F is applied electric field, $\emptyset_B$ is zero field injection barrier, k_B is Boltzmann's constant, T is temperature in K , $\alpha = 4\pi\frac{4\pi\sqrt{2m}}{h}$ (m= electron mass and h= Planck's constant), $\beta_{RS} = \sqrt{q^3}/4\pi\varepsilon\varepsilon_0$ (ε = relative dielectric constant, ε_0 = vacuum permittivity).
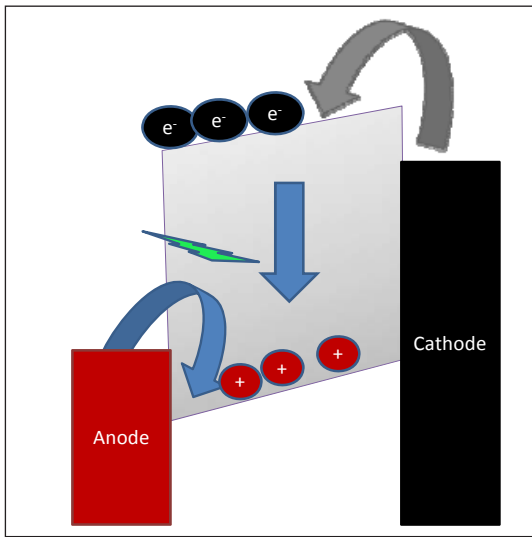

Fig. 1. Schematic of electron and hole injection and light emission. ⊕ and Ⓒ represent electron and hole. Arrows indicate the charge injection from anode and cathode. The layer between anode and cathode is emissive layer and its HOMO and LUMO are marked in the figure.

As organic based materials are mostly disordered system, therefore the charge carriers move diffusively under electric field gradient. The charge carrier mobility in organic material is very low, and they follow either space charge limited or trap charge limited conduction mechanism(s). The hole and electron recombination in organic materials is described by Langevin theory, which is based on a diffusive motion of positive and negative carriers in the attractive mutual Coulomb field[7]. Thus the recombination constant (R) is proportional to the carrier mobility as

$$R = [q/\varepsilon\varepsilon_0][\mu_h + \mu_e] \tag{3}$$

Where μ is mobility, h is hole and e is electron

The efficiency of OLED is defined in many ways, such as, the current efficiency in cA^{-1}, the luminous efficiency in

lmW^{-1} and quantum efficiency. The quantum efficiency is divided in two types—external efficiency (η_{ext}) and internal efficiency (η_{int}) [8]. η_{ext} is defined as the number of emitted photons divided by the number of injected charges, which is given by

$$\eta_{ext} = \eta_x \varphi_f \eta_{out} = \eta_{int}\eta_{out} \tag{4}$$

Where η_r is exactions, creating probability that is nearly equal to 1 because of the low mobility of the charge carriers in organic materials. φ_f is the fluorescent quantum efficiency or the fraction of excitons that decays radiatively. χ is the probability for radiative decay to occur, and generally, only singlet excitons emit light. η_{out} is the fraction of photons that can escape the device and is limited by wave guiding in the device layers and the substrate.

Device structure and materials

The efficiency of OLED depends on various factors such as the properties of light emitting layer, the injection of charge carriers in organic layers and their transport, the creation of excitions, recombination, light production and transmission of light[9]. Thus to increase the efficiency, OLED structure has evolved from single layer based devices to multilayer structures as shown in Fig. 2 [8].The importance and properties of each of these layers are discussed below.

1. **Substrate:** To fabricate whole architecture of an OLED requires a planar substrate—rigid or flexible. The substrate should be flat, pinhole free, transparent (>90%) in order for light to escape and high refractive index (1.8 to 2)[9]. Glass substrates are widely used such

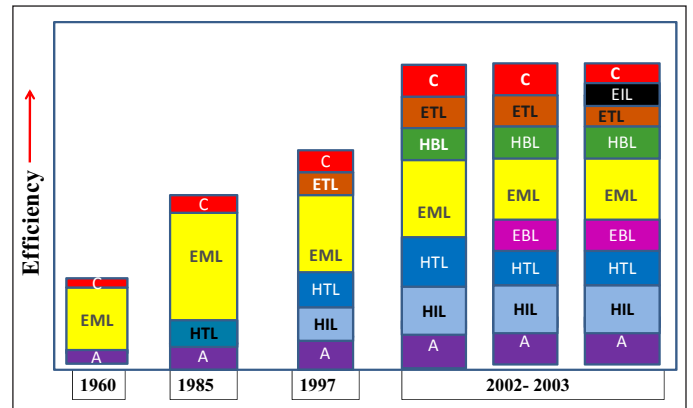*Fig. 2. Evolution of OLED device structure with time. Colors represent different layers that added with time,* ■ *= Anode (A),* ■ *= Hole Injection Layer (HIL),* ■ *= Hole Transporting Layer (HTL),* ■ *= Electron Blocking Layer (EBL),* ■ *= Emitting Layer (EML),* ■ *= Hole Blocking Layer (HBL),* ■ *= Electron Transporting Layer (ETL),* ■ *= Electron Injection Layer (EIL), and* ■ *= Cathode (C).*

as borosilicate glass (n~1.51), soda-lime (*n* ~ 1.46), Schott glass (*n* ~ 1.8)[9]. Since glass based substrate are rigid, flexible substrates are need for flexible OLEDs devices for displays and lighting. The examples of such substrates are metal foils (stainless steel, Al) flexible glass (50 μm borosilicate), polymer (polyamide, polyester, polycarbonate based) and exotic materials such as paper[9]. The advantage of using flexible substrates over rigid substrates is the possibility of the roll-to-roll processing of OLED, making devices large scale and lightweight.

2. **Anode:** Anodes are transparent materials which could inject hole into the hole injection layer (HIL) and allow to transmit generated light in the devices to outside. The most commonly used materials for anode are metal oxide semiconductors doped with heteroatoms which are transparent in visible region and highly conducting such as doped ZnO, In_2O_3 and SnO_2, In_2O_3:Sn (ITO), SnO_2:F (FTO) and ZnO:Al (AZO)[9]. Among all transparent conducting electrodes, ITO is widely used as transparent electrode. However, indium is costly and a scant metal; therefore indium free transparent conducting electrode is the present major challenge. The emergent alternatives are conducting polymer (PEDOT: PSS), graphene, carbon nanotube[9].

aligning the charge-transport levels (LUMO/HOMO) of organic semiconductors and electrodes. The layer on the anode is called hole injection layer (HIL) and corresponding layer on the cathode is electron injection layer (EIL)[9].

The effect of buffer layer for example HIL can be can explained as since the barrier between electrode and hole transporting layer is large, holes are injected directly from into the HOMO of the hole-injection organic buffer material, and then holes hop from the buffer material to the hole-transporting material. Similarly, electrons are injected to high-lying LUMO of EIL and subsequently electrons transport further. Typical HIL and EIL that are in used are presented in the Table -1.

4. **Hole transporting layer**: One of the most important factor on which high efficiency OLED depends, is the conduction of the inject carrier from electrode to emissive layer. One more factor that increases the efficiency is the confinement of the injected charges in emissive layer to improve the chance of exciton formation and recombination. Thus, hole-transporting layer (HTL) is used to transport holes and block electrons from reaching to opposite electrode without

Table -1: The list of most used HIL and EIL materials[9].

Type of layer	Inorganic based material	Organic based material
HIL	MoO_3, WO_3, NiO, CuO, RuO_2 V_2O_5, Fe_3O_4, Ag_2O and ZnO. These oxides tend to have high work functions, and thus increase the work function of the anode	copper phthalocyanine (CuPc), triphenyldiamine, (TPD), naphthyl-phenyl-amino-biphenyl (α-NPD), tricarbizoletriamine (TCTA), a family of triphenyl-amines, such as *m*-MTDATA , poly(3,4-ethylene-dioxythiophene): poly(4-styrenesulfonate) (PEDOT:PSS), polymer blends include polyaniline:camphorsulfonic acid (PANI:CSA)
EIL	Several alkali-metal halide (LiF, CsF NaF, MgF_2, and CaF_2), Cesium carbonate (Cs_2CO_3), TiO_2, ZnO, and ZrO_2	Alq_3; $Bebq_2$; PBD; OXD; TAZ; BCP, various oxadiazole-, triazole-, pyridine-, triazine-, and quinoline-based molecules, poly[9,9-bis(6'-(diethanolamino) hexyl)fluorine] (PFN-OH)

3. **Hole and electron injection layer**: The efficiency of OLED depends on the efficient charge carriers (hole and electrons) injection from electrodes (cathode and anode) to organic layer. Therefore, the energy barrier between electrode and organic layer plays important role. However, the energy barrier tends to be large which make charge injection difficult resulting high operating voltage and low efficient OLED. To mitigate the problem of energy barrier, a buffer layer (1 to 10 nm) has been introduced between electrode and organic layer, which reduce charge-injection energy barriers by

recombining with holes. Thus, HTL should have good hole conducting capability, which could be achieved by a HOMO level matching that of the emissive layer material and the work function of the anode. Furthermore, HTL should have a shallow LUMO level that prevents electrons entering into HTL from emissive layer. Since widely used anodes such as ITO and other such materials have work function between 4 and 5 eV, the HOMO level of HTL should match with the work function values. Typical examples of such compounds are 1,1'-bis[(di-4-

tolylamino)phenyl]cyclohexane (TAPC), TPD,NPD, *m*-MTDATA etc[9].

5. **Electron transporting layer (ETL)**: The purpose of ETL is same as HTL as discussed above. The only difference is, in place of hole, ETL transports electrons, blocks hole from reaching cathode, and sufficient triplet energy for exciton blocking. The LUMO level of ETL materials should be such that it can accept electron from low work function cathode (will be discuss shortly). However, organic materials have low electron mobility, and the chemical stability of such ETL material is low because of low-lying LUMO. Typical examples of ETL are shown in Fig. 3.
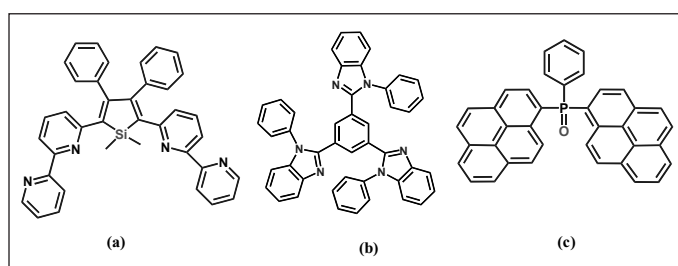

Fig. 3. Some typical examples of ETL (a) 2, 5-bis(6'-(2',2"-bipyridyl))-1, l-dimethyl-3,4-diphenylsilole, (b) 2,2',2"-(1,3, 5-benzinetriyl)-tris(1-phenyl-1-H-benzimidazole) and (c) phenyldipyrenylphosphine oxide[9].

6. **The emission layer (EML):** The most important part of OLED is light emitting layer in which excition creation and light emission take place. Moreover, the colour of the light depends on the energy gap of HOMO and LUMO of EML. When the charge carriers combine in EL, they give rise either singlet or triplet states depending on the parallel or antiparallel spins of the highest- energy electrons. From quantum mechanics, statistically three triplet states could form against each singlet state. Thus the quantum yield of a spin allowed transition ($\Delta S = 0$) from excited state to ground state (fluorescence) will be limited to $\Phi F = 0.25$. This is the reason why first OLED based on fluorescence molecule/polymer had low efficiency. Therefore, to increase efficiency, it is necessary to collect the light from triplet (T1) to singlet (S0) transition termed as phosphorescence. But $T 1 \rightarrow S 0$ transition is spin-forbidden, owing to the same $\Delta S = 0$ selection rule mentioned above because of which quantum yield of phosphorescence is too low[4,8,9]. When the emissive layer of an OLED is doped with phosphorescent compounds, emission from triplet states can be induced which help emit light from all excitons—singlets and triplets. Thus, the internal quantum efficiency of the OLED can be increased up to 100%. For examples, when platinum (II) octaethylporphyrin, a metallophosphorescent,

was doped into EL emissive material Alq_3 {tris (8-hydroxyquinolinato) aluminium}, 90% of the energy from the Alq_3 host was transferred to the complex which increases the efficiency of the OLED[10]. Typical examples of emissive materials are quinacridone doped Alq_3, DPVBi (4, 4_-bis(2,2_-diphenylvinyl)-1,1_-biphenyl) doped DSA (distryrylarylene)[9].

7. **Cathode**: Cathode is chosen such that it can inject electron to LUMO of emissive layer. Since LUMO of emissive layer is low lying, the cathode is typically a low work function metal or its alloy ($\varphi_w \approx 2.9$–4.0 eV,). It must be stable to the organic layers under it. Examples are Mg:Ag; Li:Al; Ca; thin insulator; LiF; $MgOx$[9]. If cathodic layer like thin aluminium or Mg: Ag is transparent then OLED can be emissive from both top and bottom[9].

The purpose of each layer discussed above is depicted in Fig. 4 for visualization.
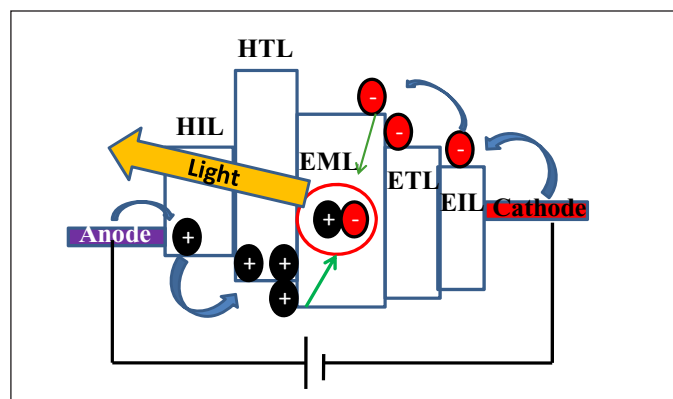
Fig. 4. Pictorial presentation of charge injection to and transportation through different layers of OLED under an electric field.

Method of layer depositions in OLEDs

All the layers starting from the anode, these typically include the HIL, HTL, EML, and ETL can potentially be deposited out of solution such as inkjet printing, doctor blading, spin-casting etc[8, 9]. The solution proccessibility of OLED makes possible to fabricate large scale at low processability cost. Other approach that has been used is vapour deposition technique. Both solution and vapour deposition techniques are used one over the other depending on technical needs, cost models, and materials compatibility.

Application of OLED

An OLED has wide viewing angle, large range of colour, rapid response time, low operating voltage, flexibility, light weight and most importantly all these at low fabrication cost and low power. Thus OLED has emerged as new display and lighting technology.

(a) Display technology: At present, the layout of active area consists of pixels that form the images in an off and on state. This arrangement differs OLED/LCD from cathode-ray tube (CRT). The pixels are arranged in two ways--passive-matrix and active-matrix display. In case of passive-matrix, electrodes are deposited as row on one side of the emissive layer and as column on other side of the layer. The intersection of row and column constitute the pixel. However, with the increase of numbers of column and rows, the operation voltage needs to be increased and the contrast of the devices decrease[8]. All these problems have been solved by addressing each pixel that has its own electrode, driven by thin-film transistor (TFT) and capacitors-termed as active-matrix[8]. AMOLED (active matrix organic light emitting diode) is intrinsically superior to existing display devices because an OLED pixel is an emissive type which can be switched off and be completely black increasing the unmatched contrast and resolution where as the backlight should be always "on" in case of LCD[8]. Among all advantages, low power consumption and better image quality are the reason why AMOLED are being used for portable devices such as car stereo, smart phone, PDAs since the first mass production of AMOLED in 2007[8]. Most recently commercialization of OLED TVs are offing such as 4K ultra high definition full colour, thin, curved OLED TVs by LG, Samsung, Sony and other major player of TV industries. Even foldable and roll over smart phone has been demonstrated by Samsung. Moreover, OLED has been considered as building block for transparent display because OLEDs require only low operation voltages (~2–4 V) , have high brightness levels <10 000 cd/m^2 with efficiencies in the order of 110 lm/W and can be designed to transmit more than 80% of visible light[11]. A transparent display is like an ordinary window being just see- through, when it is activated; information could be displayed without the use of projector[11]. Such display has wide range of application such as transparent display integrated windows of vehicles in public transport (buses, trains, etc.), hotels, public space, and stores to provide information for an augmented reality of the outside world[11]. Similarly, OLED integrated in goggles, helmets or windshields could be used by surgeons, police or fire fighters to display essential information or warning messages that might help to save lives[11]. Recently, Samsung exhibited transparent 3D interactive OLED display by which customers can see themselves and same time see on screen image. It is evident that OLED displays is rapidly growing and is the future of display industries.

(b) OLED as light source: The OLED as lighting device is a relatively new application and earned intense interest for such application because OLEDs offer great potential for providing high power efficiency at low operational voltage and low operating temperature in addition to other many interesting features, such as flexibility or transparency. Moreover, OLED can be operated at lower luminous intensity to get the same luminous flux simply by expanding the emission area without much heat generation thereby facilitating the implementation of large area inflexible and flexible lighting systems, flat panel lighting. The requirements of OLED for lighting are vastly different from display technology. For display technology, single colour pixels can form full colour devices but white light is required for general lighting application. White light has three characteristics (i) the Commission International d'Eclairage (CIE) coordinates-the good position close to (0.33, 0.33) on the CIE-1931 diagram (ii) the co related colour temperature (CCT) and (iii) the colour rendering index (CRI) (>75)[9]. To obtain high quality (high CRI) white light, all the three primary colours red, green, and blue have to be produced simultaneously which is difficult to obtain from single emissive layer. Thus generally white light from OLEDs are generated by two methods i.e. (a) colour mixing and (b) wavelength conversion. In colour mixing, white light is obtained by mixing two complementary colours (blue and orange) or three primary colours (red, green and blue)[4]. Different device architectures have been shown in Fig. 5.
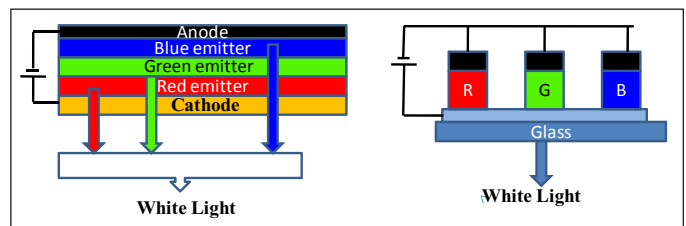

Fig. 5. Device layouts to realize white light emission. i) Vertically stacked OLEDs, ii) pixelated monochrome OLEDs, R, G, and B stand for red, green, and blue, respectively.
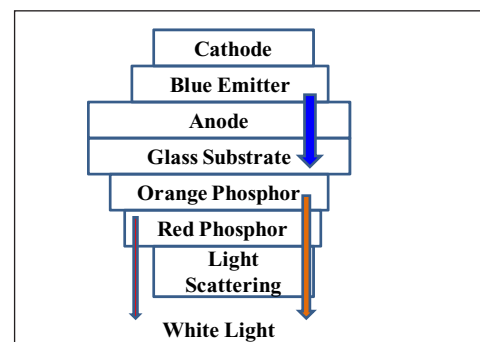

Fig. 6. Schematic diagram of white light emission by down conversion

Table 2: A few examples of colour, material and efficiency of OLED[4,8]

Colour	Material	CIE	External Quantum Efficiency (%)	Luminous efficiency lmW^{-1}
Blue	BCzVB doped CBP,	(0.15, 0.16)	2.6	-
	BCzVB doped DPVBi	(0.15, 0.14)	5.7	-
Green	Alq3	(0.39, 0.55)	-	-
	DMQA doped Alq3	(0.39, 0.59)	-	-
Red	DCJTB doped Alq3	(0.64, 0.36)	-	0.9
	DCJTB and Rubrene doped Alq3	(0.64, 0.35)	-	1.2
White	DCJTB doped SAlq	(0.33,0.39)	2.0	2.3
	FIrpic and Ir(SBFP)2(acac) dispersed in polymer P36HCTPSi. silsesquioxane-terminated	(0.41, 0.49)	14.1	25.6
	poly(9,9-dioctylfuorene) (PFO-poss): Ir(Bu-ppy)3] : [(Piq)2Ir(acaF)	(0.33, 0.33)	-	5.5

BCzVB = 4, 4_-(bis(9-ethyl-3-carbazovinylene)-1,1_-phenyl.

DCJTB = 4-(dicyanomethylene)-2-t-butyl-6(1,1,7,7-tetramethyljulolidyl-9-enyl)-4H-pyran.

DMQA = N, N_-dimethylquinacridone, DPVBi = 4, 4_-bis(2,2_-diphenylvinyl)-1,1_-biphenyl, SAlq = bis(2-methyl-8-quinolato)-(triphenylsiloxy) aluminium(III).

By using dopants, a wide range of colours from greenish-blue to orange-red can be obtained.

In wavelength conversion, blue or ultraviolet light emitter OLED is used to excite several phosphors, each of which emits a different colour. These emitted colours are mixed to make a white light with the broadest and richest wavelength spectrum as shown Fig. 6. For example, white light emission has been shown using a blue OLED coupled with perylene orange (orange emitter) and perylene red (red emitter) dispersed in poly (methacrylate) (PMMA) followed by a layer of Y(Gd)AG:Ce dispersed in polydimethyl siloxane silicon[12]. Table 2 presents a list of emissive layer and their combination, which emits light of different colour.

Future challenges and opportunities

OLEDs have the potential to bring paradigm shift of display and lighting industry. Already as a display, OLED is in the marker for decades, particularly display for small portable devices such as cell phones, smart watches, tablets, cameras, and other devices. Recently, the large-scale OLED-based display like TV has entered in to market and is challenging LED and LCD display. To sustain in the market, the efficiency and lifetime need to be increased[11]. At this moment, cost of AMOLED TV is two to three times higher than LCD. Anyway, the cost would be reduced by large volume production. The transparent OLED display is the next technology that could open-up new application as discussed above. At this moment, major challenges are the excessive light loss, transparent conductive oxide (TCO) for cathode and the disruption of displayed images due to light coming from the background[11].

OLED is the latest entrant in lighting application and challenging existing lighting such as fluorescent and LED lighting. It is poised to change general indoor lighting, outdoor lighting, specialty applications, and automotive lighting[6,9,11]. It is anticipated that flexible OLED lighting panels will find opportunities in designer aesthetic lighting. Even OLED lighting could directly embeddable onto architectural materials, such as metal and glass, and can be used to create freeform luminous objects, as well as decorative lighting applications in stairways, windows, dividing wall which are not possible with other existing lighting sources. It is proposed that OLED panel could be integrated to organic solar cell (OSC) to make a self-powered OLED lighting system[11]. Such panel generates power by absorbing the sunlight in the daytime, which can be used for operating OLED lighting panels in the evening. Since the transparent OLED panel emits light from both front and rear sides, the rare side light can be used to power generation by OSC where as front sidelight would be used for illumination[11].

Therefore, it means that large-area panels are needed to produce enough light for lighting applications. The average luminous output of 4″ and 6″ recessed down lights is about 600 lm. An OLED panel operating at 2000 cd/m^2 luminance produces about 6000 lm/ m^2. Since current efficiency for a good single-unit OLED is around 50 cd/A or 150 lm/A, to produce 600 lm requires more than 4 A of current[9, 11]. The transparent ITO electrode layer has a sheet-resistivity of around 10 ohms/ sq, so the 4 A current produces an IR drop across the ITO that is too large in comparison with the drive voltage (3 V). Thus this cause significant power loss and non-uniformity in light output. Moreover, the thin organic layer is sandwiched between two conducting electrodes, thus small pinhole or particle defects cause shorting which could decrease power, and if the shorting is more, then device would be completely died[9]. In addition, OLEDs degrade in presence of moisture and oxygen, which is the biggest challenge for long time stability of OLED lighting[9, 11]. Though rapid development of materials and their processing have improved OLED lighting performance, more work is needed to succeed in the lighting marketplace.

References:

1. VanSlyke, S. A. & Tang, C.W. (1985). Organic electroluminescent devices having improved power conversion efficiencies, US Patent 4539507.

2. C. W. Tang and S. A. Van Slyke, Organic electroluminescent diodes, Appl. Phys.Lett. **1987**, 51, 913.

3. http://energy.gov/sites/prod/files/2015/06/f22/ssl_rd-plan_may2015

4. S. Reineke, M. Thomschke, B. Lüssem, and K. Leo,Rev. Mod. Phys. **2013**, 85, 1245.

5. M. Pope, H.P Kallmann, P. Magnante, P. (1963). J. Chem. Phy. *1963*, 38, 2042.

6. R. Pode and B. Diouf, Solar Lighting, Springer: London, 2011

7. W. Brütting, , S. Berleb, A. G. Mückl, Org. Elect. **2001,** 1, 1

8. B. Geffroy,P. l. Roy and C. Prat, Polym Int. 2006, 55, 572.

9. D. J. Gaspar, E. Polikarpov, OLED Fundamentals, CRC Press, New York, 2015,

10. M. A. Baldo, D. F. O'Brien, Y. You, A. Shoustikov,S. Sibley, M. E. Thompson & S. R. Forrest, Nature, 1998, 395, 151.

11. A. Buckley,Organic light- emitting diodes (OLEDs), Woodhead: , Cambridge, 2013.

12. A. R. Duggal, J. J. Shiang, C. M. Heller and D. F. Foust, Appl. Phys. Lett., **2002,** 80, 3470.

	Dr. S.P. Koiry *joined BARC in 2004 as Scientific Officer after obtaining his M.Sc. (Chemistry) from Assam University, Silchar. He is currently working on monolayer/ multilayers of electrographhted silane molecules, porphyrin derivatives and, organic dyes and self-assembled monolayers for organic electronics and photovoltaic applications*
	Dr. D. K. Aswal *joined BARC in 1986 through 30th Batch of Training School after completing M.Sc. (Physics) from Garhwal University and is presently Head of Thin Films Devices Section. His area of scientific interest is condensed matter physics, specializing in device-oriented research leading to hybrid molecule-on-Si nanoelectronics, thermoelectric devices, and gas sensors. He is a recipient of several international fellowships including, JSPS fellowship, Japan (1997-99), IFCPAR fellowship, France (2004-05), BMBF fellowship, Germany (2006) and CEA fellowship, France (2008). He is recipient of several awards, including "MRSI Medal 2010", "Homi Bhabha Science and Technology Award-2007", "DAE-SRC Outstanding Research Investigator Award-2008", and "Paraj: Excellence in Science Award, 2000, Honorary Guest Professor,(2015-17),Shizuoka University, Japan,Distinguish Faculty Award of HBNI, 2015.*

Detection of Oral Cancer-The Photonics Way

Shovan K. Majumder and Hemant Krishna

Optical Spectroscopy and Diagnostic Lab, Raja Ramanna Centre for Advanced Technology, Indore 452013
E-mail: shkm@rrcat.gov.in; shovan.k.majumder@gmail.com

Abstract

There is an increasing current interest in using photonics based techniques for automated, noninvasive and real-time detection of oral cancer. A brief overview of the research being pursued on the application of different variants of optical spectroscopy for detection of oral cancers and pre-cancers is presented in this article.

Background and Motivation

Oral cancer is one of the highly prevalent cancers in India and its incidence is on a rise due to consumption of tobacco and pan masala.[1] Diagnosis of oral cancer at an early stage provides the patient with a considerably greater chance of successful treatment and less treatment-associated morbidity than when it is diagnosed at a late stage. Currently, the most widely used test for screening of oral cancer is visual examination of the oral cavity.[2] The process, being subjective, often fails to satisfactorily detect changes in oral mucosa associated with early cancers or pre-cancerous alterations that generally precede invasive cancers. Although, over the years, several new approaches like the use of brush cytology, toludine blue staining, Lugol iodine and Methylene blue solution, reflectance visualization after acetic acid application, and illumination with a chemiluminescent light source have been proposed to address the limitations of the conventional oral examination[3-4], due to a high rate of false positives generally associated with these methods there is an urgent current need for alternative diagnostic methods that can enhance the visual assessment of oral lesions and particularly help discriminate premalignant and benign lesions.

Optical spectroscopy, in recent years, has been suggested and validated as a powerful alternate tool that can help solve all these problems.[5-8] Its major attraction stems from its ability to provide biochemical and morphological information about the tissue in a minimally invasive or noninvasive manner. Most of the optical spectroscopy work has been performed using fluorescence spectroscopy, diffuse reflectance or elastic scattering spectroscopy and Raman spectroscopy.[8-10] Of these, fluorescence spectroscopy is the one that has been most widely researched for the detection of oral lesions followed by diffuse reflectance spectroscopy either alone or in combination with fluorescence spectroscopy. Only in recent years Raman spectroscopy has joined the league. However, the applications of Raman spectroscopy in this area are still in the early stages of development.

Fluorescence:

The motivation for using fluorescence spectroscopy for diagnosis of oral tissue pathologies is that fluorescence is sensitive to the biochemical make-up of the tissue.[5-6] Tissue contains several fluorescent bio-molecules such as NADH, elastin, collagen and cofactors like flavins (FMN, FAD), porphyrins etc. By measuring the UV-induced fluorescence from tissue (called "autofluorescence") it should, in principle, be possible to learn about the relative concentrations and redox states of such compounds and in turn to learn about the biochemical state of the tissue. However, interpretation of tissue autofluorescence is difficult due to intrinsic scattering and absorption properties of the tissue, rendering autofluorescence measurements significantly more complicated than measurements of fluorophores in dilute solution. Despite these difficulties several studies over the years have shown that fluorescence spectroscopy can be used for optical diagnosis of oral lesions. Either single-point or imaging measurements have been performed. The technological encumbrances of each approach are different. While point measurements provide spectroscopic information from a single tissue site, the spectral imaging provides a modest amount of spectral information from a significantly larger area of a tissue surface. Some of the earliest works on the use of fluorescence spectroscopy for tissue analyses by the MIT group[11] as well as our group[12] addressed differences in the UV-induced fluorescence in oral tissues belonging to different pathological states. In the recent years, several small clinical studies[13-18] on fluorescence spectroscopy for *in-vivo* oral cancer detection demonstrated that the fluorescence intensity from healthy oral mucosa was generally greater than that from the abnormal one. Algorithms developed on the basis of the differences in fluorescence spectra could discriminate healthy mucosa from dysplastic and cancerous tissue with high sensitivity and specificity.[13-18] Everything put together, these results suggest that fluorescence spectroscopy can provide a simple, objective tool to improve *in-vivo*

identification of oral neoplasia. Recently, the U.S. Food and Drug Administration approved an autofluorescence imaging device for early detection of oral neoplasia.[19] The commercial device, marketed as the VELscope® (LED Dental, Inc., White Rock, BC, Canada), employs a blue/violet light (400 – 460 nm wavelengths) for illuminating oral tissue and uses optical filters (long pass and notch filters) for enabling doctors directly visualize fluorescence inside the oral cavity.[19] The VELscope and other fluorescence imaging devices proposed in the literature work on the basis of qualitative observations for detecting and delineating neoplastic oral lesions. These instruments, therefore, require standardized image interpretation modalities and appropriate user training for reliable screening of the oral cavity.

Diffuse Reflectance:

Diffuse reflectance spectroscopy measures the light that undergoes multiple elastic scattering events within the tissue before emerging out of the tissue surface, thereby providing morphologic information about the tissue.[6,9,18] It also bears the signature of absorption by various chromophores present within the tissue, thus providing some amount of biochemical information about these absorbing chromophores. In the UV-visible region the most dominant chromophore is hemoglobin, with the oxygenated and deoxygenated forms having different absorption spectral features. The method of diffuse reflectance is sensitive to the changes associated with the sub-cellular architecture, which generally reflect in the morphological parameters (such as nuclear to cytoplasm ratio, mitochondrial size and density etc.) used during histological assessment of tissues.[20] It is also sensitive to the ultra-structural features that are beyond the limit of Abbe resolution for optical microscopy, and thus provides information which otherwise are not possible to obtain from conventional histology.[20] Diffuse reflectance spectroscopy has proved to be a promising tool for detecting premalignant and malignant changes in the oral tissues, with high sensitivity and specificity.[21] Several clinical *in-vivo* studies have used diffuse reflectance either alone or in combination with fluorescence spectroscopy with very promising results.[9, 18]

Raman:

Raman spectroscopy has the distinct advantage over fluorescence or diffuse reflectance in that it has the intrinsic ability to detect molecular "fingerprint" information in a tissue in a greater detail than either of the two techniques. Basically, it probes the vibrational energy levels of molecules, and specific peaks in the Raman spectrum correspond to particular chemical bonds or

bond groups.[7] Consequently, there is a strong rationale for using Raman spectroscopy in the detection of oral lesions since it has the ability to discern subtle biochemical changes associated with neoplastic transformation. Four important components of biological tissues that contribute to the Raman spectra are proteins (including collagen), lipids, nucleic acids and water. However, early attempts at measuring *in-vivo* Raman spectra of human oral cavity were difficult because of the fluorescent nature of tissue and limitations of sources and detectors.[7] With continued improvements in detectors and spectroscopic systems, it has now become possible to acquire good quality tissue Raman spectrum in a clinically acceptable data collection time.[7] Further, portable, powerful and stable diode lasers emitting wavelengths in the "optical window" of tissue (e.g. 785 nm and 830 nm) where they generate minimal background fluorescence while penetrating fairly deeply into tissue are now readily available. All these technological improvements have motivated several groups[7,22] including ours[23-25] to carry out *in-vivo* Ramzgnostic specificity and sensitivity and will be worth tracking in coming years.

Use of optical spectroscopy for detecting oral neoplasia-studies at RRCAT:

We at Raja Ramanna Center for Advanced Technology (RRCAT) have been actively pursuing activities on the evaluation and development of optical spectroscopic techniques for oral cancer diagnosis. Our initial work was primarily aimed at proving the hypothesis that light scattered from a tissue allows one to determine its pathological status. The extensive studies[12, 26-29] on tissue samples resected at surgery or biopsy from different organs led to an important discovery that under illumination with ultraviolet light from a nitrogen laser while the cancerous breast tissues were considerably more fluorescent than the non-cancerous breast tissues, the reverse was the case with tissues from the oral cavity. This paradox was resolved and attributed to the variation in concentration of various fluorophores, particularly that of the coenzyme NADH, which is known to be an important participator in cellular metabolism and also gets optimally excited at nitrogen laser wavelength. It was found that while higher concentration of NADH was present in cancerous breast tissues compared to the benign tumor and normal breast tissues, the reverse was the case for tissues from the oral cavity. This spectroscopic inference, subsequently confirmed through enzymatic measurements, not only accounted for the contradictory spectral differences, but also explained why illumination with nitrogen laser led to significant difference in the fluorescence from normal and malignant sites of these tissue types.

Having evaluated the applicability of optical spectroscopy for differential diagnosis of cancer, major efforts were directed towards developing an optical spectroscopic device suitable for *in-vivo* clinical use in patients with oral cancer. The first prototype system developed at RRCAT for clinical *in-vivo* studies was a trolley based fluorescence spectroscopy setup comprising an in-house built, sealed-off nitrogen laser (pulse duration, 7ns; pulse energy, 10mJ; and pulse repetition rate, 10Hz), an optical fiber probe, and a gateable intensified CCD (ICCD) detector.[14] One such unit was used at the Government Cancer Hospital, Indore for a detailed clinical evaluation of the technique after satisfactory results were obtained in a pilot study on 25 patients with histopathologically confirmed squamous cell carcinoma of oral cavity.[14] The limited database of *in-vivo* fluorescence spectra recorded from more than 68 patients enrolled at out-patient department of the Government Cancer Hospital Indore, for screening of neoplasm of oral cavity and ~30 healthy volunteers was used to develop state-of-the-art statistical pattern recognition based diagnostic algorithms that could efficiently (with accuracy of ~ 90% in general and up to 100% in favorable cases) discriminate between the spectral features of the malignant and non-malignant tissue sites.[13] In the next phase, with the further improvement in technology, it was possible to develop a more compact version of the fluorescence spectroscopy system by replacing the ICCD with a chip-based miniaturized Ocean optics spectrometer and the relatively larger nitrogen laser with a home-built miniaturized, sealed-off one and accommodating everything in one single box. This compact system was used at Tata Memorial Hospital (TMH), Mumbai, along with a portable suitcase-based Raman spectroscopy system assembled in-house for a comparative analysis of these two different approaches for the screening of the neoplasm of oral cavity.[23] In a study at TMH involving ~200 subjects, while the multi-class (squamous cell carcinoma, oral sub-mucosal fibrosis, leukoplakia or normal tissue) classification accuracy using Raman spectroscopy was found to be significantly better (92% vs. 83% for fluorescence), because of higher molecular specificity of Raman signal, the binary (normal vs. abnormal) classification accuracy for the fluorescence spectroscopy (91%) system, which is simpler and less expensive, was comparable to that for Raman (94%). Another interesting outcome of the study was that if the spectra acquired from healthy volunteers with no clinical symptoms, but having tobacco consumption history were removed from the 'normal' data base a significant improvement in classification accuracy was observed for both fluorescence and Raman spectroscopy based diagnosis.

In order to facilitate the routine use of the spectroscopic system at a hospital or a community setting, it is necessary to automate and simplify each aspect of the spectral measurements in addition to the data analysis. Having this objective in mind and with the availability of high brightness ultraviolet (~365nm) light emitting diodes (LEDs), an LED based, USB powered, compact and portable diagnostic system capable of providing automated diagnostic feedback was recently developed (Fig.1). The new LED based system has several advantages over the nitrogen laser based fluorescence system that was used earlier at TMH. First, it is more rugged and overcomes the various problems (like the random failure of the spark gaps, periodic degassing of the nitrogen from the glass tubes etc.) associated with the earlier system. Second, in contrast to the earlier system, it can record both fluorescence and diffuse reflectance spectra sequentially in one go from a given tissue site providing an opportunity to get improved diagnostic inputs. The hardware control, data acquisition and documentation are fully automated and governed by a Graphical User Interface (GUI) software developed in house. While being able to save the spectral data recorded from different sites of the oral cavity, the software can also simultaneously register the histological identity of the investigated sites as determined by the concerned physician based on visual inspection. An additional advantage of the software is that it has also the ability to deliver automated diagnosis based on the database of optical spectra that will be stored therein.

This LED based system was used at TMH to acquire spectral data from patients (with various oral lesions) as well as healthy volunteers. The *in-vivo* spectra showed a variety of differences between the different tissue types consistent with the earlier observations. For the fluorescence spectra, the most prominent differences were seen in the 460nm and 635nm spectral bands. While the 460nm spectral band was the most intense in healthy squamous tissues, the intensity of the 635nm band was the highest in the spectra from malignant lesions. The diffuse reflectance spectra showed dips around 400–450, 540–550, and 570–580 nm characteristics of blood absorption and the extent of these dips were observed to be different implying significant variations in the concentration of hemoglobin in the different tissue types. In order to evaluate the diagnostic content of the spectral data, the whole set of spectra was divided into training and test sets such that both sets have no overlap of data from the same patients. The diagnostic algorithm developed earlier was optimized using the training set data and validated on the test set data in order to have an unbiased estimate through

Figure 1. A USB powered, LED based combined fluorescence and diffuse reflectance system capable of providing automated diagnosis.
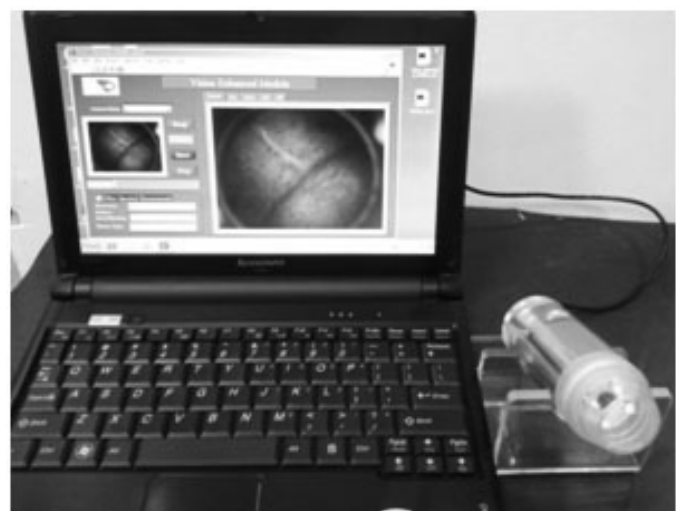

Figure 2. A portable fluorescence imaging device for large area scanning of tissue.

independent cross-validation. The algorithm was found to provide considerably better accuracy in classifying different tissue pathologies when applied on the combined fluorescence and diffuse reflectance spectra as compared to that obtained when it was applied on either fluorescence or diffuse reflectance spectra alone. The classification results for combined fluorescence and diffuse reflectance spectra showed an average sensitivity and specificity of 75% and 95% towards malignant (SCC) and 58% and 68% towards potentially malignant (SMF and LPK put together) lesions. However, if spectral data only from buccal mucosa were considered for analysis, the sensitivity and specificity improve to 83% and 100% towards malignant and 83% and 77% towards potentially malignant lesions.

The spectroscopic system was also used at oral cancer screening camps for enhancement of database in particular for potentially malignant oral lesions. Analysis of spectral data measured from ~200 patients provided an accuracy of ~75% with respect to visual assessment of the examining doctor in detecting potentially malignant lesions. Since in the camps the spectra were recorded primarily by doctors having little or no experience of oncology, further studies are being planned to acquire spectra in a controlled environment from patients with potentially malignant lesions clinically/pathologically certified by an experienced oncologist/ onco-surgeon so as to improve the accuracy in detecting potentially malignant oral lesions. Further, the point-spectroscopy system integrated with a wide area fluorescence imaging system developed recently (Fig.2) is expected to serve as a standalone automated cancer screening tool for screening population at risk in remote areas.

References:

1. A. Jemal, R. Siegel, E. Ward, Y. Hao, J. Xu, M. J. Thun, *CA Cancer J Clin.* **2009**, 59, 225.
2. P. E. Petersen, *Oral Oncol.* **2009,** 45: 454.
3. M.W. Lingen, J. R. Kalmar, T. Karrison, P.M. Speight, *Oral Oncol.* **2008**, 44:10.
4. M. P. Rosin, C. F. Poh, M. Guillard, P. M. Williams, L. Zhang, C. MacaUlay, *Ann. N. Y. Acad. Sci.* **2007**, 1098:167.
5. N. Ramanujam, *Neoplasia* **2000**, 2:89.
6. I. J. Bigio, S. G. Bown, *Cancer Biol. Ther.* **2004**, 3:259.
7. A. Mahadevan-Jansen, *Biomedical Photonics Handbook*, T. Vo-Dinh, 30:1-27, CRC Press: Washington DC, 2003.
8. D. C. de Veld, M.J. Witjes, H.J. Sterenborg, J.L. Roodenburg, *Oral Oncol.* **2005**, 41:117.
9. R. A. Schwarz, W. Gao, D. Daye, M. D. Williams, R. Richards-Kortum, and A. M. Gillenwater, *Appl. Opt.* **2008**, 47:825.
10. M. J. H. Witjes, *Head Neck Oncol.* **2009**, 1(Suppl 1):O8.
11. J. K. Dhingra, D. F. Perrault, K. McMillan, E. E. Rebeiz, S. Kabani, R. Manoharan, I. Itzkan, M. S. Feld, S. M. Shapshay, *Arch. Otolaryngol. Head Neck Surg.* **1996,** 122:1181.
12. S. K. Majumder, A. Uppal, P. K. Gupta, *Lasers Life Sci.* **1999**, 8:211.
13. S. K. Majumder, A. Gupta, S. Gupta, N. Ghosh, P. K. Gupta, *J. Photochem. Photobiol. B* **2006**, 85:109.
14. S. K. Majumder, S. K. Mohanty, N. Ghosh, P. K. Gupta, D. K. Jain, F. Khan, *Curr. Sci.* **2000**,79:1089.
15. P. Chaturvedi, S. K. Majumder, H. Krishna, M. Sidramesh, P. K. Gupta, *J. Cancer Res. Ther.* **2010**, 6:497.
16. R. A. Schwarz, W. Gao, D. Daye, M. D. Williams, R. Richards-Kortum, A. M. Gillenwater, *Appl. Opt.* **2008** 47: 825.

17. A. Amelink, O. P. Kaspers, H. J. C. M. Sterenborg, J. E. van der Wal, J. L. N. Roodenburg, M. J. H. Witjes, *Oral Oncol.* **2008**, 44: 65.

18. D. C. G.de Veld, M. Skurichina, M. J. H. Witjes, R. P. W. Duin, H. J. C. M. Sterenborg, J. L. N. Roodenburg, *Lasers Surg. Med.* **2005**, 36:356.

19. C. F. Poh, L. Zhang, D. W. Anderson, J. S. Durham, P. M. Williams, R. W. Priddy, K. W. Berean, S. Ng, O. L. Tseng, C. MacAulay, M. P. Rosin, *Clin. Cancer Res.* **2006**, 12:6716.

20. T. Uplie, W. Jerjes, H. J. C. M. Sterenborg, A. K. E. Maggar, A. Sandison, M. J. H. Witjes, M. A. Biel, I. Bigio et al., *Head Neck Oncol.* **2009**, 1:25.

21. R. Mallia, S. S. Thomas, A. Mathews, R. Kumar, P. Sebastian, J. Madhvan, N. Subhash, *J. Biomed. Opt.* **2008**, 13:041306.

22. M. S. Bergholt, W. Zheng, Z. Huang, *J. Raman Spectrosc.* **2012**, 43:255.

23. S. K. Majumder, H. Krishna, M. Sidramesh, P. Chaturvedi and P. K. Gupta, *Proc. SPIE* **2010**, 8173, 817306, doi:10.1117/12.898904.

24. H. Krishna, S. K. Majumder, P. Chaturvedi, and P. K. Gupta, *Biomed. Spectrosc. Imaging* **2013**, 2:199.

25. H. Krishna, S. K. Majumder, S. Muttagi, P. Chaturvedi, P. K. Gupta, *J. Biophotonics* **2014**, 7:690.

26. S. K. Majumder, P. K. Gupta, B. Jain, A. Uppal, *Lasers Life Sci.* **1999**, 8:249.

27. B. Jain., S. K. Majumder, P. K. Gupta, *Lasers Life Sci.* **1998**, 8:163.

28. P. K. Gupta, S. K. Majumder, A. Uppal, *Lasers Surg. Med.* **1997**, 21:417.

29. S. K. Majumder, A. Uppal, P. K. Gupta, *Curr. Sci.* **1996**, 70.

Dr. Shovan Kumar Majumder is senior Scientist (SO-H) at Raja Ramanna Centre for Advanced Technology (RRCAT), and Professor at Homi Bhabha National Institute (HBNI). He leads the activity on Optical Spectroscopy and Imaging for Biomedical Diagnosis at RRCAT.

Dr. Majumder received his graduate and postgraduate degrees in Physics from Jadavpur University, Kolkata. After successful completion of one-year Orientation Course from Bhabha Atomic Research Centre (BARC) Training School, Mumbai, he joined RRCAT in the year 1992. He received his Ph.D. degree from Devi Ahilya University, Indore for his work on the use of Optical Spectroscopy for Cancer Diagnosis. He worked as a visiting scientist at Vanderbilt University, USA where he did the post doctoral research in the same field. Dr. Majumder's main research interest is development and evaluation of optical spectroscopic techniques for biomedical diagnosis and imaging. His other interests include use of various statistical pattern recognition techniques for the development of diagnostic algorithms for classification of tissue pathologies and development of optical techniques for monitoring the authenticity and the quality of food and pharmaceutical products.

Shri Hemant Krishna obtained his B.Sc. in Mathematics and Physics from the Lucknow University, Lucknow in 2005. He obtained his M.Sc. in Physics from the Banaras Hindu University, Varanasi in 2007. He received his M. Tech degree from the Homi Bhabha National Institute, Mumbai in 2011. Currently he is working at Raja Ramanna Centre for Advanced Technology (RRCAT), Indore and is actively involved in the development and evaluation of optical spectroscopic techniques for biomedical diagnosis and imaging.

Polymers in Optical Components & Devices: An Overview

Dinesh V Udupa

Atomic & Molecular Physics Division, Bhabha Atomic Research Centre, Mumbai-85
Email: dudupa@barc.gov.in

Abstract

Optical polymers have gained wide spread applications in a variety of optical devices and instruments in the recent years including opto-electronic, photonic, waveguide optics, fiber optic, integrated optical devices and lasers. The article presents an overview of optical polymers in consumer optics as well as high end optics being used currently with a focus on various key aspects and properties of the materials. Polymers specific to refractive optics, non-linear optics and optical fibers photonics have been discussed.

Introduction

Traditionally optical components and devices have been made of optical glasses such as silicates and borosilicates, with various dopants such as barium, lanthanum, lead, phosphorous, etc. Glass optics offers various advantages such as excellent light transmission, high manufacturing precision and diverse choices in refractive index offering good flexibility in optical design. Chemically, glasses are quite stable and can withstand harsh environments with higher thermal stability which is a merit for high optical power applications. Among the chief demerits of glass optics are the difficulty of fabrication and the cost where aspherics or free-form surfaces with complex component geometries are concerned, since the surfaces have to be optically polished in a separate process. Polymers have increasingly found application in optics as a substitute to glass over the years[1]. This trend is poised for a rapid increase in the future with developments of newer optical grade polymers aiming at better opto-mechanical qualities. Optical polymers with highly polished complex surface shapes having intricate component geometries are now being manufactured in the industry. Optical polymers have an additional advantage of cost where mass manufacture is concerned with added merits of being less brittle and are light weight, aiding their popularity in application in wide variety of consumer goods such as CD, DVDs, cameras in mobiles, and computers, hand held scanners, LED lenses, etc. With recent advances in polymer material technology, plastic are now common in more high-end optical applications, including fiber optics, biomedical devices, biometric scanning, and the displays and devices used in defense and security[2]. Among the demerits of optical polymers is the presence of optical birefringence where light is doubly refracted giving undesirable effects. This problem is more of a process dependent effect introducing stress and have been controlled with materials having lower flow rates.[2,3] Another limitation in optical application is the relatively lesser refractive index and dispersion choices provided by polymers, which is now over come using hybrid glass-polymer optics in high end applications.

Polymers in refractive optics

Refractive optics include optical components such as lenses, prisms, windows or their combinations used for manipulating light in an instrument. A typical assortment of diamond turned polymer optics being manufactured currently in the industry[4] is shown in Fig. 1. Observe the odd shaped, very thin or highly curved optical components (Fig. 1) which are easier to fabricate using polymers as compared to glass.

Fig. 1. Some diamond turned aspherical polymer optics[4]

Of the various varieties of polymers used in manufacturing optics, the most common kinds are Polycarbonates, Acrylics/ PMMA and Polystyrene. Polycarbonates (PC) are a group of thermoplastic polymers containing carbonate groups in their chemical structures. An example of a polycarbonate is shown in Fig. 2. Polycarbonates used in engineering are strong, tough materials, and the optical grades are light transparent. A major application of polycarbonates is in optical storage devices such as CDs, DVDs and Blu-Ray Discs[5].

Acrylic (polymethylmethacrylate, or PMMA) is also one of the commonly used polymer for optics. PMMA
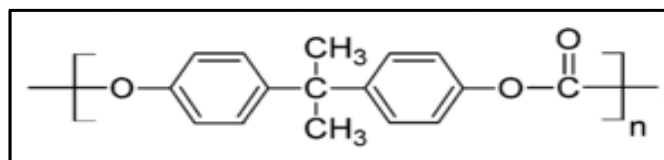

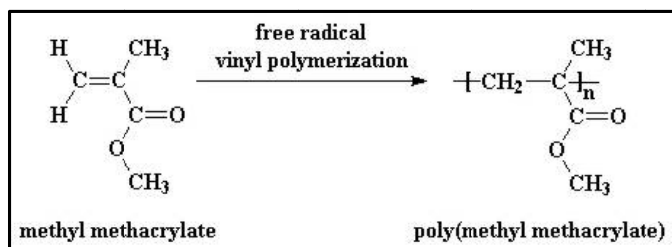*Fig 2. Polycarbonate (PC) chemical structure unit made from bisphenol A*

Fig. 3. Chemical structure of PMMA

is an ester of methacrylic acid (CH_2=$C[CH_3]CO_2H$) and belongs to the acrylic family of resins produced from the polymerization of methyl methacrylate. Fig. 3 shows the constituent monomer structure of PMMA. The polymer has good clarity and high transmittance in the visible light, but is not as mechanically tough as polycarbonates[6]. PMMA is an economical alternative to polycarbonate when strength is not necessary. As an additional merit, PMMA also does not contain the potentially harmful bisphenol-A subunits found in polycarbonates and is easier to handle. However, PMMA is more prone to scratching due to lower hardness compared to polycarbonates.

Polystyrene (PS) is a synthetic aromatic polymer made from the monomer styrene (Fig 4), which is a liquid petrochemical. Polystyrene can be foamed, finding applications in packaging industry, whereas rigid
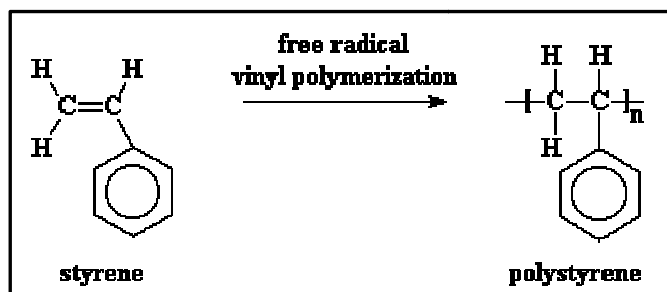

Fig. 4. Chemical structure of polystyrene (PS)

polystyrene is optically transparent and hard, suitable in optical applications. It is also very inexpensive resin per unit weight. It is a rather poor barrier to oxygen and water vapor and has relatively low melting point[7]. In optical lens applications, a combination of different refractive index material is often needed for dispersion corrections. Here polystyrene forms a good achromatic pair with acrylic. Polystyrene is similar to polycarbonate and has high impact strength and good performance over broad temperatures – up to 120 °C. Polymers having only hydrogen and carbon such as polystyrene are water resistant and non hygroscopic. In contrast, PMMA and polycarbonate polymers have a tendency to absorb water due to presence of oxygen and oxyhydrogen groups which can significantly alter some key optical properties such as refractive index and dispersion[8].

Styrene acrylonitrile (SAN) is another plastic material used in optical applications. It is a copolymer plastic consisting of styrene and acrylonitrile. The chains of the polymer have alternating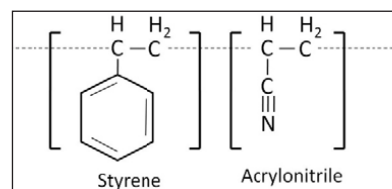 units of styrene and acrylonitrile, as shown in Fig. 5. The relative composition is typically between 70 and 80% by weight styrene and 20 to 30% acrylonitrile[9]. It is widely used in place of polystyrene owing to its greater thermal resistance. The mechanical properties and chemical resistance

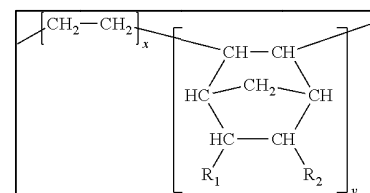*Fig. 5. The structure of co-polymer Styrene Acrylonitrile (SAN)*

Fig. 6. The chemical structure of co Cyclo Olefin Copolymer (COC)

is generally improved with larger acrylonitrile content, but it also results in a yellow tint to the normally transparent plastic[10], an undesirable effect for optical applications.

Although advances in polymer materials were slow earlier, several recent breakthroughs in newer polymers have improved options available for temperature ranges, transmission quality and stability of the index of refraction for optical applications[3]. Several new grades of acrylic deliver relatively high transmission quality from 300 nm to 1600 nm wavelengths with improved temperature operating ranges with low thermal expansion. One of the issues with polymer optical materials is the presence of birefringence in these materials, which limits their functionality in high end applications. Recently developed Cyclo Olefin Copolymer (COC) feature much lower birefringence and extremely low moisture absorption, relating directly to the stability of the index of refraction.[3,11] The polymer also has high transparency, purity, high heat resistance and good moldability. Zeon Corp., a Tokyo-based supplier manufactures COC called Zeonex K26R which is specifically used in smartphones and tablet-PC camera lenses[12]. Fig. 6 shows the chemical structure of this class of polymers.

In recent developments, Polyetheramides (PEI) are also now available in optical grades. These plastics having higher refractive index exhibit higher transmission quality than previously possible in the near-IR and withstand operating temperatures[3] from below zero to above 210 °C.

Optical properties

While refractive index at various wavelengths is an important optical property of a material besides

transmission and absorption, other properties such as dispersion (Abbe number) (v), relative partial dispersion (P), thermal coefficient of refractive index ($\Delta n/\Delta T$) are crucial with design point of view. Table 1 shows refractive index of optical polymers at various important wavelengths[13].

The Abbe number is defined as $v_d = \frac{n_d - 1}{n_F - n_C}$ where n is the refractive index and the suffixes d, F and C denotes wavelengths 587.56nm, 486.13nm and 656.27nm respectively. Abbe number at IR wavelength of 879 nm (v_{879}) is defined as $v_{879} = \frac{n_{879} - 1}{n_{703} - n_{1052}}$ where suffixes denote the wavelengths and the relative partial dispersion ($P_{x,y}$) is defined as $P_{x,y} = \frac{n_x - n_y}{n_F - n_C}$. Table 2 shows the dispersion and the temperature coefficient of refractive index for the polymers along with borosilcate crown glass BK-7 for reference[13].

Table 1. Refractive indices of various optical polymers at different wave lengths[13]

OP material	Wavelength (nm)								
	435.8	486.1	587.6	632.8	656.3	703	833	879	1,052
	1	2	3	4	5	6	7	8	9
Principal									
PMMA	1.5025	1.4973	1.4914	1.4892	1.4890	1.4863	1.4839	1.4834	1.4813
PS	1.6171	1.6056	1.5917	1.5872	1.5862	1.5820	1.5767	1.5755	1.5718
PC	1.6117	1.5994	1.5849	1.5802	1.5793	1.5749	1.5695	1.5683	1.5645
SAN	1.5882	1.5783	1.5667	1.5624	1.5623	1.5579	1.5536	1.5527	1.5496
Trademarks									
CTE Richardson	1.6023	1.5927	1.5802	1.5760	1.5750	1.5712	1.5662	1.5651	1.5615
NAS-21	1.5933	1.5835	1.5714	1.5683	1.5674	1.5643	1.5582	1.5566	1.5544
S-low styrene	1.5310	1.5245	1.5162	1.5141	1.5134	1.5119	1.5087	1.5078	1.5055
Optorez 1330	1.5219	1.5163	1.5094	1.5074	1.5065	1.5054	1.5026	1.5017	1.4984
Zeonex E48R	1.5431	1.5376	1.5309	1.5285	1.5282	1.5256	1.5230	1.5225	1.5204
Bayer	1.6121	1.5998	1.5857	1.5815	1.5803	1.5765	1.5711	1.5698	1.5661

Table 2. Dispersion characteristics and of various optical polymers at different wavelengths[13]

Dispersion characteristics	PMMA	PS	PC	Zeonex E48R	Optorez 1330	SAN	BK-7 glass
n_d	1.4914	1.5917	1.5849	1.5309	1.5094	1.5667	1.5168
v_d	59.2	30.5	29.1	56.5	52.5	35.4	64.17
v_{879}	96.7	56.4	54.6	100.5	71.7	66.6	82.3
$P_{435,F}$	0.63	0.59	0.61	0.58	0.57	0.62	0.535
$(\Delta n/\Delta T)_4 \times 10^{-4} \text{ K}^{-1}$ (at 20°C and λ = 435.8 nm)	-1.00	-1.35	-0.60	-1.24	-1.00	-1.10	350

Table 3. Important properties of various optical polymers[13]

Properties	Acrylic (PMMA)	Polycarbonate (PC)	Polystyrene (PS)	Cyclic Olefin Copolymer	Cyclic Olefin Polymer	Ultem 1010 (PEI)
Max Continuous Service Temperature	198°F 92°C	255°F 124°C	180°F 82°C	266°F 130°C	266°F 130°C	338°F 170°C
Water Absorption % (in water, 73°F for 24 hrs)	0.3	0.15	0.2	<0.01	<0.01	0.25
Specific Gravity	1.19	1.20	1.06	1.03	1.01	1.27
Hardness	M97	M70	M90	M89	M89	M109
Haze (%)	1 to 2	1 to 2	2 to 3	1 to 2	1 to 2	-
Coeff of Linear Exp cm X 10-5/cm/°C	6.74	6.6-7.0	6.0-8.0	6.0-7.0	6.0-7.0	4.7-5.6
dN/dT X 10-5/°C	-8.5	-11.8 to -14.3	-12.0	-10.1	-8.0	-
Impact Strength (ft-lb/in) (Izod notch)	0.3-0.5	12-17	0.35	0.5	0.5	0.60
Key Advantages	Scratch Resistance Chemical Resistance High Abbe Low Dispersion	Impact Strength Temperature Resistance	Clarity Lowest Cost	High moisture barrier High Modulus Good Electrical Properties	Low Birefringence Chemical Resistance Completely Amorphous	Impact Resistance Thermal & Chemical Resistance High Index

Table 3 summarizes the important physical properties of optical polymers[14]. With the exception of Ultem (a polyetheramide with n_d = 1.682) most have good transmission between 350 nm and 1600 nm wavelength and are suitable for broadband visible applications. Acrylic and Zeonex have excellent external transmission properties in the visible (around 92%). Polycarbonate and Polystyrene have slightly more haze (with external transmissions of about 87% to 88% in the same region)[14].

Hybrid Glass-Polymer optics

The positive aspects of traditional optical glasses and those of polymers can be conveniently exploited by their combination into what is termed as glass-polymer hybrid optics[8]. Here, a rather thin layer of aspherized optical polymer is added to a conventional spherical glass lens. While glass has a wider range of refractive index and dispersion selectivity, the polymer offers easy aspheic fabrication with lower cost. Thin polymeric portion in the hybrid ensures comparable overall transmissions to lenses made by pure glass multiplets. The optical designs exploit the complementing properties of glass and polymers. For example, glass being non hygroscopic is positioned outside facing the environment so that it protects the inner thin polymer aspheric component. The design allows for a large numerical aperture, a diffraction-limited highly resolved image with wide-field angle, and a compact design with lesser number of optical elements. Additionally, hybrid optics even has a better thermal stability considering the thermal coefficient of refractive index ($\Delta n/\Delta T$), which is the
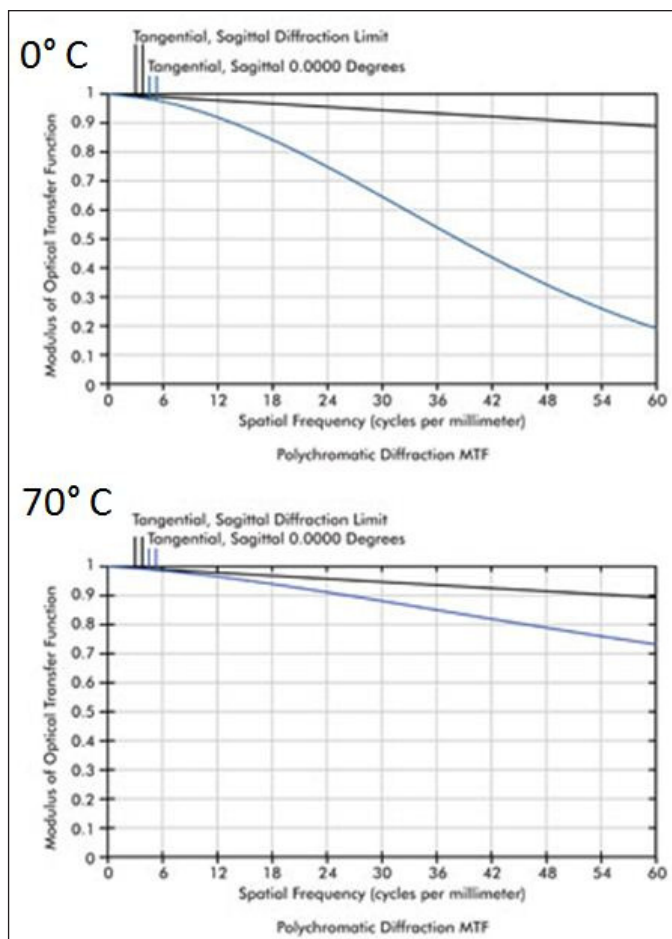

Fig. 7. MTF plots of glass doublet lens at 0°C and 70°C

change in refractive index of the material with temperature. Optical glasses have positive $\Delta n/\Delta T$ whereas optical polymers have negative $\Delta n/\Delta T$, resulting in an enhanced thermal stability of glass polymer hybrid. This effect is illustrated in Figs. 7 and 8 showing the variation in the Modulation Transfer Function (MTF) of doublet lenses for two different temperatures[8]. MTF is a measure of the overall quality of an imaging lens which describes the degradation of the contrast over various spatial frequencies in the object being imaged by the lens. Fig. 7 is the MTF plot for a glass doublet at 0 °C and 70°C showing greater variation as compared to the MTF plots of an equivalent hybrid glass-polymer doublet at the same temperatures (shown in Fig. 8).
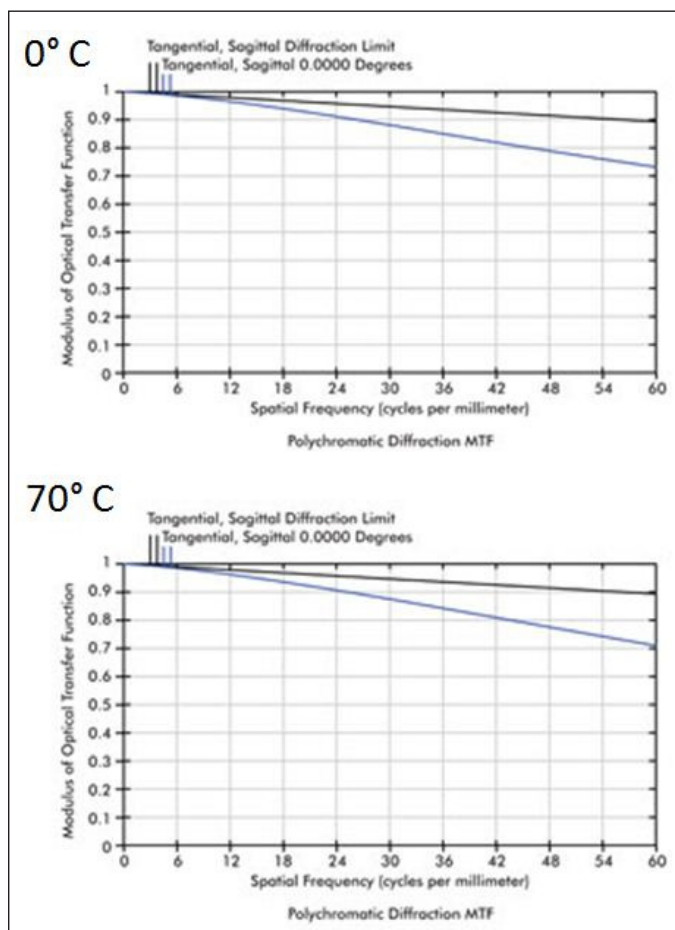
Fig. 8. *MTF plots of glass-polymer hybrid doublet lens at 0°C and 70°C*

Further, the possibility of integrated mounting in the actual manufacturing of the optics allows design freedom, simplified optical alignment, and simplified mechanical design. It also supports easy assembly and packaging, since a system can be assembled and aligned in a single manufacturing step[15].

Component manufacturing process

One of the chief advantages of polymer optics over glass wherever mass manufacturing is concerned is in the cost. Precision plastic optics is fabricated with molding processes that yield high-volume production capability as compared to glass optics. Usual molding methods for optics are injection molding and compression molding[16]. Fig. 9 shows a typical injection molding machine, where pre-dried plastic pellets are put in the hopper and fed into the injection barrel containing a screw. The material is heated to a molten state and injected into the mold. Heat, injection pressure, and injection velocity at various stages in the molding cycle are adjusted to optimize and stabilize the process. The injected material cools and solidifies, taking the shape of the insert cavity. The mold is open and an ejection mechanism separates the optic from the mold. In compression molding, the material is pressed between heated fixed and movable platens, which are temperature-cycled during normal pressing. This type of molding is used primarily used in the manufacture of optical elements requiring high structural details such as Fresnel lenses and lenticular arrays since extremely fine-depth grooves and tight angular tolerances can be achieved with this process. Current technologies in use for molding polymers can manufacture optics with surface roughness of 50 Å using nickel plating on hardened steel inserts[3].
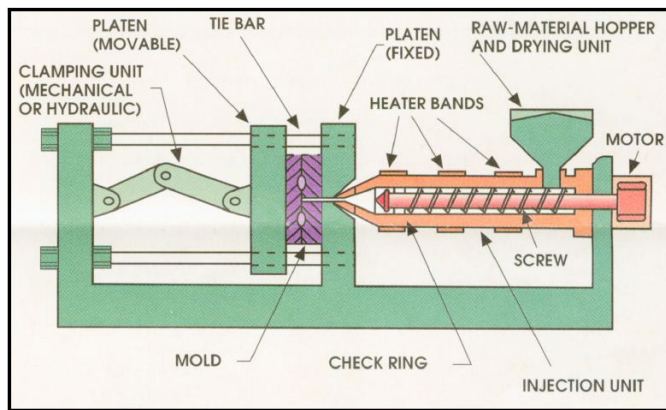

Fig 9. *Schematic of an injection molding machine[16]*

Non linear optical polymers

Polymers have found increasing applications in Non Linear Optical (NLO) devices as active components in the recent years. New developments in polymeric electro-optic modulators has reduced insertion losses to values as low as 5 dB, which is competitive with values obtained for lithium niobate modulators and is much lower than that obtained for gallium arsenide electro-absorptive modulators. Polymeric electro-optic materials are now being evaluated for applications such as phased array radar, satellite and fiber telecommunications, cable television (CATV), optical

gyroscopes, electronic counter measure (ECM) systems, backplane interconnects for high-speed computers, ultrafast (100 Gbit/s) analog-to-digital (A/D) converters, land mine detection, radio frequency (RF) photonics, and spatial light modulators[17].

The non linear optical effect arises out of non linear polarizability of the molecule in response to large electric fields in intense light. The non linear equation describing the macroscopic polarization in the material is expressed as

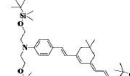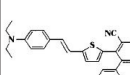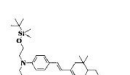$$P = P_0 + \chi_{IJ}^{(1)} E_J + \chi_{IJK}^{(2)} E_J E_K + \chi_{IJKL}^{(3)} E_J E_K E_L + \cdots \quad (1)$$
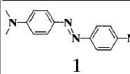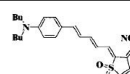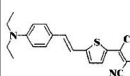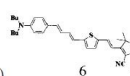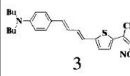
Where P_0 is a static dipole moment and $\chi^{(n)}$ denotes the nth-order susceptibility with *I, J, K, L* subscripts refer to co-ordinate system. Substituting sinusoidal field equation $E(z,t)= E_0 \cos(\omega t\text{-}kz)$ in equation (1), new frequency components originating as non linear effects is shown to be from $\chi^{(2)}$ (second order) and higher orders. Unlike the first and third-order terms there is a symmetry condition for the second-order terms[18]. Specifically, non-centrosymmetric or ascentri-molecular symmetry is required for both molecules and materials in order to realize a nonzero second-order susceptibility. For practical applications, organic second-order NLO materials can be considered to be dipolar molecules organized into non-centrosymmetric chromophore lattices[17].

In polymer-based NLO materials, an NLO chromophore is incorporated into a polymer matrix either as a guest (in a host-guest-system), or as an integral component covalently grafted to polymer chain, or even co-polymerized into the polymer backbone itself. Covalent incorporation in the system can markedly improve stability of the NLO chromophors in applications[19].

The active chromophores in the polymer have to be ordered in a specific direction to get the NLO property either by applying a DC electric field or by specific thin film fabrication methods designed to yield order at the molecular level. The most common methods for generating non-centrosymmetry of dipolar molecules include electric field poling of polymers, utilization of liquid crystalline order, self-assembly, or Langmuir-Blodgett-film formation[18].

Table 4 shows typical guest-host type NLO polymers with their electro-optic coefficients[20] (r_{33}). By using several highly nonlinear molecules such as 5, 6, 7, and 8 shown in Table 4 in polymers, such as PMMA and PC, very large electro-optic coefficients ($r_{33} > 60$ pm V^{-1}, measured at 1.3 µm) is achievable. This is twice the value for lithium niobate (31 pm V^{-1}).

Table 4. Electro-optic coefficients (r33) of some polymers doped with NLO Chromophores[20]

NLO chromophore	$\mu\beta$ (10^{-48} esu) at 1907 nm	$\mu\beta /M_w$	NLO chromophore	$\mu\beta$ (10^{-48} esu) at 1907 nm	$\mu\beta/M_w$
1	580 r_{33} = 13 pm V^{-1} at 1330 nm (30% wt. in PMMA)	2.1	5	13,500 r_{33} = 55 pm V^{-1} at 1330 nm (20% wt. in PC)	27.1
2	6200 r_{33} = 30 pm V^{-1} at 1330 nm (25% wt. in Polyimide)	17.3	6	r_{33} = 65 pm V^{-1} at 1330 nm (20% wt. in PMMA)	
3	9800 r_{33} = 45 pm V^{-1} at 1330 nm (25% wt. in PQ-100)	25.5	7	35,000 r_{33} > 60 pm V^{-1} at 1330 nm (30% wt. in PMMA) V_p = 0.8 V	45.7
4	r_{33} = 36 pm V^{-1} at 1330 nm (25% wt. in PQ-100)		8	r_{33} = 105 pm V^{-1} at 1330 nm (17.5% wt. in PMMA)	

NLO chromophores can also be incorporated by covalent bonding to various polymer backbones in what is termed as side-chain NLO polymers. These types of polymers can provide higher chromophore loading density compared to guest-host systems. They also improve temporal and thermal stability of aligned NLO dipoles. Vinyl polymers like PS and PMMA and high-T_g polymers such as polyurethanes, polyimides, polyamides, polyesters, polyethers, and polyquinolines are being considered for NLO chromophore incorporation[20]. Another type of NLO polymers are the cross linked polymers, where the chromophores are aligned first before linking them to polymer backbone to achieve greater ordering. However, this type of system suffers greater optical losses due to limited cross linked reaction. A relatively new class of macromolecules different from the conventional linear, cross linked, or branched polymers called dendrimers have shown promising potential for NLO polymers. Their regular, well-defined, and highly branched three-dimensional architecture lead to interesting characteristics and physical properties[20].

Polymers in optical fibers

The advances in polymer technologies have also aided rapid developments in fields of fiber optic communication engineering and integrated optical electronics, in which polymers in optical waveguides and optical fibers play a central role. Polymer optical fibers (POF) have certain technical advantages over glass optical fibers such as greater flexibility, mechanical strength, and can be made with larger core diameters (~1 mm) with high resistance to fracture unlike glass fibers. Additionally, POFs have a
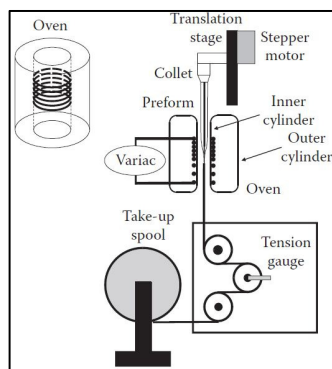
Fig. 10. Schematic of a typical fiber drawing tower[22]

great potential for economic mass production of complex planar photonic circuits and polymer optical fibers due to the availability of a wide range of inexpensive optical polymers and the simplicity of fabricating waveguides from them. The low processing temperature of polymer fibers (200-300°C) allows for introduction of nonlinearity by doping with organic dyes for making active polymer optical fibers such as optical fiber amplifiers and lasers. Optical non linearity in POF can be made much higher than silica glass fibers. The main drawbacks in plastic optical fibers are their dimensional instability and high optical attenuation losses limiting their applications to short range data lines.

POF cores are generally made of optical grade polymers of PMMA, PS and PC while the cladding is of fluorinated or perflurinated polymers. The optical fibers can be fabricated by extrusion process, which is the most economical method for making polymer optical fiber that is also amenable to high-volume processing[21]. Here the monomer is polymerized in the reaction chamber and extruded by pushing the material through small nozzle for creating the fiber. The polymer may be continuously extruded while being polymerized or may be extruded after full polymerization and heating the polymer in a two step process. The optical fibers can also be made by drawing a preform as is done in glass fibers, allowing fabrication of dye doped core with single mode or multimode fibers and graded index fibers. A typical drawing tower for optical fiber fabrication[22] is shown in Fig. 10.
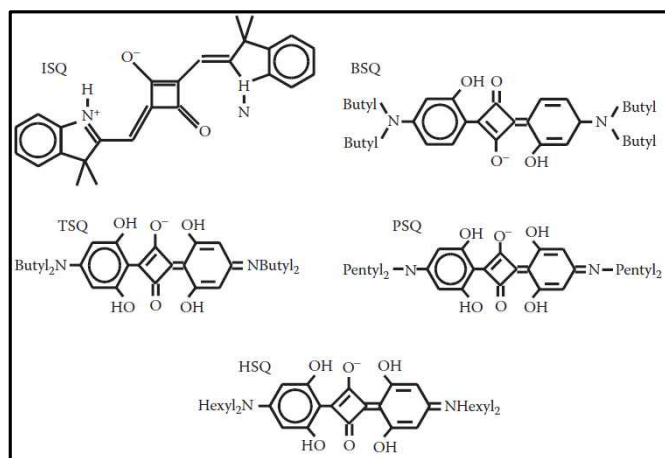

Fig. 11. Typical dye structures used as dopants in POF core[21]

The drawn fibers however tend to suffer from optical birefringence due to polymer chains being stretched during the drawing process and a differential cooling between surface and the inside of the fiber. The flexibility available for doping the fiber core with large number of organic dopants have extended the polymer fibers to diverse applications which are as good as for those with glass fibers and sometimes even better. These include optical fiber-photonic devices, planar waveguides in photonic circuits, fiber sensors, fiber optical amplifiers and lasers. Fig. 11 shows typical structures of the dyes used for doping POF cores[21]

Conclusion

Optical polymer materials have found increasing application in various optical, opto-electronic and photonic devices in the recent times owing to the advancement in polymer technology and many advantageous polymer optical properties complementary to that of optical glass. The growth of polymer optics has also been aided due to economic factors. The vast possibilities in organic polymer structures being investigated by researchers in the field will only aid in their future prospects in optics and photonics, which is definitely set for high growth.

References

1. Menendez, J., Erismann, F., Gauvin, M., "The advantages of plastic optical components" Opt. Photon. News 10, 28–30 (1999)
2. Valerie, C., "Plastic Optics Provide Precision" Photo. Spectra, Dec 2012
3. Tolley, P., "Polymer optics gain respect" Photon. Spectra **10**, 76–79 (2003)
4. http://www.diverseoptics.com/
5. Volker, S., "Polycarbonates" in Ullmann's Encyclopedia of Industrial Chemistry, Wiley-VCH, Weinheim, 2000. doi:10.1002/14356007.a21_207
6. Smith, W. F., Hashemi, J., "Foundations of Materials Science and Engineering" (4th ed.) McGraw-Hill (2006)
7. Maul, J., Frushour, B. G., Kontoff, J. R., Eichenauer, H., Ott, K. H. and Schade, C. "Polystyrene and Styrene Copolymers" in Ullmann's Encyclopedia of Industrial Chemistry Wiley-VCH, Weinheim, (2007) doi:10.1002/14356007.a21_615.pub2
8. Doushkina, V., "Advantages of polymer and hybrid glass-polymer optics. Photon. Spectra" **4**, 54–58 (2010)
9. "Ullmann's Encyclopedia of Industrial Chemistry" Polystyrene and Styrene Copolymers **29**, Wiley Online Library. p. 487
10. Charles A. Harper, ed., "Modern Plastics Handbook", ISBN 0-07-026714-6 (2000)
11. "Cyclo olefin polymer containing intermediate transfer members", US Patent no. US 20110244249 A1
12. http://www.zeonex.com/press/ZeonexK26R.asp

13. Sultanova, N. G., · Kasarova, S. N. , Nikolov, I. D., "Characterization of optical properties of optical polymers" Opt Quant Electron 45:221–232 (2013), doi: 10.1007/s11082-012-9616-6

14. Beich., W. S., "Injection Molded Polymer Optics In The 21st-Century" Proc. of SPIE Vol. 5865, (2005), doi: 10.1117/12.626616

15. Doushkina, V. and Fleming, E.,. "Optical and mechanical design advantages using polymer optics" Proc SPIE, Vol. 7424, 74240Q (2009)

16. Tribastone, C., and Peck, W., "An Introduction to the Design, Manufacture and Application of Plastic Optics.", http://www.apollooptical.com/ content/ docs/ photonics_article.pdf

17. Dalton, L., "Nonlinear Optical Polymeric Materials:From Chromophore Design to Commercial Applications" in Advances in polymer science **158,** ed. Lee., K. S., Springer, (2002)

18. Cho., M J., *et al*, "Recent progress in second-order nonlinear optical polymers and dendrimers" Progress in Polymer Science, **33**, 1013–1058(2008)

19. Prasad, P.; Williams, D. Introduction to Nonlinear Optical Effects in Molecules & Polymers, Jon Wiley & Sons (1991)

20. Kajzar, F., Lee, K., S., Jen, A. K, "Polymeric Materials and their Orientation Techniques for Second-Order Nonlinear Optics" in Advances in polymer science **161**, ed. Lee., K. S., Springer ISBN: 3-540-43157-8 (2002)

21. Kuzyk, M.G., "Polymer Fiber Optics Materials, Physics, and Applications" CRC Press, USA, ISBN 1-57444-706-8 (2007)

22. D. W. Garvey, D.W., et al, "Single-Mode Nonlinear- Optical Polymer Fibers," J. Opt. Soc. Am. B 13, 2017–23 (1996)

Dr. Dinesh V Udupa completed his M Sc in physics at IIT Bombay in 1992 and M. Tech in Applied optics at IIT Delhi in 1993. He joined the first batch OCEP (Orientation Course for Engineering Post-graduates) course of the Training School of Bhabha Atomic Research Centre (BARC). After the completion of the training, he joined Spectroscopy Division of BARC and has been working in the field of Optical design, instrumentation, optical testing, optical interferometry and laser holography primarily for spectroscopic research and analytical applications. He got his PhD in Physics from University of Mumbai with the thesis entitled "Techniques in refractive index measurement and the testing of optical components". He has designed and developed several spectroscopic instruments such as Czerny -Turner monochromators, 22 channel polychromator, Micro-Raman spectrograph, 6.65 meter Vacuum ultraviolet scanning spectrometer for synchrotron beamline and 0.25 m echelle spectrograph for spectroscopic applications. He has also designed and developed a 6 meter optical periscope for visual inspection in the core of the nuclear Fast Breeder Test Reactor, Kalpakkam and a 10 m optical periscope for the Prototype Fast Breeder Reactor. He was conferred the "Scientific and Technical Excellence Award" for the year 2009 by the Department of Atomic Energy for his special contributions to the R&D program of the Department. He is a fellow member of the Optical society of India and is presently leading the Optics & Analytical Spectroscopy Section of the Atomic & Molecular Division, BARC.

Studies on Organic Photonic Materials

Mukesh P. Joshi, S. Raj Mohan and T. S. Dhami
Organic Photonic Materials Laboratory, Laser Materials Processing Division,
Raja Ramanna Centre for Advanced Technology (RRCAT), Indore 452013
Email: mukesh@rrcat.gov.in

Abstract

Thin films and nanostructures of pi-conjugated semiconducting organic materials are used extensively as photoactive component in wide range of photonic device applications such as OLEDs, solar cells, nonlinear optical devices etc. We provide basic description of organic materials with respect to the origin of semiconducting nature of these materials and related optical and charge transport properties. Some examples of studies made using organic materials and with blends of organic and inorganic materials in photonics are presented.

Introduction:

Thin films and nanostructures of organic semiconductors (small molecule dyes are polymers) are used extensively as photoactive materials in developing variety of photonic components and devices. Organic semiconductors are essentially a class of carbon based molecular solidshaving properties similar to that of conventional inorganic semiconductorssuch as low energy electronic excitationsand tuning of bulk electrical conductivity upon doping[1-3].The origin of semiconducting propertiesof these special class of organic solids are essentially due to the conjugation of π-electrons in the molecular structurei.e. the presence of alternate carbon-carbon double and single bonds in theirstructure. Each carbon atom in these materials is in sp^2+ p$_z$ hybridized state. Three sp^2 hybridized orbitals form three strong covalent sigma bonds with neighboring atoms giving mechanical strength to molecular structure. The remaining p$_z$orbitals of each carbon atom, which lie perpendicular to the plane of sigma bonds, form additional weak bonds with neighboring p$_z$ orbitals known as π bonds. The presence of alternate carbon-carbon single and double bonds is known as π conjugation and organic compounds with π conjugation in their structure are known as π conjugated organic materials. Due to weak nature of π bonds the electrons forming π bonds (π electrons) remain delocalized over the backbone of the molecular structure and are essentially responsible for semiconducting and conducting nature in these materials.As shown in Figure 1.1(a), the interaction of delocalized π electrons leads to splitting of initially degenerate 2p$_z$ energy levels and the formation of energy gap between the highest occupied molecular orbital (HOMO) and lowest unoccupied molecular orbital (LUMO) [1-3]. The energy gap of HOMO and LUMO in most of π-conjugated organic materials are ~1-3 eV and also the absolute energies of these orbitals are such that they are either good acceptors of electrons (with high electron affinity) or good donor of electrons (with low ionization potential). For these reasons the thin films and crystals of most of π-conjugated organic materials possess reasonably high cross sections of light absorption/emission in uv-visible spectral range and also offer tunable conductivity upon doping. Apart from this, compared to inorganic counterpart, organic semiconductors offer several other advantages. Film fabrication methodology like spin casting, thermal evaporation etc.are relatively simple and allowcost effective large area film deposition for commercial device applications. Also, withthe advances in chemical synthesis routes, the properties of organic semiconductors such as band gap, solubility in solvents, extension
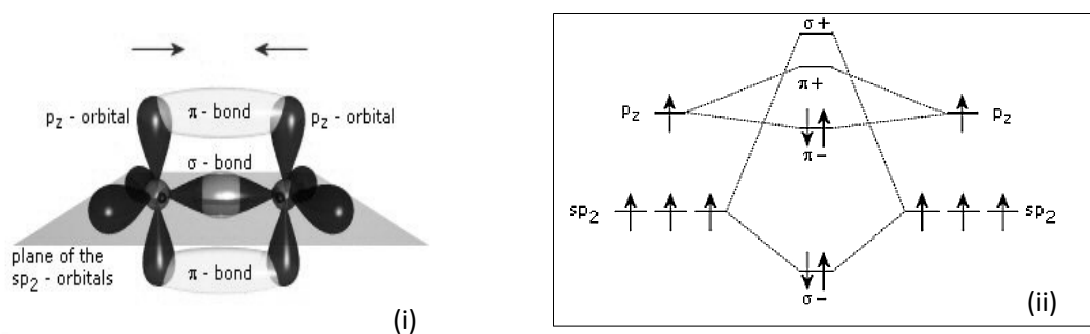

Figure 1.1(a).(i) Schematic of the orbitals and bonds in sp^2+p$_z$ hybridized carbon atom.
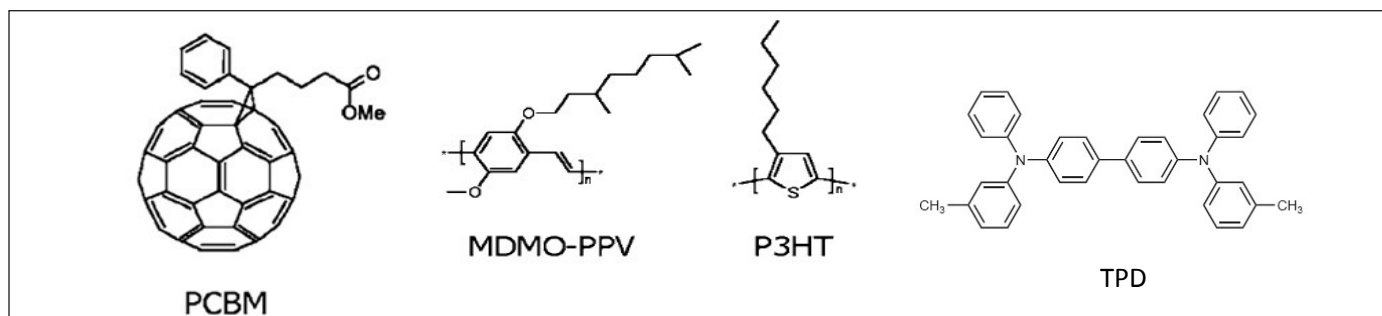*(ii) Splitting of p$_z$ orbital leading to formation of HOMO and LUMO levels.*

Figure 1.1(b). Structures of widely used organic materials in photonics,(i)PCBM ([6,6]-phenyl C61-butyric acid methyl ester),(ii) MDMO-PPV (poly[2-methoxy-5-(3,7-dimethyloctyloxy)]-1,4 (phenylenevinylene),(iii) P3HT (poly(3-hexylthiophene-2,5-diyl)), (iv) TPD (N,N'-diphenyl-N,N'-bis (3-methylphenyl)-[1.1'-bi-phenyl]-4, 4' diamine).

of π-conjugation etc.can be tailored by altering its chemical structure or byattaching variety of side groups.In addition, organic:inorganic hybrid optical materials fabricated bycoupling or blending molecular or polymer units with inorganics (e.g. nanoparticles of semiconductors) further broadens the choice of novel materials and application area[4]. Typical examples of π-conjugated molecules and polymers used extensively in devices such as lasers, organic light emitting diodes (OLED), organic solar cells, organic-field effect transistors (OFET), nonlinear optics, bio-sensors etc. are shown in Figure 1.1(b).

Unlike in the covalently bonded inorganic semiconductors,the intermolecular force of attraction in organic semiconductors isweak due to Van der Waals dipole-dipole interaction. The weak intermolecular forcetogether with the structural disorder (particularly with amorphous polymers films) results in localized electron states. As a consequence, these materials have low dielectric constant, high binding energy for excitons, and low carrier mobility due to hopping nature of

charge transport from one localized state to another [5]. In chemical terms, transport is a redox process (oxidation/reduction) between two molecules. Schematic representation of hopping of charge carrier (e.g. hole) among localized states is shown in Figure 1.2. Therefore for optoelectronic and NLO device applications the light absorption, emission properties, nonlinear susceptibilities etc. of these materials are quite strong but due to low mobility the charge transport efficiency is low. Research directions with these materials are therefore related not only with the search of new materials or processing methodology but more on the understanding structure-property relationship with respect to optical response, transport of charge carriers, degradation under device operation conditions etc. We provide brief account of recent research findings with organic optical materials in the areas of Photovoltaics,OLEDs and nonlinear optical applications.

Influence of casting solvent on polymer film morphology and charge transport:

Conjugated polymer based bulk heterojunctionphotovoltaic cells has gained immense importance because of the potential of chemically tailoring their properties and the availability of cost effective technology developed for various polymer thin film applications. One of the important factors that determine the efficiency of photovoltaic cell is the charge collection efficiency (carrier mobility) and that depend,in a subtle manner, on the film morphology.Film morphology here refers to nano/microscale regions of aggregation or crystallization of polymer chains (or dopants) distributed randomly within the bulk. To understand charge transport in disordered systems,where site energies and inter-site distances of hopping sites follow a certain distribution,the Gaussian Disorder Model (GDM) is widely used[5,6]. According to GDM, carrier mobility is high when energetic and positional disorder in the polymer film is low. These parameters depend largely on the film morphology.
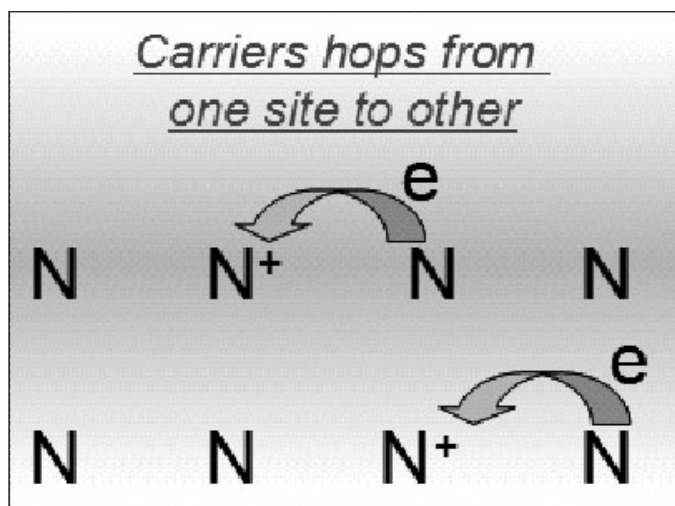

Figure 1.2. Schematic of Redox reaction based hopping transport of holes in molecular solids. N and N+ represent molecules in neutral and oxidized (cation) state.
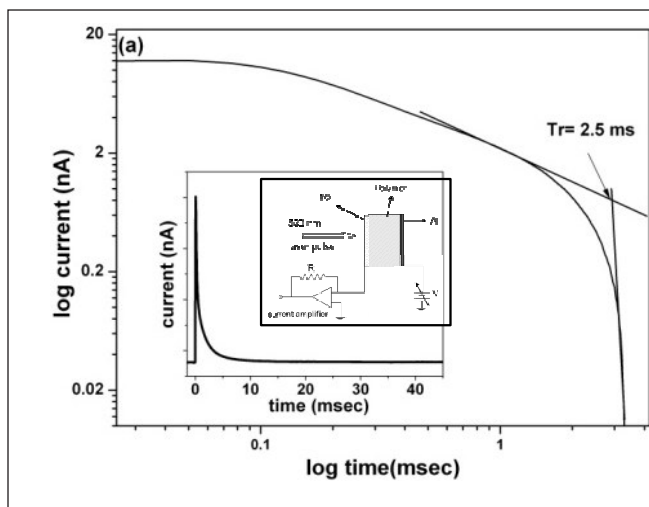
Figure2(a). Double logarithmic representation of photocurrent pulse recorded for CB-TF at Electric field = ~2.4x105V/cm, T= ~300K. Inset shows the photocurrent in linear scale and schematic of current pulse measurement.
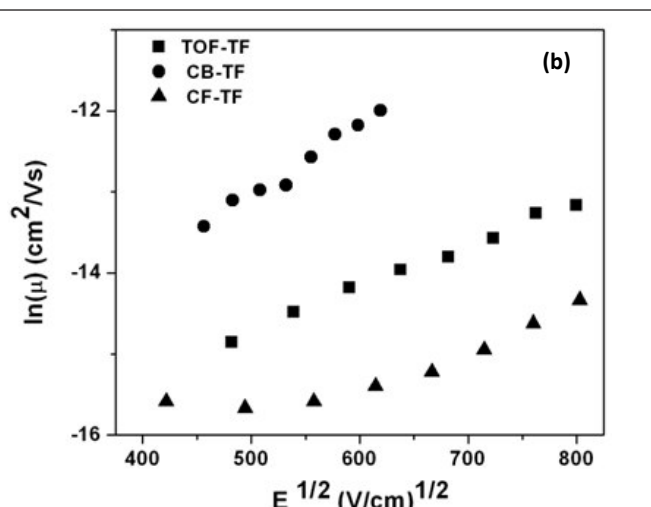
Figure 2(b). Field dependence of mobility in CF-TF, TOL-TF and CB-TF.

Morphology of spin casted filmse.g., depends on various factors like deposition method, deposition parameters, solvent used etc. Choice of casting solvent used is one such parameter that strongly influence the film morphology because of the various conformations, orientations etc. taken up by the polymers chain in different solvents.

We investigatedthe field dependence of charge carrier mobility in thin films of Poly (2-methoxy-5-(3',7'-dimethyloctyloxy)-1,4-phenylenevinylene) (MDMO PPV) casted using either Chlorobenzene (CB), Chloroform (CF) or Toluene (TOL) as casting solvent[7]. These films are named as CB-TF, CF-TF and TOL-TF respectively. Mobility was measured using the time-of-flight (TOF) transient photoconductivity measurement method[6]. Figure 2(a) shows the typical TOF transient photocurrent pulses obtained from CB-TF. Transit time, $T_r$across the sample thickness is obtained from the double logarithmic plot (as shown in Fig 2(a)) and the mobility is calculated using $\mu = L^2/(VT_r)$, where L is the film thickness and V is the applied voltage. Figure 2(b) shows the field dependence of mobility in CB-TF, CF-TF and TOL-TF respectively. In all samples, mobility increases with applied electric field in ln (μ) vs $E^{1/2}$fashion as predicted by GDM [6]. Compared to CF-TF, mobility in CB-TF is at least one order higher while mobility in TOL-TF is higher only by a factor of two.

To gain insight into the relationship of observed mobility values with casting solvents used, we made investigations on the nature of intermolecular or interchain interactions of polymer using photoluminescence (PL) and Raman spectroscopy[7]. PL spectra, shown in Fig 3, shows two major peaks and assigned as 0-0 and 0-1

phonon-assisted transitions. Two main observations are the relative change in the intensity of the 0-0 and 0-1 PL peaks and the shift in PL peak positions among the three spectra. Huang-Rhys (HR) factor, that indicate the strength of electron-phonon coupling[8], are tabulated in the inset of Figure 3. HR factor is highest in CB-TF and least in CF-TF while for TOL-TF is intermediate. This suggests that stronger interchain interaction is present in CB-TF than TOL-TF while the CF-TF possesses the least. Stronger interchain interaction can result in high probability for carrier hopping and thus higher carrier mobility. Another observation from Fig 3 is the shift of PL peaks with three
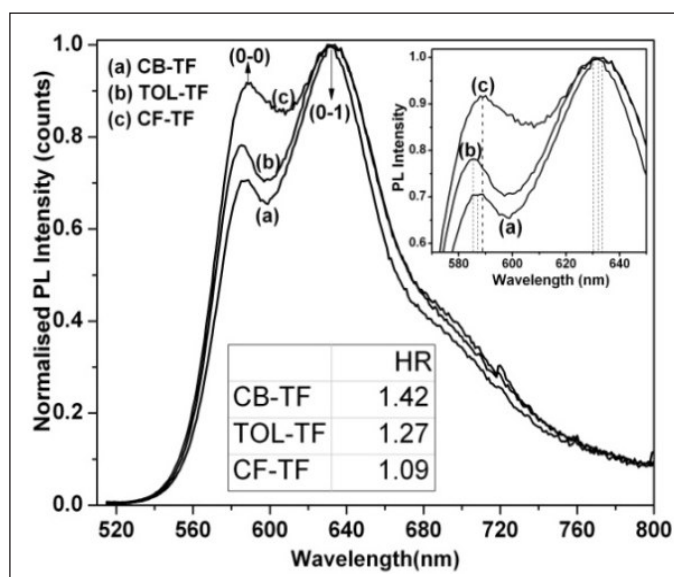

Figure 3. PL spectra of MDMO PPV thin films. Table shows the value of HR factor in each case. Inset shows PL peak shift.
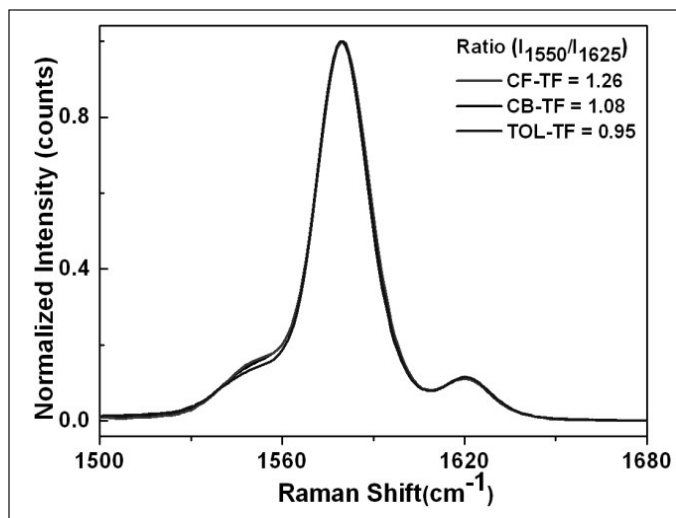
Figure 4. Raman Spectra of MDMO PPV drop casted from various solvents (a) variation in peak intensities at ~1557cm^{-1} and 1625cm^{-1}.

solvents used. It is observed that, with reference to PL of CB-TF, the PL of TOL-TF is blue-shifted while that of CF-TF is red-shifted. This suggests that conjugation length of MDMO PPV is higher in CF-TF and least in TOL-TF, while CB-TF shows intermediate conjugation length. The change in MDMO PPV conjugation length can be attributed to different degree of coiling of chains with solvents used. Thus, we infer that the presence of short conjugation length in TOL-TF is due to the tight coiling of the polymer chains and that results in smaller polymer aggregates in TOL-TF than in CB-TF. In CF-TF the polymer chain may not be tightly coiled as compared to the other two, which can result in large conjugation length. These inferences obtained from PL spectra are also supported by Raman spectra of respective films, as shown in figure 4. The intensity ratio of Raman modes at 1150 cm^{-1}(stretching of vinylene group) and 1625 cm^{-1} (stretching

of phenylene group) correlates with the changes in the conjugation length [8]. Intensity ratios also suggests that the conjugation length is higher in CF-TF and least in TOL-TF with CB-TF possessing an intermediate value. Similarly, the variation in the intensity of out of plane wag of C-H group of vinylene (~963cm^{-1}) suggested that tight coiling of polymer chain occurs in TOL-TF than in CB-TF and least in CF-TF [7]. Hence smaller polymer aggregates are expected in TOL-TF than in CB-TF while in CF-TF polymer chain may be loosely coiled. Smaller aggregates spread throughout film thickness can result in larger fluctuation of hopping distances, which results in large positional disorder and accordingly variation in the mobility. In conclusion, a careful choice of solvent for film casting is important to achieve optimum film morphology for improving charge transport properties in the conjugated polymer thin films.

Enhanced optoelectronic properties of photodegradedaromatic diamine dye:

Thin films of blue light emitting and electron donor aromatic diamine dye, N,N'-diphenyl-N,N'-bis(3-methylphenyl)-1, 1-biphenyl-4.4 diamine (TPD), are used extensively in developing organic display devices as hole transporting layer and also as gain media in solid-state dye lasers[9-10]. Photoinduced doping of TPD was shown when solution of TPD with halomethanewas exposed to UV-light[11].It generates TPD radical cations that not only assist in reducing the injection barrier across metal-polymer interface but also improve bulk conductivity of TPD film. As a continued effort toward understanding the effects of UV light on optical properties, the changes in emission properties of TPD were investigated [12]. It was observed that as UV exposure is continued, there is gradual decrease of TPD radical cations and quenching of blue emission intensity of TPD. Upon prolonged exposure,
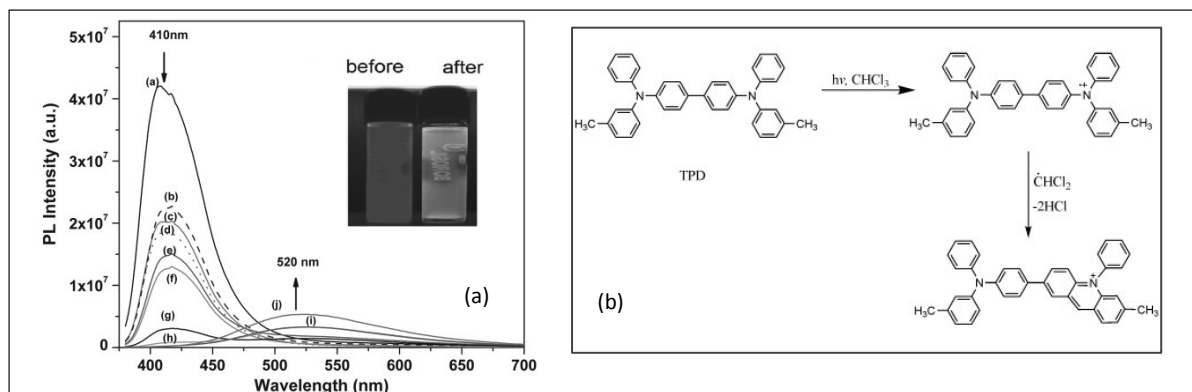

Figure 5. (a) Changes in photoluminescence spectrum of TPD-chloroform solution with UV exposure taken at different exposure durations (a) 0 s, (b) 10s, (c) 30s, (d) 1.5m, (e) 3.5 m, (f) 8.5m, (g) 18.5m, (h) 38.5m, (i) 68.5m, (j) 113.5m. All the data recorded with excitation wavelength at 365 nm. Inset photograph show emission color change before and after prolonged UV exposure (~24 hrs). (b) Possible transformation reaction scheme of TPD to acridine-based dye.
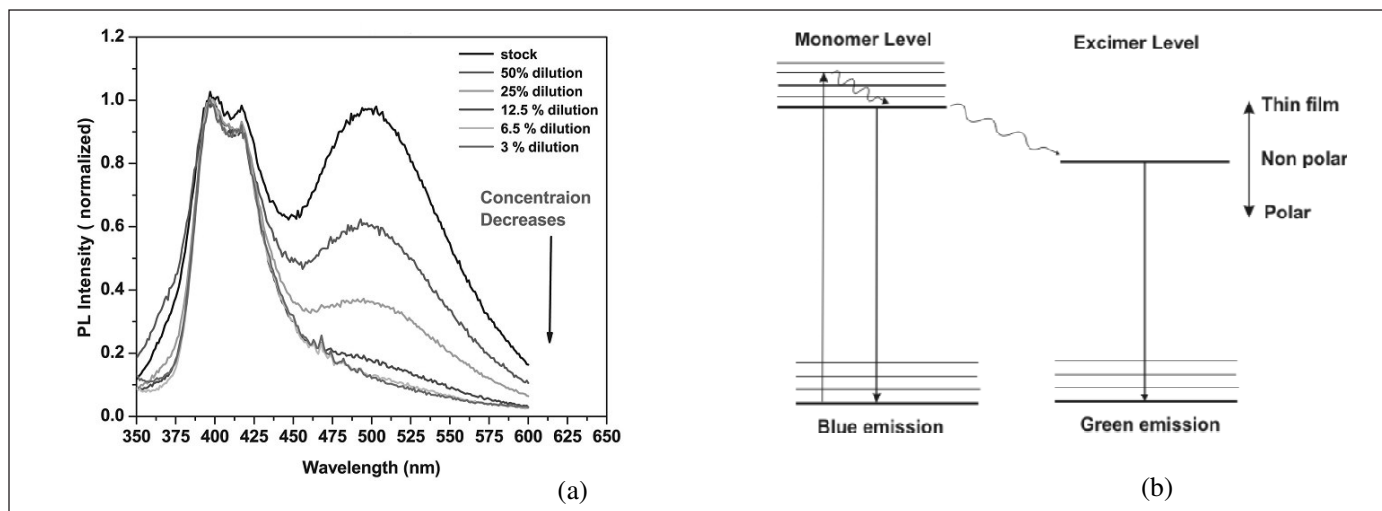
Figure 6.(a) Concentration dependent PL emission from photoproduct dissolved in dioxanesolvent. With decreasing concentration the intensity of green band decreases without any appreciable red-shift. (b) Proposed excimer energy level transitions involved in blue-green dual band PL emission from photoproducts.

the photodegraded TPD showed strong red-shifted broad-band emission in green spectral region(Fig 5(a)). To understand possible origin of green emission, we analyzed the photoproduct and made solvent and concentration dependent emission studies.

Based on detailed analysis of the photoproduct using FTIR and X-ray photoelectron spectroscopy (XPS), it was concluded that UV-induced photolysis of halomethane leads to multicomponent degradation of TPD with acridine salt as major photoproduct[12]. Schematic of possible degradation route of TPD is shown in Figure 5(b).When photoproduct was dissolved in solvents of varying polarity, we observed dual band emission in blue-green spectral region with varying relative intensity of two bands[12]. In addition, the PL decay life times of blue and green bands were different (in general, $\tau_{blue} < \tau_{green}$) and green band lifetime varied strongly with the solvent. These studies suggested that the origins of two bands are interrelated and could be of intra- or intermolecular in nature. To isolate intra- vs. intermolecular origin, we carried out concentration dependent experiment. Figure 6 (a) show concentration dependent emission from dioxane solution of photoproduct. Upon dilution (with decreasing conc.) the emission intensity of green band decreased strongly with respect to that of blue band. These emission characteristics of photoproduct suggested that emission in blue was due to locally excited transitions from monomer of acridine based photoproduct while green band was due to intermolecular excimer/aggregate emission from acridine based photoproduct. A suitable model/scheme based on excimer emission was proposed(as shown in Figure 6(b)) to explain the origin of dual band emission

The film of photoproduct also showed substantial improvement in electrical conductivity compared to film of parent compound TPD[12]. Therefore the technique of UV light exposure based photochemical transformations of molecular materials with enhanced optoelectronic properties may be considered as novel means of processing of molecular materials for various device applications.

Nonlinear Optical Properties of Donor-Acceptor-Donor Y-Type π–Conjugated Polymer:

Nonlinear optical response of π-conjugated organic polymers are exploited in developing intensity modulator, harmonic generation etc[13]. For large nonlinearity various chromophore systems have been designed and investigated, which are primarily of extended π-conjugation and based on suitably linked donor/acceptor groups. In that respect, for second order NLO applications, dipolar or multipolar molecules with multiple donor/acceptor arrangements such as X-, V- and Y-shaped chromophores have attracted a great deal of attention [14]. Another requirement, for second order optical response, is the lack of inversion symmetry at macroscopic level. Since most of the as prepared polymer thin films are amorphous with random orientation of chromophore dipoles. Corona poling is widely used technique to induce or align dipoles in a particular direction to obtain poled polymers with non-zero second order nonlinearity. One of the challenging issues in the performance of poled polymer system is the stability of aligned dipoles after poling. It has been observed that with aging or with temperature rise the directionality of oriented dipoles is lost leading to poor NLO response. In this context, to maintain orientation of NLO chromophores, polymer with Y-shaped chromophore
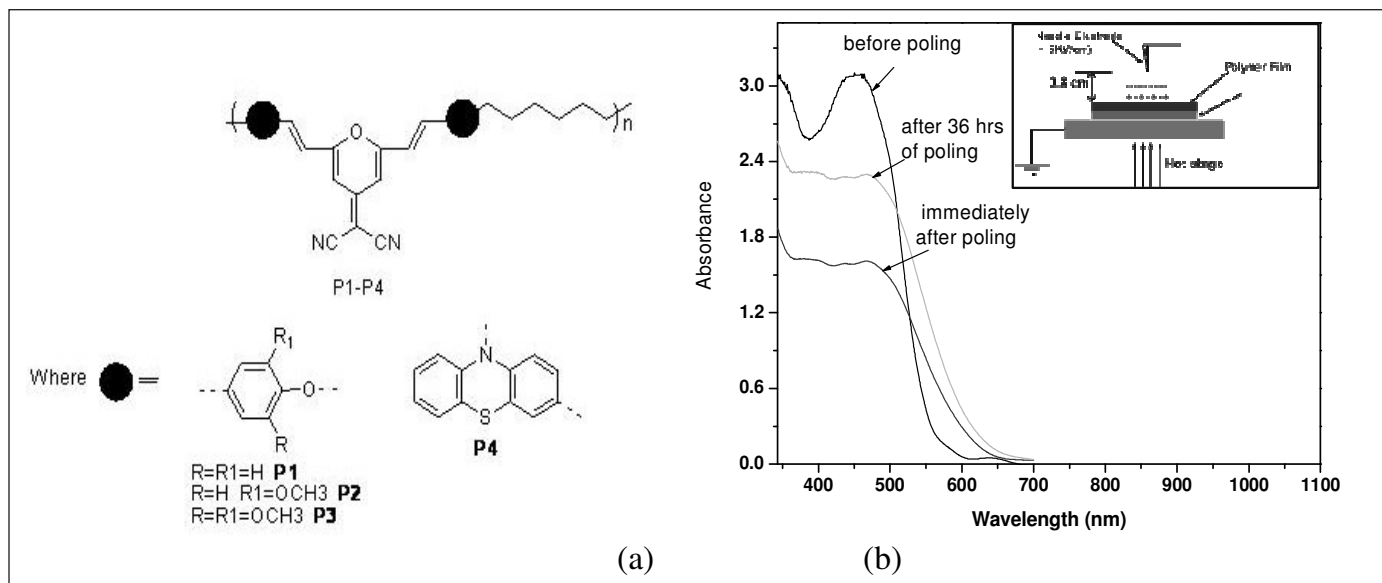
Figure 7: (a) Basic structure of Y-shape polymer with different side groups (P1-P4). (b) Typical absorption spectrum of polymer P4 before and after poling. Inset picture shows the schematic of poling process.

is considered to be of advantage. It not only provides large nonlinearity but, due to structural rigidity, it is thermally stable (T_g) up to 160^{0}C. We characterized second harmonic generation (SHG) properties of four different Y-type polymers [15-17].These polymers are based on donor-acceptor-donor type repeating unit having different aromatic moieties acting as donors. Structures of four polymers are shown in Figure 7(a). The donor group is directly linked to the polymer backbone at both the ends and the acceptor dicyanomethylene group is attached to pyran ring. The donor is varied from different substituted benzenes to phenothiazine. We studied the influence of four different side groups attached to polymer backbone on the stability of SHG intensity of poled polymer with temperature and time. For SHG measurements we used Q-switched Nd:YAG laser pulses (1064 nm, 5 ns, 10 Hz rep rate). For in-situ SHG measurement i.e. while poling process is on, the desired DC field (~ 5KV/cm) was first applied across film thickness and temperature is gradually increased (see inset of Figure 7(b)). Near the T_g, drastic increase in SHG intensity was observed confirming the beginning of dipolar alignment process. Poling process is kept on for 10-15 minutes (till SHG intensity stabilized to its maximum). Temperature is then lowered with field still on. Field is switched off after films are cooled to RT. The degree of dipole orientation of poled polymer films was characterized by measuring order parameter (Φ) of dipole orientation calculated using equation

$$\Phi = 1 - A_1 / A_0$$

where A_0 and A_1 are the absorbance of the polymer film before and after poling respectively. The maximum value

of Φ = 1 corresponds to 100% alignment of dipoles. The absorption data of polymer P4 before and after poling is shown in Figure 7(b). It can be observed from Table 1 that the donor structure has influenced the absorption pattern of the polymer as acceptor remained same. The wavelength of maximum absorbance (λ_{max}) depends on the conjugation length and donor strength. P4 show highest λ_{max} because it has phenothiazine as donor group which is known for maximum donor strength characteristics as compared to other polymers [15]. Similarly, the order parameter also varied strongly with the donor group. For thermal stability studies, we first poled each polymer for sufficient time
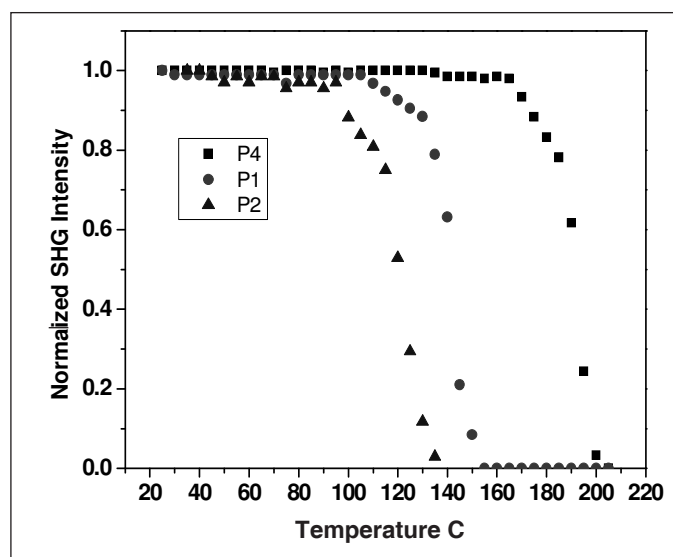

Figure 8: Thermal stability data of poled polymers showing comparison of second harmonic intensity from poled polymers as a function of temperature.

Table 1			
Polymer	λ_{max}(nm)	T_g(^{o}C)	φ
P1	417	172	0.30
P2	340	129	0.20
P3	337	133	0.07
P4	459	212	0.48

to achieve maximum possible SHG intensity. All poled polymer samples were kept at room temperature for more than a week and then loaded back on to the heating stage for SHG measurement again. Figure 8 shows the dynamic thermal stability of polymer P1, P2 and P4. It can be seen that SHG intensity of P2 is stable up to 100^{0}C whereas P1 is stable up to 110^{0}C.

When the donor substituent changed to hetero aromatic moiety containing polymer (P4), the SHG intensity was observed to be highest and remained stable up to almost 165 ^{0}C. In addition, polymer P4 also showed long term stability [15]. This strong stability of P4 against temperature and time and also large order parameter could be due to high T$_g$ and the nature of phenothiazine as strong donor substituent.

Photovoltaic performance from blend of conjugated polymer and PbS nanoparticles:

Bulk heterojunctions formed by blending of conjugated polymer with nanomaterials, such as fullerenes and inorganic semiconductor nanoparticles, has been found to enhance the performance of polymer based photovoltaic devices [18-20].When polymer is photoexcited it generates excitons, which then migrates to interface of polymer and

nanoparticles. Due to favorable type-II alignment of energy levels of the two materials system, electrons are transferred from polymer (p-type semiconductor) to nanoparticles (n-type semiconductors) thereby dissociating excitons into free charges.The signature of efficient dissociation of excitons is seen as decreased radiative recombination (the quenching of polymer luminescence) and increase in the photocurrent.Apart from the desired type II alignment of energy levels, the efficiency of charge transfer process also depends largely on the physical separation between the polymer chain and nanoparticles [21]. The insulating nature of ligand or capping molecules, e.g. often used during preparation of colloidal solution of nanoparticles, play an important role in deciding the efficiencies of charge transfer process. To investigate the same, we made comparative study of photoluminescence (PL) quenching and transport properties of blends of Poly[2-methoxy-5-(3',7'-dimethyloctyloxy)-1,4-phenylenevinylene](MDMO-PPV) and lead sulfide (PbS) nanoparticles with respect to the preparation of blends. We processed blends via two different approaches of incorporating PbS nanoparticles in the polymer matrix. The first approach consisted of separately preparing colloid of oleic acid ligand capped PbS nanoparticles and then mix with MDMO-PPV polymer. While in the second approach, PbS nanoparticles were grown in-situ in the polymer solution without any capping agent or ligand[22]. The rationale for in-situ growth approach was to achieve closest possible proximity of nanoparticles and the polymer.

Figure 9(a) shows the PL quenching spectra of composites prepared using two techniques. It is observed that the in-situ grown PbS nanoparticles quench the PL of MDMO-PPV more efficiently than the ligand capped
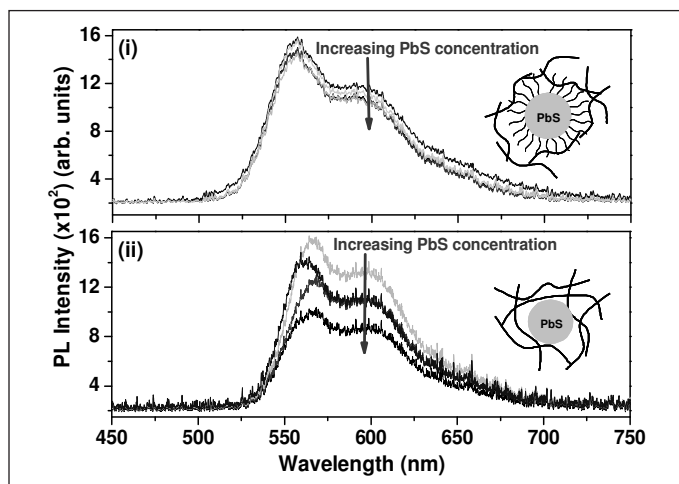

Figure 9(a). PL quenching of MDMO-PPV by (i)oleic acidligand capped and (ii) in-situ grown PbS nanoparticles.
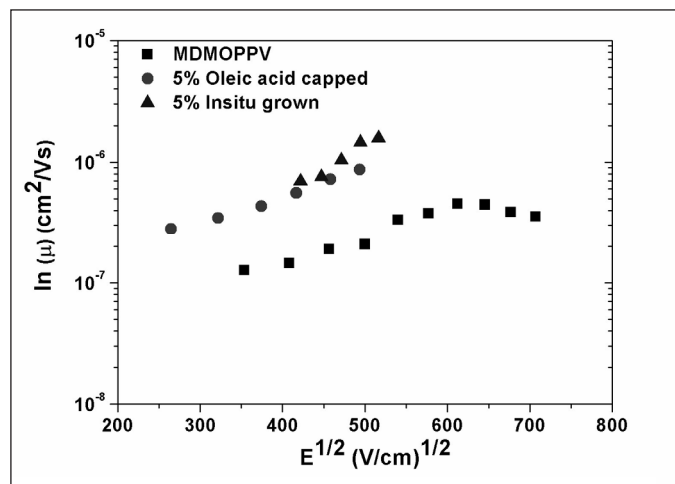

Figure 9(b). Comparison of field dependence of mobility in MDMO-PPV dispersed PbS nanoparticles.

PbS. Further evidence of PL quenching was observed from PL decay lifetime measurement [23].Transient photoconductivity based field dependence of mobility in thin films of both kinds of blend is shown in Figure 9(b). It is observed that for the same concentration of PbS, the composite prepared using in-situ grown approach shows strong quenching of PL and higher hole mobility.

A prototype photovoltaic cell using ligand capped PbS and polymer was fabricated. The device structure was ITO/PEDOT:PSS/polymer composite/Al. The I-V characteristics under dark and white light illumination (output from Xe arc lamp) is shown in Figure 10.
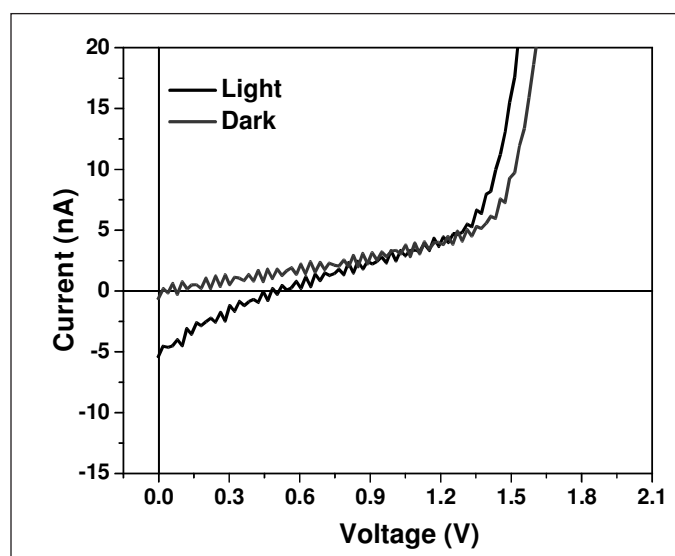

Figure 10. I-V characteristics of ITO/PEDOT:PSS/MDMO-PPV:PbS/Al structure under dark and white light illumination.

It clearly shows increase in photocurrent under illumination. The open-circuit voltage V_{oc} was ~0.5V which matches well with the difference between HOMO of polymer to LUMO of PbS. The short-circuit current I_{sc} was ~5nA. The initial resultof photovoltaic response from the composite was encouraging. Improvement of device performance is expected with further optimization of processing conditions with respect to concentration of PbS in polymer, device structure, fabrication in glove box system etc.

Conclusion:

Above mentioned studies are few representative research based studies where semiconducting organic materials are used as photoactive component in variety of optoelectronic device applications. With the advances in synthesis routes for obtaining molecules or polymers with desired optical/electrical properties and also the film deposition methodology, organic materials have shown great potential as a choice of photoactive material in devices and components at commercial level. These include large area and flexible display, solar cells and other electronic components. For long term device usage and new device applications, focused work in the areas of hybrid composites with inorganics, aging, degradation in ambient etc. demand detailed investigations.

References:

1. G. Hadziioannou, Paul F.van Hutten, *Semiconducting Polymers: Chemistry, Physics and Engineering*, Wiley-VCH :Weinhelm, 2000.

2. R. Farchioni, G.Grosso, *Organic Electronic Materials: Conjugated Polymers and Low Molecular Weight Organic Solids*,Springer:Berlin, 2001.

3. M. Pope, C. E. Swenberg, *Electronic Processes in Organic Crystals and Polymers*, Oxford University Press: New York, 1999.

4. G. Chen, J.Seo, C. Yang and P. N. Prasad, *Chem. Soc. Rev.*, **2013**, 42, 8304.

5. S. Baranovski, *Charge Transport in Disordered Solids with Application in Electronics*, Wiley: England, 2006.

6. H. Bassler, A. Kohler, *Top. Curr. Chem.* 2012, 312, 1; S. Raj Mohan, M. P. Joshi and M. P. Singh, *Org. Electr.*, **2008,** 9, 355.

7. S. Raj Mohan, M. P. Joshi, Shalu C, C. Ghosh, C. Mukharjee, L. M. Kukreja, *J. Polym. Sci., Part B: Polym. Phys.* **2015**, 53, 1431.

8. A. J. Wise, M. R. Precut, A. M. Lapp. J. K. Grey, *ACS Appl. Mater. Interfaces*, 2011, 3, 3011.

9. S. Wang, Y.Q. Liu, X.B. Huang, S.L. Xu, J.R. Gong, X.H. Chen, L. Yi, Y. Xu, G. Yu, L.J. Wan, C.L. Bai, D.B. Zhu,*App. Phys. A*,**2004,** 78, 553.

10. E. M. Calzado, J. Villalvilla, P. G. Boj, J. A. Quintana, M. A. Diaz-Garcia, *Org. Elect.*,**2006**, 7, 319.

11. S. Raj Mohan, M. P. Joshi, S. K. Tiwari, V. K. Dixit, T. S. Dhami,*J. Mater. Chem.*,**2007**,17, 343.

12. M. P. Joshi, S. Raj Mohan, T. S. Dhami, B. Jain, M. K. Singh, H. Ghosh, T. Shripathi, U. P. Deshpande,*Appl. Phys. A*, **2008** 90, 351.

13. S. R. Marder, B. Kippelen, A. K. Jen, and N. Peyghambarian, *Nature*,**1997**, 388, 845; A. M. Sinyukov and L. M. Hayden, *J. Phys. Chem B*, **2004,**108, 8515.

14. S. K. Yeshoda, C. K. S. Pillai and N. Tsutsumi, *Prog. Polym. Sci.*,**2004**, 29, 45.

15. B. Kolli, S. P. Mishra, A. K. Palai, T. Kanai, M. P. Joshi, S. Raj Mohan, T. S. Dhami, L.M. Kukreja, A. B. Samui, *J. Polym. Sci. Part A: Polym. Chem.*, **2013**, 51, 836.

16. B. Kolli, S. P. Mishra, M. P. Joshi, S. Raj Mohan, T. S. Dhami, A. B. Samui, *J. Polym. Sc., Part A: Polym. Chem.*, **2012**, 5, 1572.

17. M. P. Joshi, Raj S. Mohan, Balakrishna Kolli, Sarada P. Mishra, Akshaya K. Palai, Tapan Kanai, T. S. Dhami, L. M. Kukreja, A. B. Samui, *Pramana-J. Phys.*, **2014**, 82, 283.

18. C. Piliego, M. Manca, R. Kroon, M. Yarema, K. Szendrei, Mats R. Andersson, W. Heiss, M. A. Loi, *J. Mater. Chem.*, **2012**, 22, 24411.

19. T. Xu and Q. Qiao, *Energy Environ. Sci.*, **2011**, 4, 2700.

20. P. Reiss, E. Couderc, J. De Girolamoa, A. Pron, *Nanoscale*, **2011**, 3, 446.

21. A. Watt, H. Rubinsztein-Dunlop, P. Meredith, *Materials Letters*, **2005**, 59, 3033.

22. T. S. Dhami, M. P. Joshi, S. Raj Mohan, Pallavi Dubey and L. M. Kukreja, *DAE-BRNS International Symposium on Materials Chemistry(ISMC 2012)*, **2012**, Mumbai.

23. M. P. Joshi, T. S. Dhami, S. Raj Mohan, DAE-BRNS National Laser Symposium(NLS), Indore, **2010**, 90.

	Dr. M. P. Joshi *obtained M. Sc. (Physics) in 1987 from IIT Bombay, Mumbai and joined RRCAT in 1988 after graduating from the 31st batch of the BARC training school. He received Ph. D. degree from IIT Bombay in 2000 for his work on linear and nonlinear optical properties of fullerenes and fullerene based composite materials. He worked for a period of two years at the State University of New York at Buffalo in the area of laser ablation based growth of nanocomposite thin films and polymer photonics. Presently he is involved in R & D of growth methodology and characterization of photonic thin films and nanostructures. Recent research activitiesaredevice application related studies of organic:inorganicnanocompositematerials in photovoltaic, NLO etc.*
	Dr. S. Raj Mohan *obtained M. Sc. (Physics) from CUSAT, Cochin in the year 2001. He accomplished his Ph. D. thesis work at RRCAT in 2007 on optoelectronic properties of organic semiconducting materials. On receiving SITRA Fellowship, he worked at ÅboAkademi, Turku, Finland on characterization of polymer based solar cells. He was awarded Dr. K. S. Krishnan Research Associateship and later joined at RRCAT in 2009 as scientific officer. At present, he is actively involved in research and development of organic materials based optoelectronic devicesand related studies.*
	Dr. T S Dhami *obtained M.Sc. (chemistry) from Kumaun University Nainital in the year 1987. He worked at Central Drug Research Institute (CDRI) Lucknow as JRF, SRF and Research Associate (RA) and received Ph. D. degree in chemistry in 1992. He joined RRCAT in 1993 as a scientific officer. His research interest includes the area of synthetic organic chemistry, organic photonic materials and synthesis of nanomaterials etc. Presently working in organic photonics materials laboratory (OPML), Laser Material Processing division at RRCAT Indore.*

Photonic Crystals of Stimuli-Responsive Microgels

B. V. R. Tata* and R. G. Joshi

Condensed Matter Physics Division, Materials Science Group, Indira Gandhi Center for Atomic Research, Kalpakkam 603 102
*email:tata@igcar.gov.in

Abstract

Under suitable conditions, submicron sized monodisperse colloidal particles suspended in a solvent like water, exhibit crystalline order with lattice constants of the order of wavelength of light and are known popularly as colloidal crystals. Photons propagating through such colloidal crystals experience periodic refractive index variation resulting in stop bands or full photonic band gap depending on the crystal structure and refractive index contrast. Hence colloidal crystals are known as photonic crystals and serve as ideal templates for fabricating photonic band gap structures. Among the various types of colloids (e.g. polymer particles,silica etc.), stimuli responsive microgel colloids are of special interest, as they offer tunability of lattice constant and refractive index contrast as they undergo particle swelling/deswelling upon varying external stimuli such as temperature, pH, ionic strength etc. Apart from reviewing results reported on stimuli-responsive microgel crystals, present article discusses our own results obtained from experimental studies on Poly (N-isopropylacrylamide) (PNIPAM) microgel photonic crystals using light scattering, confocal microscopy and UV-visible spectroscopy techniques. Synthesis of monodisperse stimuli responsive microgels particles and methods for the fabrication of microgel photonic crystals are presented. The tunability of stop band frequencies of dense PNIPAM microgel photonic crystals upon application of osmotic compression and stability of PNIPAM microgel crystals upon variation of temperature are discussed. The article also highlights recent methods employed for fabricating portable PCs through gel immobilization method.

Introduction

Photonic crystals (PCs) are structures composed of two or more materials with different dielectric constants (in other words materials with different refractive indices) arranged periodically in space with lattice constants in the visible range [1]. Such periodic dielectric structures forbid the propagation of electromagnetic waves in a certain frequency range (stop bands). For certain crystal structures and for high values of refractive index contrast, these stop bands overlap leading to complete photonic band gap forming a photonic analogue of electronic semiconductors and are known as photonic band gap(PBG) materials [1-5]. According to variations in the refractive index and periodicity in space, PCs are classified as one-dimensional (1D), two-dimensional (2D) and three-dimensional (3D). PCs have technological relevance as they have been used in the area of optical fibers, photovoltaic devices, Bragg filters, displays, sensors and so on [1, 6-9]. Self-assembly of monodisperse colloidal particles into crystalline order(known popularly as colloidal crystals) has provided cost effective methods for preparing 2D and 3D photonic crystals. The periodic modulation of the refractive index in colloidal crystals gives rise to photonic band gap properties. Colloidal crystals with lattice constants in the visible range exhibit a stop band that manifest as structural colors, similar to natural opals [10]. Several applications such as tunable color displays, iridescent pigments, colorimetric chemical sensors and anticounterfeiting materials[2-3] have been demonstrated based on stop band and structural colors exhibited by colloidal PCs. Several of these applications require techniques for synthesizing monodisperse particles and assembling them into a crystalline state with long-range order.

Colloidal suspensions of hard-sphere as well as charged spheres self-assemble into crystalline order with face centered cubic structure (*fcc*) and their phase behavior has been extensively studied with aim to understand the role of interparticle interactions responsible for different structural orders and to identify stability regimes of the crystalline phase [11-12].
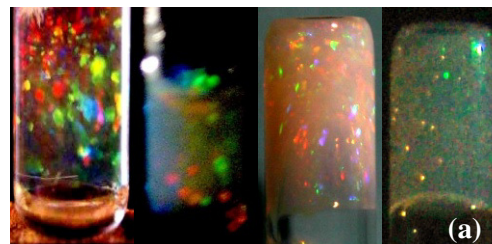

Figure1. Photographs of colloidal photonic crystals showing iridescence under visible light illumination. (a) Charged silica spheres (d =110nm) dispersed in 90:10 ethylene glycol –water mixture, (b) charged polystyrene spheres (d =109nm) dispersed in water. Portable colloidal photonic crystals of charged polystyrene (c) and charged silica (d) particles fabricated by immobilizing the crystalline order in polyacrylamide hydrogel by photopolymerization.

For example poly-methyl methacrylate (PMMA) particles dispersed in Decalin-carbon disulphide mixture is known to freeze into an *fcc* structure at a volume fraction, φ=0.5 and above. Whereas deionized charged polystyrene colloidal suspensions crystallize into a body centered cubic structure (figure 1 (a) and (b))at low volume fractions (φ< 0.2) and into an *fcc* structure at high volume fractions. Deionized suspension of charged silica particles of low charge density, exhibit phase behavior similar to that of polystyrene charged colloids. Photonic crystals based on PMMA, Polystyrene and Silica particles have been extensively studied for their structure, phase behavior and photonic band structure [12-13].
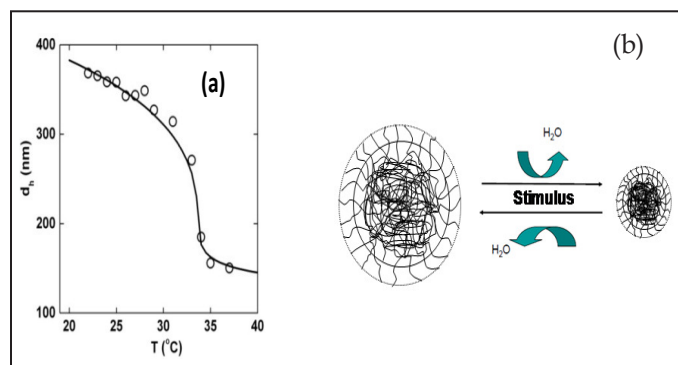

Figure 2. (a) Schematic showing the swelling and deswelling of microgel particles with change in stimulus. (b) Hydrodynamic diameter, d_h of PNIPAM microgel particles measured as a function of temperature using DLS technique. Continuous line is guide to the eye.

The sizes of hard sphere or charged colloidal particles once synthesized are fixed and cannot be altered without changing the concentration of ingredients in the synthesis or synthesis conditions.On the other hand stimuli responsive microgel particles offer size tunability as function of stimuli such as temperature, pH, ionic strength and pressure (shown schematically in figure 2 (a)).PNIPAM microgel particles are thermo-responsive and undergo sudden collapse in size at ~ 34°C which is known as volume phase transition (VPT) [14]. PNIPAM microgels can be functionalized with chemical groups such as acrylic acid to make them pH or ionic strength responsive [15-16]. PNIPAM microgels are also reported to be pressure responsive [18-20]. PNIPAM microgel particles at room temperature are in their swollen state with polymer network content being 2-3% of polymer and rest water [21].Hence the microgel particles in their swollen state are closely index matched with respect to the solvent (water). Upon increasing temperature, the polymer network shrinks due to deswelling resulting in decrease in size of the microgel particle. Beyond VPT, microgel particles will be in their deswollen state with reduced water content and increased refractive index. Hence microgel suspensions beyond VPT appear highly turbid as compared to below VPT. Dense suspensions of monodisperse PNIPAM microgel particles [14,22] as well as charged PNIPAM microgel particles [23], are shown to freeze into crystallize state exhibiting iridescence for the visible light. Since ionic and neutral PNIPAM microgel particles offer tunability in particle size as well as particle refractive index, they are expected to offer tunability in structural color arising due to change in lattice constant and associated photonic band structure. This article focuses on our own results on dense PNIPAM microgel photonic crystals. Effect of temperature and osmotic pressure on the stability against melting and tunability of stop bands of PNIPAM microgel photonic crystals as revealed by systematic shift in Bragg wavelength are discussed. The article also highlights methods for fabricating portable microgel photonic crystals by photo-polymerization process.

Synthesis and characterization of PNIPAM microgel spheres

Free radical precipitation polymerization is commonly used method for the synthesis of PNIPAM based microgels in aqueous medium. Details of synthesis procedure are available in the literature [24-27]. Key ingredients for the synthesis of microgel particles include monomer (N-isopropyl acrylamide - NIPAM), initiator (potassium persulphate - KPS), cross linker (N, N′-methylenebisacrylamide - BIS) and surfactant (sodium dodecyl sulphate - SDS). Synthesis is carried out at temperature of 70°C, by mixing appropriate concentrations of solution of above ingredients, as per the procedure described earlier [24-27]. At this temperature, KPS forms free radicals and initiates the polymerization. BIS cross links the polymer chains and forms polymer network, leading to gel formation. Concentration of BIS decides the number of cross links present in the polymer network, hence the swelling ability of the gel. High amounts of BIS gives rise to large number of cross linking points leading to the reduction in the swelling ability of microgels to the external stimuli. SDS helps in controlling the size of PNIPAM microgel particles. In aqueous medium, SDS forms spherical micelles beyond critical micellar concentration. These micelles as spherical shells contain monomer droplets. Monomer droplets get polymerized to form microgel particles. By varying the SDS concentration, microgels particles ranging in size from 50 nm to ~ 1 μm have been successfully synthesized [14]. Preparations of microgel photonic crystals require microgel particles with very low size polydispersity. The free radical polymerization carried out in one pot, where polymerization is initiated simultaneously within entire

reaction mixture (monomer, cross linker, surfactant), has yielded highly monodisperse particles with size larger than ~ 100 nm. Whereas, microgels synthesized with one pot method having size less than ~100 nm are found to be polydisperse. Brijitta *et al* [27] have developed a novel techniquebatch method for synthesis of monodisperse microgels with size less than 100 nm. Brijitta *et al* [27] divided the reaction mixture in to two parts and added the initiator to one of the part. Once polymer nuclei are formed in one part then they are further grown by controlled drop wise addition of reaction mixture from another part. This has led to the formation of monodisperse microgel particles of size less than ~100nm. PNIPAM microgel can be readily functionalized to make them pH / ionic strength responsive by co-polymerization with ionic co-monomer like acrylic acid [15,23].

Dynamic light scattering (DLS) is a prime tool to study the response of PNIPAM microgel particles to the applied stimuli. In DLS one measures intensity autocorrelation function, $g^{(2)}(q,t)$ which is related to electric field correlation function, $f(q,t)$ as $g^{(2)} = l + |\beta f(q,t)|^2$ with β being geometry dependent coherence factor. In dilute non-interacting suspension of monodisperse particles, $f(q,t)$ decays with single exponential *i.e.* $f(q,t) = exp(-D_o q^2 t)$, Here, q is the scattering wave vector which is related to wavelength of incident light, λ refractive index of solvent, μ_s and scattering angle, θ as $q = (4\pi\mu_s/\lambda) \, sin(\theta/2)$. D_o is the free diffusion coefficient which is related hydrodynamic diameter, d_h of the particle via Stokes-Einstein relation $D_o = k_B T / 3\pi\eta d_h$, where η is the solvent viscosity. Polydisperse particles show deviation from single exponential decay of $f(q,t)$ and are analyzed by cumulant analysis [28] to determine average particle diameter, d_h and size polydispersity. Figure 2(b) shows typical variation of PNIPAM microgel diameter as a function of temperature (*T*) measured using DLS. At 34 °C particles undergo sudden collapse in size, which is identified as VPT. The transition of PNIPAM microgels from swollen state to deswollen state occur due to change of polymer nature from hydrophilic to hydrophobic state. DLS technique has also been employed to study the pH and pressure response of PNIPAM microgels. Mohanty *et al* [23] have studied the pH response of PNIPAM co-acrylic acid microgels, where microgels are found to be in the swollen state at higher pH (> 4.25) and in deswollen state at low pH (< 4.25). At pH > 4.25, carboxylic groups of acrylic acid dissociate giving negative charge to polymer chains. The charge on polymer chains causes electrostatic repulsion between chains leading to the swelling of polymer network. On the other hand, at pH < 4.5, carboxylic groups remains undissociated, hence microgels deswell due to absence of the electrostatic repulsion between polymer chains. Pressure response of PNIPAM microgels have been investigated under application of hydrostatic [19] as well as osmotic pressure [18]. Under both the conditions, PNIPAM microgel particles have been found to deswell beyond a critical pressure.

Fabrication of PNIPAM microgel photonic crystals

Since PNIPAM microgel particles respond to stimuli such as temperature and osmotic pressure by undergoing swelling and deswelling, they can be assembled to crystalline state for tuning the structural color. When functionalized with acrylic acid molecules, they respond to pH and ionic strength in addition to temperature and pressure. Here we discuss our own results on dense PNIPAM microgel suspensions for their phase behavior as a function of temperature tunability of color of dense PNAPAM microgel crystals as a function of osmotic pressure.

PNIPAM microgel particles with low size polydispersity (SPD < 6%) having a mean diameter of 353 nm at 25 °C have been synthesized as per the procedure described above. When concentrated to a volume fraction in the range of 0.5 to 0.6, their suspensions are found to undergo crystallization exhibiting iridescence (structural colors) to the visible light (figure 3(a)). Samples exhibit different colors due to different microgel crystallites with different orientation (sample of incident θ being different for different crystallites) satisfy the different Bragg condition $\lambda_B = 2d\sqrt{n_{eff}^2 - Sin^2\theta}$. [3]. Here, n_{eff} is refractive index of microgel crystal which can be determined by an effective medium approach $n_{eff}^2 = \sum f_i n_i^2$, with f_i and n_i representing the filling fraction of different constituents and their refractive indices, respectively. Apart from the wavelength of the Bragg peak, λ_B the width of the Bragg peak which related to the dielectric contrast (in other words refractive index contrast) and its resolution which is related to the crystallization of the sample, are important quantities that need through investigation for designing good quality opal photonic crystal structures[3]. UV visible spectroscopy [29] and static light scattering are the appropriate techniques for characterizing the structure of opal photonic crystals [11].

In the case of PNIPAM microgel crystals with volume fraction > 0.6, one does not observe the spontaneous crystallization, due to increased volume fraction of the suspension leading to kinetic arrest of PNIPAM microgel particles. The glassy state observed in samples with φ > 0.6 is translated to the crystalline state by repeated annealing of the PNIPAM microgel samples at temperature above VPT. The sudden decrease in the particle size creates space for

particles to rearrange themselves and explore configuration space, getting them structured in to crystalline state upon slow cooling. Figure 3(b) shows iridescence of PNIPAM microgel crystal with volume fraction of 0.8.
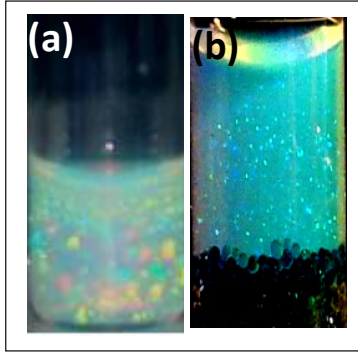

Figure 3. Photographs of colloidal photonic crystals of PNIPAM microgel particles showing iridescence under visible light illumination. (a) Sample with ϕ = 0.5, left undisturbed for 24 hours and (b) sample with ϕ= 0.8, cooled slowly from VPT to room temperature and black region at bottom of the cell is due to the presence of mixed-bed of ion exchange resins.

Techniques for characterizing the structure of colloidal photonic crystals

Since the lattice constants of colloidal photonic crystals are of the order of wavelength of light, static light scattering, confocal laser scanning microscopy and UV-Vis spectroscopy are the appropriate techniques for investigation of their structural ordering.

Confocal laser scanning microscopy

Particles, whose size is above the diffraction limit of light, can be imaged using optical microscope. Unlike an optical microscope, confocal laser scanning microscope (CLSM) employs illuminator pinhole and detector pinhole in confocal geometry. Confocality of pinholes improves the lateral spatial resolution as compared to conventional optical microscope because of the sharpening of the central peak of the Airy disc [30]. Further, detector pinhole rejects the light coming from the off focal points and allows only the light coming from the focal point of the objective lens. This allows optical slicing thereby facilitates imaging inside the sample and hence depth profiling of the sample. Scanning the laser beam in the horizontal (XY) plane allows generation of single optical slice at single Z and then such several optical slices can be generated by moving the objective in Z direction (figure 4 (a) and (b)). Latter by combining the several optical slices, the three dimensional image of the sample can be reconstructed. Brijitta *et al* [31] have successfully employed the CLSM to investigate the structure of PNIPAM microgel crystal having volume

fraction of 0.45. In order to investigate the structure, PNIPAM microgel crystal was imaged in layer by layer manner by moving objective in Z direction and several optical slices are generated. Figure 4(b) and (c) shows the Z stack of CLSM optical slices and 3D image reconstructed using these slices, respectively for PNIPAM microgel crystal. In order to know about stacking of crystalline planes in the microgel crystals, objective was moved by distance of $\sqrt{2/3}d_{nn}$ (d_{nn} – near neighbor separation), which is the inter-planar distance for close packed planes of *fcc* and hexagonally close packed (*hcp*) structures. The near neighbor separation,d_{nn} has been directly measured from single Z slice. The recorded images have been analyzed and used for obtaining the quantities like stacking probability, *a* and pair correlation function *g(r)*. Optical slices have been subjected for image analysis for obtained (X,Y) coordinates in a given Z- slice. Z-stacks of optical slices have been analyzed for their stacking sequence and the stacking disorder is determined[31]. 3D *g(r)* obtained by image analyzing the Z-stacks is shown in figure 4(d) and confirms the structure of annealed PNIPAM microgel crystals to be *fcc*[31].
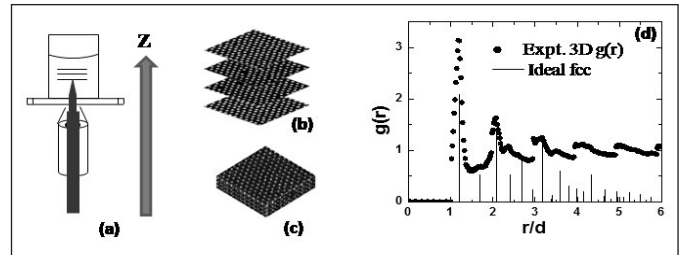

Figure 4: (a) Schematic of confocal laser scanning microscope geometry for imaging the sample in layer by layer manner to generate a Z- stack of optical slices. (b) Z-stack of optical slices from photonic crystals of520nm diameter PNIPAM microgel particles.(c) Reconstructed 3D image using optical slices shown in (b). (d) Experimental 3D g(r) of photonic crystals PNIPAM microgel particles. Vertical lines represent 3D g(r) calculated for an ideal fcc lattice

Static light scattering

Static light scattering (SLS) is the appropriate tool for charactering the structural ordering in less turbid colloidal suspensions of small size (diameter smaller than 300nm) particles. In SLS one measures scattered intensity *I(q)* from colloidal particles, which in Rayleigh-Gans approximation is given by [14],

$$I(q) = AF(q)S(q) \text{(1)},$$

Here, *S(q)* is interparticle structure factor, *P(q)* is particle structure factor and *A* is a constant arising due to Rayleigh scattering given as,

$$A = \frac{16\pi^4 N a^6}{\lambda^4}\left[\frac{\mu_r^2 - 1}{\mu_r^2 + 2}\right]\frac{I_0}{r^2}\,(2).$$

Where I_0 is the incident intensity, r is the distance between sample and the detector, a - particle radius, N - number of scattering particles, μ_r - relative refractive index of the particle with respect to solvent. $P(q)$ of the particle can be measured using SLS on the dilute non-interacting suspensions ($S(q)$ =1), which can be further used to obtain $S(q)$ of ordered suspensions from the measured $I(q)$.

Tata *et al* [11] have reported crystal structure of colloidal photonic crystals of polystyrene to be *bcc* using SLS and showed that crystalline order can coexist with particle free regions (voids) in suspensions of highly charged particles. In the case of highly turbid suspensions exhibiting iridescence, Ultra small angle X-ray scattering (USAXS) technique can be employed to characterize the structure. Petukhov *et al* [32] have used high resolution SAXS technique and, studied the colloidal photonic crystal structure of PMMA, polystyrene and silica spheres. Brijitta *et al* [24] and Joshi *et al* [33] have studied the stability of PNIPAM microgel photonic crystals against melting using SLS and discussed later in this article.

UV-Visible spectroscopy

In a static light scattering experiment one keeps incident wavelength of the laser fixed and sweeps the scattering angle to records different diffraction peaks to analyze the crystal structure of colloidal photonic crystals. UV-Visible spectroscopy offer yet another way of analyzing crystal structure of colloidal photonic crystals where one sweeps the wavelength by keeping the incident angle fixed to record different diffraction peaks. Unlike in conventional UV-Visible spectrometers, Fiber based UV-Visible spectrometers offer advantage of selecting different incident angle to a maximum of 90° [3,34]. UV-Visible spectroscopy can be used to characterize for characterizing the crystal structure of colloidal photonic crystals provided absorption peaks from colloidal particles or solvent does not interfere with the Bragg diffraction peaks or stop bands of photonic crystals [29]. Bragg peaks in the reflection spectra are analyzed for parameters such as Bragg wavelength (λ_B) the full width at the half-maximum (FWHM) and the height of the reflection maximum and the resolution of the reflectance maximum. Diffraction resonances recorded at different angles of observation also provided another important parameter that can be used for characterizing the completeness of the PBG structure [3]. Zhou *et al* [29] have used extensively UV-visible reflection spectra to characterize the crystal structure of charged polystyrene colloidal photonic crystals but also crystallization kinetics [29]. Here we report UV visible studies on dense PNIPAM microgel photonic crystals showing tunability of Bragg diffraction upon osmotic compression.

Temperature response of PNIPAM microgel photonic crystals

Temperature does not play much role in the case of photonic crystals formed using charged polystyrene spheres or PPMA hard-spheres as the inter particle interactions are less sensitive to temperature [11-12]. However colloidal photonic crystals of thermo-responsive microgel spheres are expected to be less stable at elevated temperature as PNIPAM microgel sphere deswell leading disruption of crystalline order. Joshi *et al* [33,35] have studied the temperature response of PNIPAM microgel crystals using SLS. Bragg diffraction peak (Figure 5(a) from PNIPAM microgel photonic crystal has been recorded at room temperature by measuring $I(q)$ vs q using SLS. Upon raising the temperature, the intensity of Bragg peak was found to decrease and turn into a broad peak (figure 5 (b)) 26°C. Sharp Bragg peak tuning into a single broad peak associated with absence of iridescence in the sample suggest melting of PNIPAM microgel crystals. The melting transition temperature was identified by monitoring the Bragg peak intensity as a function of temperature (shown in figure 5(c)). The sudden decrease in Bragg peak intensity at around 26°C indicated the melting temperature beyond which colloidal photonic crystals does not exist. Weissman *et al* [36] have studied temperature response of photonic crystals of PNIPAM microgel particles functionalized with ionic groups (2-acrylamido-2-methyl-1-propanesulfonic acid). It is shown that, crystalline order can be made stable even beyond the VPT of PNIPAM microgel particles by functionalizing PNIPAM particles with ionic groups. UV-visible studies by Weissman *et al* [36] on photonic crystals of ionic PNIPAM microgel show enhanced diffraction efficiency of PNIPAM microgel photonic crystals at temperatures above VPT. Higher diffraction efficiency observed beyond VPT is due to increase in the refractive index contrast coming from collapsed (deswollen) microgels particles [36].

Pressure response of PNIPAM microgel photonic crystals

PINIPAM microgel particles not only undergo deswelling upon increasing the temperature but also undergo compression upon increasing the osmotic pressure applied by addition of non-adsorbing polymer chains such as dextran [18]. Recently Joshi *et al* [20,33,35]
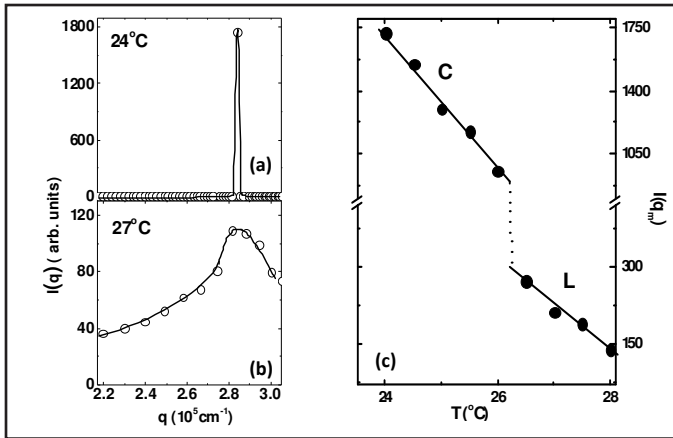
Figure 5. (a) Bragg peak from photonic crystals of PNIPAM microgel particles with φ = 0.8 measured using SLS. (b) I(q) vs qshowing single broad peak at 27°C indicating melting of photonic crystals. (c) Intensity of Bragg peak, I(q$_m$) as a function of temperature. Vertical dotted line at ~26°C indicates melting of photonic crystals (C) into a liquid (L). Continuous lines are guide to the eye.
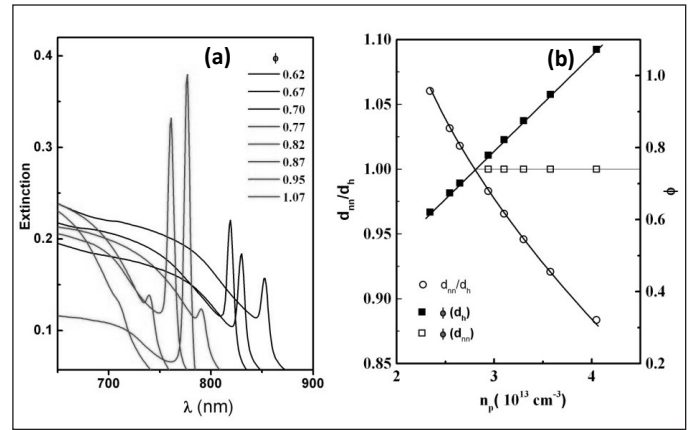

Figure 6.(a) UV-Visible spectra from photonic crystals of PNIPAM microgel particles showing blue shift upon osmotic compression to different values of φ (increasing from right to left). Black and red lines indicate the samples with PNIPAM microgel particles in uncompressed (φ< 0.74) state and compressed φ> 0.74) state, respectively. (b) d$_{nn}$/d$_h$ and φ estimated using d$_h$and d$_{nn}$ as a function of n$_p$. Continuous lines are guides to the eye. All spectra correspond to T = 22°C.

have shown that PNIPAM microgel spheres undergo compression by experiencing the osmotic pressure exerted by its own particles under dense conditions. Such a conclusion has been obtained by subjecting dense PNIPAM microgel photonic crystals to different amounts of osmotic compression and by analyzing systematic shifts in Bragg peaks recorded using UV-visible spectrometer [20,33,35]. Osmotic pressure exerted by microgel particles in a suspension can be varied by changing the number density of microgel particles, n_p and hence the volume fraction, $φ$ of the suspension. Figure 6 (a) shows UV-Visible spectra form PNIPAM microgel crystals recorded as a function of increased volume fraction. The peaks in the UV-Visible spectra are due to the Bragg diffraction of light from PINIPAM microgel photonic crystals. With increase in $φ$, the Bragg peak position, $λ_B$ is found to exhibit a blue shift. Using CLSM, we have shown earlier that dense PNIPAM microgel photonic crystals order into an *fcc* structure [31]. From the knowledge of the structure and using the values of $λ_B$, we could determine the near neighbor separation, d_{nn}, number density of microgel particles n_p and volume fraction $φ$ of PNIPAM microgel photonic crystals subjected to different amounts of osmotic pressure.

Figure 6 (b) shows the variation of near neighbor separation, d_{nn} as a function of osmotic pressure which is proportional to n_p.   Notice that with increase in osmotic pressure, d_{nn} decreases suggesting compression of microgel crystals. For microgel crystals with high n_p, $φ = n_p πd^3/6$ determined with d being microgel diameter (d_h) in the swollen state is found to be higher than 0.74, which is unphysical as maximum packing limit of spheres for an

fcc crystalline order is 0.74. Note that the observed value of d_{nn} for microgel crystals with $φ> 0.74$ is lesser than the microgel particle size in its swollen state (*i.e.* d_{nn}/d_h < 1). This suggests that microgel particle deswell upon osmotic compression in dense colloidal photonic crystals. The $φ$ values estimated using d_{nn} as the particle diameter found to scale to 0.74. This implies that above a volume fraction of 0.74, microgel particles experience osmotic compression and undergo deswelling to a new size such that volume fraction remains at 0.74. The deswelling of PNIPAM microgel particles, upon osmotic compression in a crystalline state is depicted schematically in figure 7. The reason for osmotic compression can be under stood as follows. At $φ ≥ 0.74$, microgel particles experience osmotic pressure greater than the bulk modulus of individual microgel particle [37], hence any increase in $φ$ (osmotic pressure) beyond 0.74 leads to compression of the microgel particle to a new size where the osmotic pressure equals the bulk modulus of the microgel particle. Osmotic compression experiments with the controlled addition of
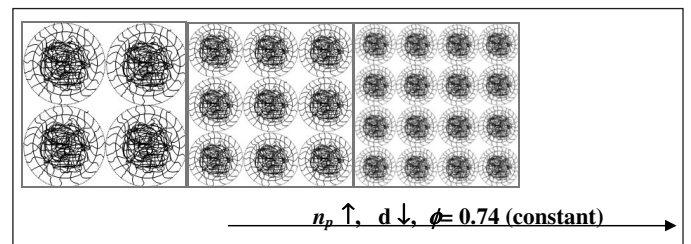

n_p ↑, d ↓, φ= 0.74 (constant)

Figure 7. Schematic representing the deswelling of PNIPAM microgel particles with increasing n$_p$(i.e. increasing osmotic pressure) beyond the volume fraction of 0.74.

non-adsorbing external polymer under dilute condition indeed confirm this explanation. Thus PNIPAM microgel photonic crystals offer tunability of Bragg diffraction (in other words stop bands) with controlled osmotic pressure applied under dense conditions.

Fabrication of portable colloidal photonic crystals

Colloidal photonic crystals are soft and fragile as their elastic constants are extremely small(~ 10-100 dynes/cm^2) [11-12], hence crystalline order gets disrupted easily under extremely small shear, in other words during handling. This limitation can be easily circumvented by immobilizing them in a polymer hydrogel medium. Typical process of gel immobilization involves growing colloidal crystals in a prequel solution consisting of monomer, cross-linker and photo-initiator. Colloidal crystals in the pregel solution are exposed to UV light for polymerization and gel formation. Colloidal crystal immobilization by photo polymerization process using UV light is shown schematically in figure8. Here, photo-initiator helps in carrying out the gelation without physically disturbing the crystalline order. Upon gelation, polymer chains span a network around the microgel particles and thereby fixing the particles close to the original lattice positions. This method of gel immobilization has been widely employed for preparing portable colloidal photonic crystals using charged polystyrene or silica colloidal particles [38,39]. Photographs of gel immobilized photonic crystals of charged polystyrene and silica spheres in water are shown in figure 1 (c) and (d), respectively. The same method has also been successfully applied for immobilizing photonic crystals of charged microgels [40-41]. Immobilization of microgel photonic crystals in a gel matrix also avoids the melting of these crystals upon variation of stimuli, thereby making their optical properties tunable reversibly with respect to the stimuli.

Another alternative method for fabricating colloidal photonic crystals of PNIPAM microgel particles without using an external gel matrix is by directly cross linking neighboring microgel particles in the crystalline state [42]. In this method, polymerizable groups such as vinyl groups are chemically added to microgel particle surface. The microgels with polymerizable groups are made to crystallize by self-assembly process. Cross linking between neighboringmicrogel particles is achieved by photo-polymerization process [42].Based upon the application, one of the above methods is employed for fabricating portable colloidal photonic crystals of microgel particles. In applications where stimuli responsive property of the polymer gel matrix is useful, there the gel matrix is allowed to swell or deswell to external stimuli and the changes in

gel swelling/deswelling is monitored by recording the shift in Bragg diffraction of the photonic crystals immobilized in the gel matrix [36]. On the other hand, applications that require change of lattice spacing of microgel crystals with stimuli due to swelling/deswelling of microgel particles, method of fabrication involving direct cross-linking of neighboring microgel particles may prove beneficial.
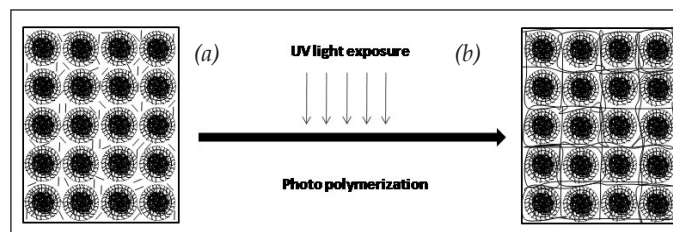

Figure 8. Schematic describing the procedure for immobilization of microgel photonic crystals in a polymer hydrogel matrix by UV-photopolymerization: (a) Microgel photonic crystals in a pre-gel solution (b) microgel photonic crystal upon gelation.

Conclusions

We have discussed the immense use of fabricating photonic crystals using self-assembly/self-organization process. The advantage offered by stimuli responsive microgel particles in fabricating colloidal photonic crystals over the hard-sphere and charged organic or inorganic particles is discussed. The variation in particle size and associated changes in refractive index contrast of thermo responsive PNIPAM particles as well as pH responsive acrylic acid functionalized PNIPAM particles help in tuning Bragg diffraction peaks or stop bands of microgel photonic crystals assembled using these particles. Response of individual PNIPAM microgel particles as well as photonic crystals of PNIPAM particles, to temperature and pressure has been presented. By observing the blue shift in Bragg diffraction of PNIPAM photonic microgel crystals subjected to different amounts of osmotic compression, it is shown that microgel particles not only shrink in size upon increasing the temperature but also to osmotic pressure.The use of dynamic light scattering technique for characterizing size and size poly dispersity is presented. Experimental techniques such as static light scattering, ultra-small angle x-ray scattering, UV-visible spectroscopy and confocal laser scanning microscopy have been discussed in brief for characterizing the structure of colloidal photonic crystals. The method for fabricating portable colloidal photonic crystals, through immobilization in a polymer gel matrix, is presented. Bragg diffraction from the functionalized PNIPAM microgel crystals using stimuli like pH, ionic strength, temperature and osmotic pressure is shown to be useful for not only for investing the swelling and

deswelling behavior of PNIPAM microgel particles under osmotic compression, but also for several high-tech applications. Though this article only dealt with colloidal photonic crystals of spherical particles through self-assembly process, there have been several interesting reports of colloidal photonic crystals fabricated using non-spherical particles and through non-self-assembly process such as e-beam lithography, holographic optical tweezers, holographic optical lithography, direct laser writing, focused ion beam milling [12,43]. Despite these techniques being cumbersome to use and expensive, nevertheless are useful for making desired photonic crystal structures with potential for realizing complete photonic band gap.

Acknowledgements

References:

1. J. D. Joannopoulos, S. G. Johnson, J. N. Winn and R. D. Meade, " *Photonic Crystals: Modeling Flow of Light*", Princeton University Press, Oxford (2008).
2. H. Wang and Ke-Qin Zhang, *Sensors*, **13**, 4192(2013).
3. T. Maka *et al.*, *Progress in Electromagnetic Research*, **41**, 307 (2003).
4. B. V. R. Tata *et al.*, *Current Science* **103**, 1175 (2012).
5. H. S. Lee *et al.*, *Chem. Mater.* **25**, 2684 (2013).
6. S. John, *Nat. Mater.* **11**, 997 (2012).
7. E. Yablonovitch, *Nat. Mater.***11**, 1000 (2012).
8. C. Paquet and E. Kumacheva, *Mater. Today***11**, 48 (2008).
9. Y. Zhao *et al.*, *Chem. Soc. Rev.* **41**, 3297 (2012).
10. J. V. Sanders, *Nature* **204**, 1151 (1964).
11. B.V.R. Tata and S.S. Jena, *Solid State Commun.***139**, 562 (2006).
12. B. V. R. Tata, *Current Science* **80**, 948 (2001).
13. R. D. Pradhan *et al*, *Phys. Rev. B***55**, 9503 (1997).
14. B. V. R. Tata *et al.*, *Int. J. Adv. Eng. Sci. Appl. Math.* **5**, 240 (2013).
15. C. D. Jones and L. Andrew Lyon, *Macromolecules* **33**, 8301 (2000).
16. Li-Yi Chen *et al.*, *Appl. Mater. Interfaces* **5**, 4383 (2013).
17. Q. Luo *et al.*, *Journal of Polymer Science: Part A: Polymer Chemistry* **48**, 4120 (2010).
18. A. Fernández-Nieves *et al.*, *J. Chem. Phys.* **119**, 10383 (2003).
19. Lietor-Santos *et al*, *Macromolecules* **42**, 6225 (2009).
20. R. G. Joshi *et al*, *AIP conf. proc.* **1349**, 208 (2010).
21. B.R. Saunders, *Langmuir* **20**, 3925 (2004).
22. J. Wu *et al.*, *Phys. Rev. Lett.* **90**, 048304 (2003).
23. P. S. Mohanty and W. Richtering, *J. Phys. Chem. B* **112**, 14692 (2008).
24. J. Brijitta *et al.*,*J. Nanosci. Nanotechnol.***9**, 5323(2009).
25. J. Gao and B. J. Frisken, *Langmuir* **19**, 5217(2003).
26. I. Varga *et al.*, *J. Phys. Chem. B* **105**, 9071 (2001).
27. J. Brijitta *et al.*, *J. Polym. Res.* **22**(36)(2015).
28. B.J. Frisken, *Applied Optics* **40**, 4087 (2001).
29. H. Zhou *et al.*, *Langmuir* **27**, 7439 (2011).
30. C. J. R. Sheppard and D. M.Shotton, *Confocal Laser Scanning Microscopy*, β IOS Scientific Publishers, Oxford, UK (1997).
31. J. Brijitta *et al.*, *J. Chem. Phys.* **131**, 074904 (2009).
32. A. V. Petukhov *et al.*, *J. Appl. Cryst* **39**, 137 (2006).
33. R.G. Joshi *et al.*, *J. Chem. Phys.* **139**, 124901 (2013).
34. T. Sawada *et al.*, *Jpn. J. Appl. Phys.* **40,** L1226 (2001).
35. R. G. Joshi, *Ph. D. Thesis* (Homi Bhabha National Institute), Unpublished (2015).
36. J. M. Weissman, *Science* **274**, 959 (1996).
37. B. Sierra-Martín *et al.*, *Phys. Rev. E* **84**, 011406 (2011).
38. T.Kanai *et al.*,*J. Ceram. Soc. Jpn*. **118**, 370 (2010).
39. M. Murai *et al.*, *Langmuir* **23**, 7510 (2007).
40. C. E. Reese *et al.*, *J. Am. Chem. Soc.* **126**, 1493 (2004).
41. W. Song *et al.*, *Soft Matter* **9,** 2629(2013).
42. M. Chen *et al.*, *Angew. Chem. Int. Ed.* **52**, 9961(2013).
43. S. Takahashi *et al. Nat. Mater.* **8**, 721 (2009).

Dr. B V R Tata *is from 25th batch BARC training school and joined in IGCAR in the year 1982. He is currently the senior professor and Dean-academic of Homi Bhabha National Institute. He has established a vibrant research programme in the area of Photonic crystals and soft condensed matter in Materials Science Group, IGCAR. He has obtained his Ph.D from University of Madras, Chennai. Earned high reputation both nationally and internationally for the original, elegant and impressive experiments in the areas of structural ordering, dynamics and phase transitions in nanoparticle dispersions and stimuli-responsive nanogels, bio-colloids etc. He has 72 journal publications and two books to his credits. His expertise lies in light scattering, confocal microscopy, rheology and computer simulations.*

Dr. R.G. Joshi *has completed his Ph. D from Homi Bhabha National Institute. He is from the 7th batch of RRCAT training school and joined as scientific officer in Condensed Matter Physics Division, IGCAR in the year 2007. Since then he is working in the area of soft condensed matter. His research interests are in the area of structural ordering, dynamics, phase transitions and rheology of soft matter and in particular stimuli responsive microgels and fabricating photonic crystals through colloidal route. He is an expert in static and dynamic light scattering and rheology.*

In this issue